Variability and climate change signals in the Southern Ocean in the CSIRO and Antarctic CRC Coupled Ocean-Atmosphere Model.

Ann-Maree Catchpole

Submitted in fulfillment of the requirements for the Degree of

Masters of Science

University of Tasmania (January, 2007)

Declaration

I hereby declare that this thesis contains no material which has been accepted for the award of a degree or diploma by any tertiary institution. To the best of my knowledge and belief, this thesis is solely the work of the author and contains no material previously published or written by another person except where due acknowledgement and reference are made in the text.

Authority of access

All authority to this thesis is given to the University of Tasmania. This authority is subject to any agreement entered into by the University concerning access to the thesis.

Abstract

To investigate the variability and potential climate change impacts in the Southern Ocean I use output from the c10, c15 and c16 model runs of the CSIRO and Antarctic CRC coupled ocean-atmosphere model. 300 years of the output is reported here, after a spin up of approximately 1000 years. Modifications over the earlier versions of this model (c10 and c15), including improved topography in waters south of Australia make the c16 model run more suitable for examining natural variability in the southern ocean. We use potential temperature, salinity and velocity (21 depths, 66 longitudes and 29 latitudes in the Southern Hemisphere Ocean) and surface heat flux (66 longitudes and 29 latitudes in the Southern Hemisphere).

Hovmoeller diagrams of potential temperature anomalies along a streamline show circumnavigating propagation. At 400 m, the strongest anomaly timescales are 4-5 years (interannual anomalies) and take approximately 20 years to travel around the globe. The anomaly strength is not uniform along this streamline and the strongest anomalies occur in the longitude band 100 to 200°E. Below 1000 m, decadal variability is the dominant signal and persists to at least 2000 m. Scatterplots show a clear relationship between ACC current speed and phase speed throughout the water column. This relationship is strongest at intermediate depths (500 to 1500 m) where anomalies are most strongly advected and least subject to other influences such as convection, mixing and mid-ocean ridges.

Using HEOF analysis revealed two dominant modes of variability in the Southern Ocean. First, a mode characterised by zonal wavenumber 3, interannual anomaly in temperature and salinity on shallow to intermediate depth and density surfaces. Interannual variability of wavenumber 2 or 3 has been described in studies using observations or models of the Southern Ocean. Also, significant correlation between temperature and pressure anomalies occurred on density surfaces. The pressure pattern is 180° out of phase with the temperature changes on density surfaces. This is similar to a mechanism proposed by (White et al., 1998) for the ACW. The second mode is characterised by zonal wavenumber 2, decadal variation at all intermediate to deep depths and density surfaces. Overall, the decadal signal is the dominant feature of the Southern Ocean, with more total energy in this mode throughout most of the water column.

Variability in several atmospheric properties including wind stress, heat and salinity fluxes is examined. The heat flux and meridional wind component showed dominant modes of interannual variability with zonal wavenumber 3. These two properties have been shown to play a significant role in determining SSTs in the Southern Ocean. The results indicates that heat flux and meridional wind are important for creating zonal wavenumber 3 interannual variability in resultant SSTs. The second mode, consists of a decadal signal with dominant zonal wavenumber 2. This suggests that slower timescales may occur in the ocean due to natural filtering of anomalies such that interannual signals are absorbed and only the longer term decadal signals remain. The change in dominance from a signal with spatial structure zonal wavenum-

ber 3 to zonal wavenumber 2 is more complex. Exploring the possible reasons for a zonal wavenumber 2 structure required investigation of convection regions in the Southern Ocean. An estimate of mixed layer depth revealed two dominant regions of wintertime convection. The first begins in the southeast Indian Sector of the Southern Ocean and continues to below Australia. The second region is the Pacific Ocean to the east of Drake Passage. These two regions are important for generation of SAMW and AAIW respectively. In essence, these two regions of convection act like highways in a myriad of surburban streets whereby anomalies at the surface can quickly access the deeper depths (compared with anomalies at the surface in adjacent regions of low convection). A simple model is used to test the assumption (Chapter 4). Forcing this model with interannual, zonal wavenumber 3 heat flux anomalies and applying a convection system of two convective regions, we obtain a resultant subsurface anomaly with zonal wavenumber 2. The hypothesis that the distribution of convection regions influences the zonal wavenumber structure of anomaly was shown to be reasonable.

For the third aim, I compared warming and deepening signals seen in the transient model run with a control run. There is a consistent pattern of cooling on isopycnals in shallow/Mode waters and warming on isopycnals in AAIW in the transient run. This coincides with a general deepening of density surfaces. The fingerprint experiment reveals statistical significance in these results indicating that the simulation of CO_2 changes indeed produces changes to Southern Hemisphere water masses with the described spatial pattern. Qualitative comparison with studies of observed changes show a

similar pattern of change.

Contents

List of Figures

List of Tables

Chapter 1

Introduction

Motivation

Between the preindustrial era and 1997, Carbon Dioxide (CO_2) levels in the atmosphere increased from approximately 280 to 360 ppm (Friedli et al., 1986; Hansen et al., 1998; Keeling and Whorf, 1998). Correspondingly, the last 150 years show an increase in global mean surface temperature of between 0.3 and 0.6°C (Jones et al., 1986; Jones and Osborn, 1997; Nicholls et al., 1996). These statistics lead us to investigate whether man's influence is in fact leading to a global climate change or whether we are undergoing natural climatic variations? If there are long term climate changes occurring, what will ensue for our living conditions?

Current state and prediction

The International Panel on Climate Change (IPCC) is working toward answering these and more questions. In the 2001 Summary for Policymakes,

some predictions include: temperature forecast to increase by 1.4 to 5.8°C over the period 1990 and 2100. Sea-level is predicted to rise between 0.09 and 0.88 m in the same period. Also, the report indicates that further research using both observations and models is required to reduce uncertainties in the process of detection, attribution and projection of climate change. In particular, there is a need for additional systematic observations, modeling and process studies. This study aims to increase knowledge by investigating natural variability in the Southern Ocean as simulated by a coupled ocean-atmosphere Model. Further, to explore the signature of climate change in the Southern Ocean water masses.

Understanding the oceans role in the climate cycle

If the first aim in climate science is to gain an accurate picture of our current state of climate, the second is to understand the mechanisms behind it. The earth's climate is controlled by many small and large scale processes which are both simple and complex. Voids of knowledge within many branches of science have been identified in the 'quest' to detect climate change. Central to investigations, a key regulator of the climate system is the Global Ocean. The most important ocean climate regulator is its large scale circulation, known as thermohaline circulation or the global conveyor. Thermohaline circulation is crucial for the redistribution of heat from the atmosphere to the deep oceans. Models which simulate world climate and have made disturbing predictions of a breakdown or reversal of this most critical circulation. Ice and sediment records have shown that the thermohaline circulation has

previously undergone slowdowns or reversals in response to previous changing climates (Broecker, 1997). Through thermohaline circulation and other processes, the ocean is able to achieve a virtually constant uptake of heat in warm regions and release of heat in cool regions. Alongside the uptake and release of heat is the uptake and release of chemicals and molecules such as Carbon Dioxide (CO_2) and Oxygen (O_2). Storage and transport of these components is essential for flourishing ocean productivity. In some cases it is also critical for maintaining atmospheric concentrations below levels which may alter the terrestrial environment. Therefore, it is fundamental that we understand the mechanisms behind and the current state of the ocean as a climate regulator. Furthermore, the ocean is as important as the atmosphere for climate monitoring as the ocean acts to filter short term fluctuations and thus long term signals are more clear in ocean observations compared with the atmospheric equivalent.

Where are we?

Much of our understanding of the ocean has been made in the last few decades with the aid of new technology[1]. Despite exponential growth in our oceanic knowledge base, extensive research is required for determining the current state of the ocean and for setting up suitable climate monitoring programs. At the 1995 International Panel on Climate Change (IPCC), a number of target areas were set highlighted. One of these is 'Natural Variability' on decadal to century timescales. The reason for this target area is as fol-

[1]Technology for monitoring the ocean includes ctd, xbt, satellite etc

lows: Recorded gradual changes in observations need to be considered in terms of the natural variations occurring. A key problem in the detection of an anthropogenic signal in today's climate is estimating the levels of variability one might expect to occur naturally (Barnett, 1999). This problem exists because there is a general lack of complete observations in space and time for the ocean and the atmosphere. In particular, with relatively short timescales of observational data, very little is known about ocean variability on decadal timescales from observations - these timescales being those upon which climate change is to be monitored. In order to better understand natural variability, science has thus far begun a strong campaign which draws upon the use of climate models to determine levels of variability and climate change scenarios. Early studies which use models for detection of climate change include Santer et al. (1996).

Working Toward a Global Climate Monitoring System.

Efforts[2] which have focussed on the above goal have lead to considerable progress in our understanding of our climate systems. Great advances in computer technology have enabled simulations of global climate using Global Climate Models (GCMs). GCMs provide extensive time and spatial information with various climate scenarios and in many cases are the only tool for which to conduct low frequency studies. GCMs employ assumptions and parameterizations of many processes. This is essential in order to generate re-

[2]For example the Coupled Model Intercomparison Project (CMIP) aims to constantly compare the output from various models in order to monitor the status of model accuracy

sults in reasonable timeframes but requires us to understand their predictive limits. Coupled ocean-atmosphere models will generally see more variability in both sea-surface ocean and atmosphere properties than in an atmosphere model with fixed ocean data-sets (Barsugli and Battisti, 1998). The Coupled Model Intercomparison Project (CMIP) identifies key areas for model improvement. The project revealed that early model variability studies produced mixed results (Barnett (1999)). On inspection, approximately 50% of the disparity arose from the model drift. Improvements in this area have been substantial. The CSIRO c17 model run (used in this study) made considerable advances in reducing drift (Bi, 2002). Also, flux adjustments are now so small as to be negligible. With such advances in place, the variation in energy between models is still seen to be greater than a factor of 2 between various models. Such results suggest that coupled general circulation models can not yet be used for accurate prediction and a discussion of model assumptions and parameterizations is useful in any interpretation of model output.

In the remainder of chapter 1, I will introduce the oceanographic concepts which are a basis for this research. The concepts discussed include the Southern Ocean and its fronts and water masses. Then I discuss observed changes of water masses and simulations by models. Further I discuss a Southern Ocean variability mode, the 'Antarctic Circumpolar Wave' and its significance in the Southern Ocean Dynamics. Then I discuss detection and fingerprint experiments which examine climate change in the Southern Ocean. At the end of the chapter I present the aims of my thesis in and discuss chapter

outlines.

1.1 The Southern Ocean water masses

This study uses output from a coupled ocean-atmosphere-sea ice model to study the Southern Ocean. This section of the global ocean has been explored relatively little and its significance in a global climate context has not been established. It is unique from other oceans in that its dominant current, the Antarctic Circumpolar Current (ACC), flows virtually uninterupted by continents. The ACC is primarily driven by prevailing westerly winds and its speed and transport is believed to be a balance between surface zonal windstress and the bottom and lateral frictional retardation (Bi, 2002).

Much of the progress in understanding the ACC and Southern Ocean has been in remaining decades of the 20th Century through programs such as International Southern Ocean Studies (ISOS) and the World Ocean Circulation Experiment (WOCE).

Subantarctic Mode Water (SAMW) formation and Antarctic Intermediate Water (AAIW)

In the Southern Hemisphere, regions of thick mixed layer are typically regions of SAMW (McCartney, 1977). SAMW is formed by deep winter convection on the north side of the Sub Antarctic Front (SAF). SAMW is identified by the following characteristics: an oxygen rich vertical mixed layer (Rintoul et al., 2001); Temperatures in the range of 4 to 15 °C; Salinity in the

range 34.2 to 35.8 psu and Potential Density ($\sigma(\theta)$) in the range 26.5 to 27.1 kg/m^3 (McCartney, 1977). SAMW presence extends well beyond its formation region. McCartney (1982) discusses the flow of SAMW from formation regions to the lower thermocline of southern hemisphere subtropical gyres (McCartney, 1982). Observations show that the easternmost SAMW in the Indian Ocean is the densest outcropping water in the combined South Atlantic and South Indian Ocean subtropical gyres (McCartney, 1977). Rintoul (1991) and Sloyan and Rintoul (2002) showed that SAMW (and AAIW) form the upper limb of the global overturning circulation . In the ACC SAMW becomes progressively cooler, fresher and denser across the Indian and Pacific Ocean Basins (McCartney, 1982). The change in temperature is due to the mainly southward movement of the SAF (winter convection occurs just north of the SAF). In the western Atlantic, the SAF is at its most north and SAMW is its warmest.

AAIW is identified by a salinity minimum that descends near the Subantarctic Front (Hanawa and Talley, 2001). Before McCartney (1977), authors believed that the circumpolar AAIW tongue was renewed by northward sinking of cold, fresh Antarctic Surface waters (Rintoul et al., 2001). (McCartney, 1982) first suggested the easternmost SAMW in the South Pacific (the densest water outcropping in the South Pacific subtropical gyre) is the source of AAIW. Mixed layer depths occur off the coast of Chile to approximately 600 m. AAIW moves north on the eastern side of the Pacific and joins the subtropical gyre. It also moves through the Drake Passage into the Atlantic where it undergoes subduction. The advected AAIW receives modifications

in the Indian and Atlantic regions giving it unique properties in each region. Work by England et al. (1993) reveals AAIW within a GCM originating in the South-East Pacific and spreading around the globe.

1.2 Observed changes and water mass variability

Many studies have been conducted which compare water mass properties over time in order to establish whether water masses are staying constant or experiencing change. The following discusses results from various studies on water mass properties and surface forcing mechanisms which impact on watermass formation.

Aoki et al. (2005) examine water-mass changes along meridional lines in the Indian and south-west Pacific sectors of the Southern Ocean. Along 45°E, 110°E and 150°E they find significant freshening and cooling on neutral density surfaces at around 27.0 kgm^{-3} equatorward of the Sub-Antarctic Front. These changes are consistent with other observations showing cooling and freshening of SAMW. Deeper (around 27.9 kgm^{-3}) and south of the Polar Front they find warm and saline anomalies on neutral density surfaces of around 27.9 kgm^{-3} with oxygen decreases. They explain this is most simply due to the ventilation by warm, fresh surfaces waters. A study by Banks and Bindoff (2003) using the coupled ocean atmosphere model HadCM3 reveal a similar pattern of cooling and freshening on isopycnals at midlatitudes and

warming on isopycnals at high latitudes. They suggest the results are linked to changes in surface fluxes and that surface warming is the dominant factor influencing the surface flux.

Bindoff and Church (1992) show warming in the southwest Pacific in a section between Australia and New Zealand using SCORPIO sections. The rates of warming are a depth average of 0.04 and 0.03°C at 43°S and 28°S respectively over a period of 22 years. The highest warming is seen at 500-750 dbar with warming at all depths but with decreasing magnitude. This is with the exception of a slight cooling at 43°S at around 1500 dbar. In a later study (Bindoff and McDougall, 1994) show that these decadal changes are due to warming and freshening of source waters. In contrast, two sections taken 6 months apart show changes which are only attributable to the vertical displacement of the neutral density surfaces.

Bindoff and McDougall (2000) examine observations along the 32°S Indian hydrographic section from 1962 and 1987. Their results show that AAIW and SAMW have deepened, freshened and cooled. They discuss the changes and most likely causes. Changes in SAMW are most likely to be due to a warming of the surface waters at the source region. Changes in AAIW can be explained by an increase in precipitation in the AAIW source region. More recent research by (Bryden et al., 2003), show that the 32°S Indian hydrographic section (a remote Indian Ocean section) revealed saltier and cooler mode waters since 1987. This compares with freshening and warming of the mode waters that occurred between 1965 and 1987 and little change between 1936

and 1965. Hence this result is in contrast with other studies which evidence warming and freshening of sections within the Indian and Pacific Ocean. The study concludes that mode water properties exhibit significant variability.

Rintoul and England (2002) examine changes in temperature and salinity in SAMW in observations south of Australia (along SR3 at around 145°E) to find significant variability. Their investigations show that the changes are explained by variations in northward ekman transport of cool, low salinity water across the subantarctic front. They use results from a coupled ocean atmosphere model to show the observations are typical of the subantarctic zone.

Hence previous studies which use observations and/or models have found significant freshening and cooling on neutral density surfaces in SAMW (26.5 to 27.1 kgm^{-3}) and warming and increasing salinity on deeper neutral density surfaces at higher latitude (usually associated with Circumpolar Deep Water). The changes have generally been suggested to be due to changes in heat and freshwater flux at the source regions (for water mass). However Rintoul and England (2002) give evidence to show that these air-sea flux variations were too small to explain the variations. They showed that changes in SAMW can be explained by variations in ekman transport of cool fresh water across the SAF leading to changed source water properties. Therefore, the study by (Rintoul and England, 2002) indicates that meridional wind stress is the dominant factor in determining water mass changes. This contrasts with the general suggestion of dependence on atmosphere and ocean heat

and mass exchange.

Using a GCM, Toggweiler and Samuels (1993), Toggweiler and Samuels (1995) and McDermott (1996) vary the magnitude of wind stress over the Southern Ocean. They find that the magnitude of the ACC increased as winds were increased as did pycnocline depth north of the ACC and the magnitude of the Northern Hemisphere Circulation.

Changes in forcing mechanisms

For the Indian Ocean, Allan and Reason (1995) describe observations which reveal changes in ocean-atmosphere forcing during this century. These include warmer SSTs and strengthening of an anti-cyclone in the mean flow field over the Indian Ocean in January to March during early 1900's to 1970's from Comprehensive Ocean-Atmosphere Data Set (COADS) and United Kingdom Meteorological Office (UKMO) Global Sea-Ice and Sea-Surface Temperature (GISST) data. Forcing a model with selected winds, these changes were shown to be related to the Indonesian throughflow passage and in turn affected the Agulhas Current Reflection Zone (inclusive of the region at 40° between Southern Africa and the SW Australian Sectors in the Southern Ocean). In particular, CO_2 forcing resulted in less warm water reaching the Indian Ocean via the Indonesian throughflow and a weaker Agulhas Current.

Antarctic Circumpolar Current

Observations within the ACC in the Southern Ocean have revealed a mode in sea surface properties which varies on timescales similar to the Southern Oscillation Index (SOI). The phenomena is described by White and Peterson (1996). In their study, they examine sea-level pressure (SLP), meridional windstress (MWS) from forecasts for years 1985-1994, sea surface temperature (SST) from years 1982-1994, sea-ice extent (SIE) from 1979-1991. SLP, SST and MWS were averaged over 55-65°S. The data were filtered using a 3-7 year bandpass filter. In their analysis, they observe anomalies occurring on time scales of 4-5 years which appear to circumnavigate the whole Southern Ocean. This takes approximately 8-10 years and shows a zonal wavenumber pattern 2. White and Peterson use the phrase 'Antarctic Circumpolar Wave' (ACW) to describe this mode of propagating anomalies. Observed anomalies were strongest in the Pacific sector of the southern ocean. Their comparison of variables showed that warm (cool) SST trail low (high) SLP by 1 year (90° out of phase in a 4 year cycle). They suggest a possible atmosphere-ocean teleconnection between El-Nino Southern Oscillation (ENSO) and the ACW.

Since this study there has been extensive discussion on the ACW. Observations and model output have both been used to identify propagating anomalies which are similar to the ACW. Using anomalies along 56°S from a coupled ocean-atmosphere-sea ice model, Motoi et al. (1998) obtain SST and SSS anomalies of 1.2°C and 0.4psu respectively. The SST anomaly agrees with results of White and Peterson (1996) and SSS agree with Murphy et al.

(1995). Motoi obtain a period of 20-30 years, noting it is considerably slower than the observed 8-10 years (White and Peterson, 1996). They suggest the slower propagation is due to a slow model ACC mean speed of 0.02m/s. A significant relationship between sea-ice and ENSO is discussed by Gloersen (1995) and Murphy et al. (1995).

Numerous modelling studies (including Christoph et al. (1998) and Cai et al. (1999)) reveal an ACW which has a slower propagation and has zonal wavenumber 3. Motoi et al. (1998) suggests slower propagation seen in models is due to slower Antarctic Circumpolar Current speeds. This needs to be taken into account if model results are to be used for comparison of observations or predictive purposes. Baines and Cai (2000) use a CGCM to find a similar result and suggest that the zonal wavenumber 3 pattern arises in a model dataset where they provide longer and more comprehensive datasets. Since the observational records are short, longer model runs are being used to determine whether the mode is stable over the long term (or just a unique occurrence). General attempts to determine the mechanism behind ACW-like propagating anomalies are hindered since basic characteristics of the mode (eg. frequency and zonal spatial structure) are often not consistent between datasets. The initial study by White and Peterson (1996) showed that oceanic properties (SST) were out of phase with atmospheric properties (SLP) suggesting atmosphere-ocean connection. An analysis of observations by Bonekamp et al. (1999) includes the original dataset used by White and Peterson (1996) and a further 5 years of observations. The extended data set showed SLP anomalies as a dominantly standing wave compared to a

propagating wave in the shorter data set. Hence it is not clear whether the observed mode involves propagating SLP anomalies at all. Other studies support the original ocean-atmosphere interaction hypothesis by suggesting the mode arises due from the thermodynamic balance between SST and meridional wind stress (MWS). Other studies have shown that, to an extent, the ocean alone can generate ACW-like anomalies internally.

Associated questions are: is the ACW a recent phenomenom or is it continuous in time. When its existence has been established, further study will be required to determine the source and decay of the anomalies. That is, whether the anomalies are atmospheric or ocean derived and whether (and how) the anomalies influence oceanic waters outside of source regions. This area of research has some preliminary findings. Studies attempting to predict Southern Australia and New Zealand's rainfalls by means of an ACW indicator (White and Cherry (1999) and White (2000)) show significant correlation does exist between southern landmasses and ACW mode. More research is needed to determine key indicators of the ACW mode and how it will specifically impact on local climates. An area that strongly needs to be addressed is how the supposed ACW relates to watermass formation and variability. This study addresses this issue, along with determining the basic characteristics of ACW-like variability.

1.3 Thesis outline and aims

The aim of this study is to characterise the natural variability of ocean water masses on depth and density surfaces as well as correlating between patterns in the ocean and atmosphere. The timescales which are of focus are interannual to multi-decadal timescales. The justification for targeting these timescales is that they are presently the limits in which the observational record exists (and for data sparse regions: aims to exist). Hence understanding Southern Ocean variability on these timescales forms the basis for climate change monitoring.

In particular the goals for this project are as follows. (1) Examining water mass formation, water mass properties and variability within the Southern Ocean in a stable climate scenario. (2) Identify and examine key processes and regions which facilitate water mass formation or have some interaction upon water masses (within a stable climate scenario) or which may be useful in monitoring global or regional climate. (3) Examine temporal and spatial variability within the ocean and isolate sources of variability (4) Examine water mass properties in a climate change scenario and compare this with the control climate scenario and observations. (5) Identify key factors which lead to variations between control and climate change scenarios in watermass characteristics. (6) Implications from the study for global climate monitoring.

Given these goals, the broad aim is expanded into 3 thesis aims as follows: First, to characterise the general patterns of variability in the Southern Ocean component of a coupled model. Second, to determine sources or factors which

generate and influence these variability patterns. Lastly, to determine the impact of a climate change signal in terms of water mass properties.

The aim of chapter 2 is to describe the model, methods, mean fields of surface heat flux, winds, SST and identify water mass formation.

Chapter 3 examines propagation in the Southern Ocean in comparison to the observed Antarctic Circumpolar Wave. The propagation is investigated as a function of depth.

Chapter 4 characterises variability on depth layers and neutral surfaces within the ocean by examining RMS energy in various frequencies. Lastly, I examine both spatial and temporal variability of properties at the sea surface and at depth. These results combine and further the understanding given by the sections on RMS energy and propagation.

Chapter 5 involves comparing ocean variability and surface forcing such as winds and heat flux. A simple model is used to show how filtering occurs.

Chapter 6 will compare the climate change scenario run with the control model run to determine whether the climate change scenario produces any significant changes in the water masses discussed in the above chapters. Chapter 7 summarises the results and discusses the implications for further research.

Chapter 2

Dataset description and Mean fields

2.1 Model Description

In this study I use output from the c17 and t17 model runs of the CSIRO and Antarctic CRC coupled ocean-atmosphere model (Gordon and O'Farrel, 1997). These model runs were provided for use by Dave Bi, who conducted the experiments as part of his phD thesis (Bi, 2002). I use 300 years of data from each of these model runs from the year 1880 to 2180. These model runs are modified versions of the well described c10 run by Gordon and O'Farrel (1998). The c10 model run has been used in the Coupled Model Intercomparison Project (CMIP) to compare with other coupled global circulation models (CGCMs) (Meehl et al., 1997). The atmosphere component uses a spectral grid and the ocean model is a version of the Geophysical Fluid Dynamics

Laboratory (GFDL) grid point ocean model with Gent and McWilliams parameterization (Gent and McWilliams, 1990). Initial spin up uses Levitus (1982) climatology and Hellerman and Rosenstein (1983) windstress.

Many coupled models have been subject to substantial drift in the barotropic flow in the ACC (Cai and Gordon, 1999). As a result of improvements to coupled models (including intensification of deep ocean northward flow), the model runs used in this thesis shows very little drift in the barotropic flow of the ACC (Bi, 2002). Hence the model is ideal for studying water mass transports and change within the ACC and Southern Ocean.

The data set used in this analysis includes 300 years from a control run (c17) with no anthropogenic forcing. A corresponding transient model run has been included. The transient model run has been subject to anthropogenic forcing equivalent to three times the preindustrial level of CO_2 starting from the year 1880.

In this thesis I originally used model output from the original c10 (and t10) model runs before the later versions were available (including an intermediate version called c15 and t15). The c10 has been more thoroughly analysed than the c17, however modifications which include improved topography in waters south of Australia (pers comm Hirst, 1999) make the c17 run more desirable for use in analysis of the southern ocean. Hence the c17 and t17 versions were ultimately chosen as the most appropriate data sets. From these data sets I analyse 3-dimensional fields: potential temperature (hereafter temperature), salinity and velocity (21 depths, 66 longitudes and 29 latitudes in the

southern hemisphere ocean); and 2-dimensional fields: surface wind stress, surface heat and salinity flux (66 longitudes and 29 latitudes in the southern hemisphere).

2.2 Methods of Analysis

A number of methods were employed for this analysis. For oceanographic variables, as well as examining properties at constant depth (or pressure) we calculated and examined properties on neutral density surfaces (or isopycnals). Neutral surfaces are defined by satisfying the following equations:

$$\alpha \nabla_n \theta = \beta \nabla_n S \tag{2.1}$$

$$\alpha = \frac{1}{\rho} \frac{\partial \rho}{\partial \theta} |_{S,\rho} \tag{2.2}$$

$$\beta = \frac{1}{\rho} \frac{\partial \rho}{\partial S} |_{\theta,\rho} \tag{2.3}$$

There are advantages to looking at properties on these surfaces as well as on constant depth surfaces. Theoretically, the path of minimum potential energy loss occurs along neutral density surfaces (McDougall, 1987) and hence mixing tends to occur along them. Properties on neutral surfaces are calculated using an algorithm by Jackett and McDougall (1997). We calculate properties on approximately 21 surfaces of neutral density in order to represent shallow to intermediate (0-1000m) waters.

For distribution of variance within various frequencies we apply a box window to a Fourier Spectrum and then calculate the recreated signal. Signals from

up to 300 years of annually averaged oceanographic variables are filtered into 4 frequency bands: Annual-Biannual (1-3 years), Interannual (3-8 years), Decadal (8-15 years) and multidecadal (15-32 years). Hovmoeller diagrams are used to identify propagation along specific paths within the Southern Ocean.

Using model output for the southern hemisphere, at various surfaces (depth and neutral density) we calculated Empirical Orthogonal Functions (EOFs) and Hilbert Empirical Orthogonal Functions (HEOFs). Hilbert EOFs can also be referred to as Complex EOFs, a term which also includes other complex EOF methods. In order to avoid confusion we will continue to use the more specific term HEOF. Methods for calculating EOFs and HEOFs are according to Von Storch and Zwiers (1999). Various subsets of the data from the Southern Ocean were analysed, including subsets of data along lines of constant streamline, constant latitude and maximum velocity.

By definition, a HEOF analysis determines individual modes which contain both time and spatial propogation and an EOF analysis produces modes which propagate in time but are spatially stationary. Spatial Propagation can be identified using the EOF method by combining modes with similar frequency. In comparison, the HEOF compacts propagation into individual modes so it is more efficient (in terms of reducing the number of statistical modes describing the information in the data) where both spatial and temporal propagation are occurring . Reconstruction of anomalies from individual modes displays this clearly. In this study, I am concerned with variability

which is spatially propagating. I have chosen to discuss results using the HEOF method.

Hovmoeller diagrams of potential temperature anomalies along a streamline in the Southern Ocean are used to identify propagating interannual anomalies within the ACC. Anomaly wave speeds are correlated with corresponding average ACC speed to determine means of propagation.

Neutral Density Surfaces

The mean depth of a neutral surface shows that neutral surfaces typically outcrop in the Southern Ocean. The neutral density surfaces (density up to around $\gamma = 27.7\text{kg.m}^{-3}$) deepen when occurring within the subtropical gyres of the South Indian and South East Pacific Ocean. On constant pressure surfaces, this deepening of density surfaces within the subtropical gyre translates to a less dense surface existing on the constant pressure surfaces. In theory, flow along a neutral density surface gives rise to a zero loss in potential energy, so we expect that anomalies from the surface to be seen to flow from the surface into the ocean along these surfaces. Therefore, we assume that anomalies on a vertically steep neutral density surface are more easily able to access a certain depth (which the surface cuts through) as compared to a more vertically graduated neutral density surface. In this assumption, we expect there to be higher variability within the subtropical gyres due to anomalies being able to reach depth by flowing along the steep neutral density surfaces.

2.3 Mean fields and water mass identification.

The following description of the model includes an examination of the mean state of properties at sea surface as well as a discussion of ocean and atmosphere exchange.

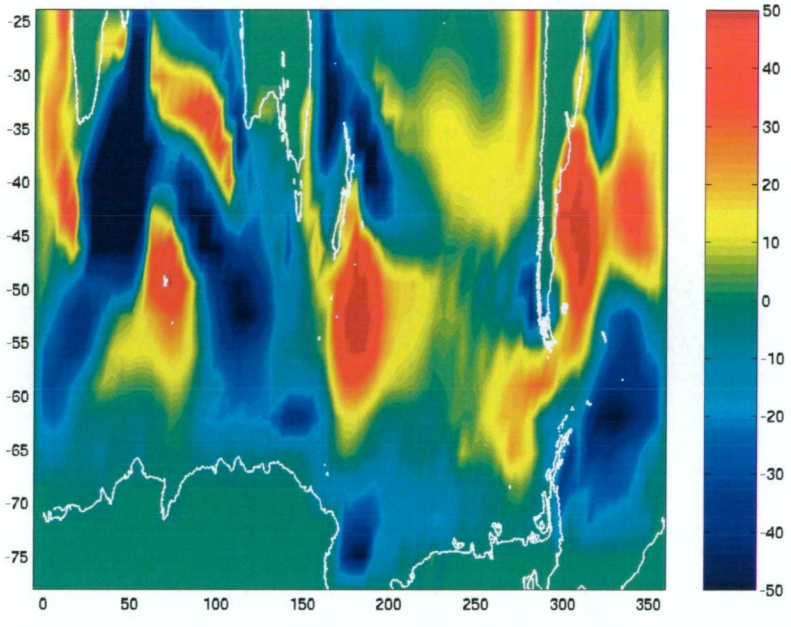

Figure 2.1: 300 year mean model heat flux (W.m^{-2}) at sea surface. Negative (blue) values indicate heat passing from the ocean into the atmosphere. Horizontal axis is Longitude (°E) and vertical axis is Latitude (°S).

Heat and Salinity flux

Heat flux is affected strongly by seasonal changes. Generally, heat is stored in the ocean in summer and released in winter. A 300 year mean heat flux is shown in Figure 2.1. The blue contours represent a transfer of heat out

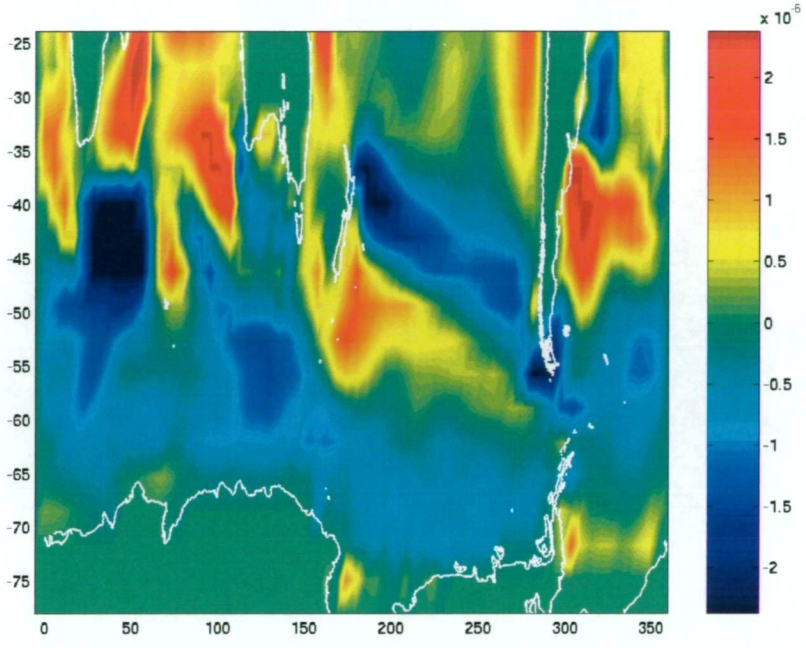

Figure 2.2: 300 year mean model salinity flux (evaporation - precipitation) (kg.psu.cm^{-2}s^{-1}) at sea surface. Positive values indicate that Evaporation exceeds Precipitation. Horizontal axis is Longitude (°E) and vertical axis is Latitude (°S).

of the ocean and red represents a transfer of heat into the ocean. Heat flux is affected by incoming solar and outgoing back radiation, evaporation and mechanical ocean-atmosphere heat transfer (Tomczak and Godfrey, 1994). The model has used heat flux corrections used to balance conservation equations. The heat flux model data presented in this thesis is post heat flux correction. Along the western boundary of each ocean there is a fast flowing current which is part of the subtropical gyre and flows south (eg. Augulus, East Australian Current). Here, warm tropical surface water is advected to colder regions and so heat is released into the atmosphere along its path (blue regions). Net heat release can also occur along the ACC in regions where its

path is in a southerly direction. This occurs in the Indian Sector between 100°E 40°S and 125°E 60°S. Regions of net ocean heat intake (red regions) include regions where surface water undergoes rapid advection to warmer (usually northerly) regions or where upwelling of cool water occurs. In the Southern Ocean this occurs in the Indian Sector (60-80°E) , in the Pacific Ocean (170-200°E) and at Drake Passage and along the east coast of South America.

In the ACC, the mean salinity flux (Figure 2.2) shows mostly regions of net precipitation (blue regions). A region of net evaporation occurs southeast of Australia and New Zealand to about 55°S.

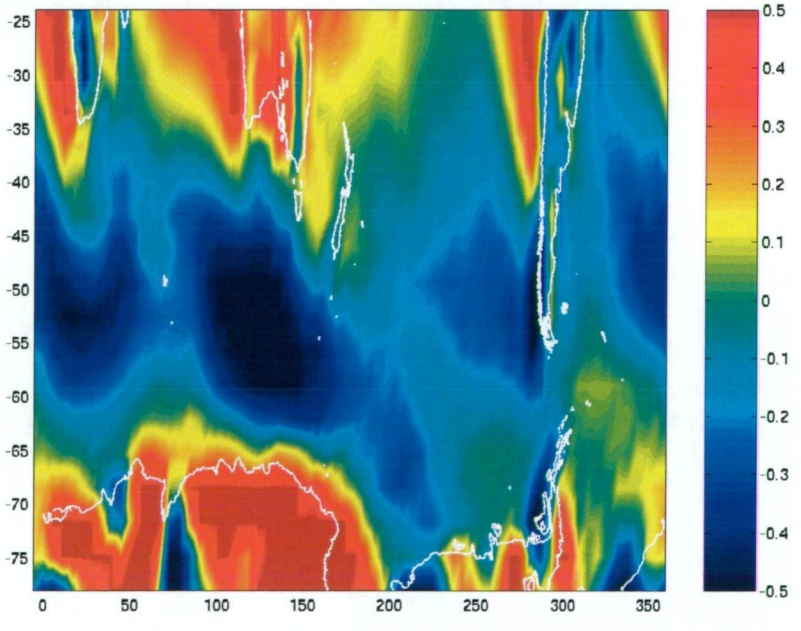

Figure 2.3: 300 year mean model meridional wind stress (dynes.cm^{-2}).Horizontal axis is Longitude (°E) and vertical axis is Latitude (°S). Blue indicates southward winds.

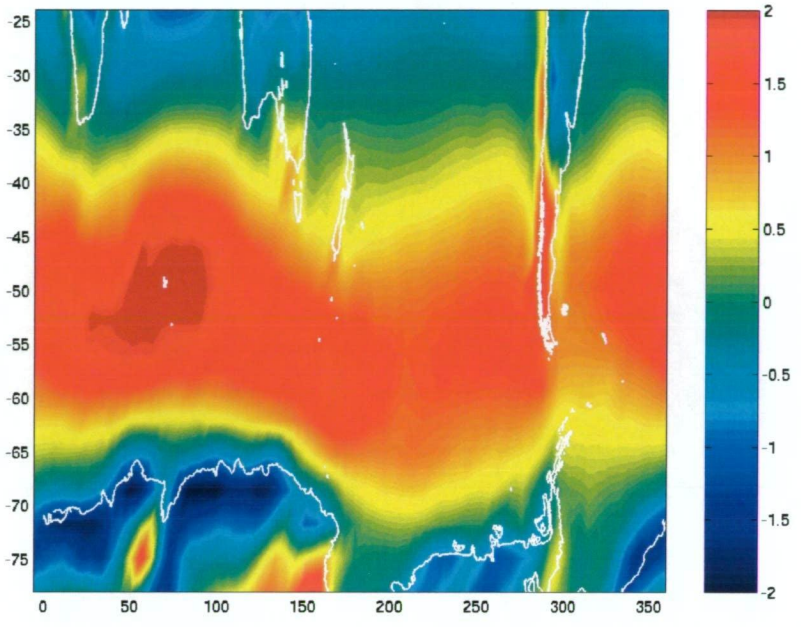

Figure 2.4: 300 year mean model zonal wind stress (dynes.cm^{-2}).Horizontal axis is Longitude (°E) and vertical axis is Latitude (°S). Red indicates eastward winds.

Winds and Surface Currents

Mean Wind Patterns are generally determined by the mean atmospheric pressure gradients. In the Southern Ocean the typical pattern from the equator to about 30°S is a system of south easterlies. At midlatitudes there exists a system of anti-cyclones (clockwise rotation) characterised by north-westerly winds. Figures 2.3 to 2.5 show the mean meridional, zonal components of wind stress and the vector plot of wind stress. These diagrams show that the model Southern Ocean experiences the typical strong westerly winds (from the west) seen between 40 and 60°S, with a northerly component (from the north). The surface ocean currents resemble Ekman currents, closely related to the winds.

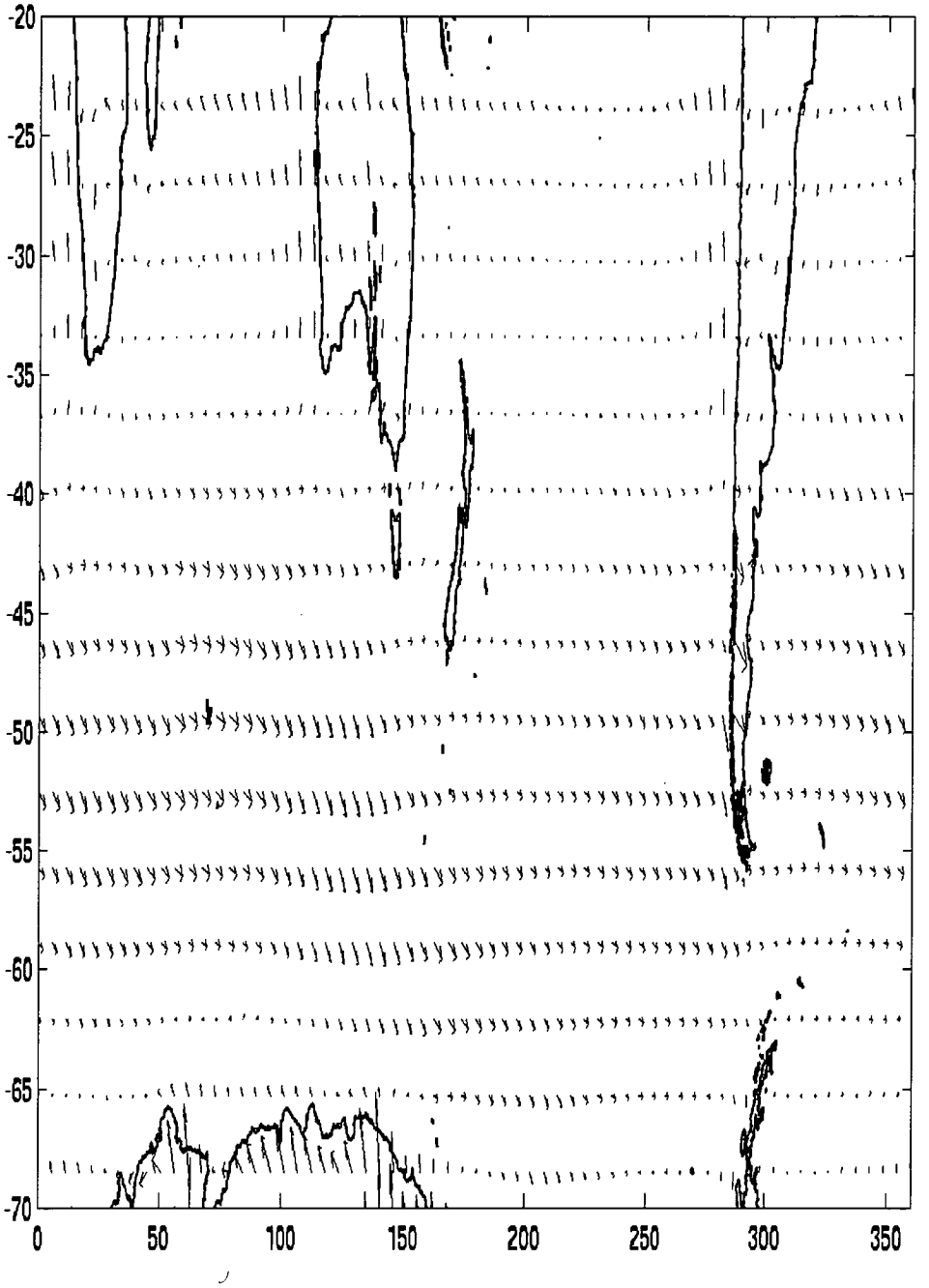

Figure 2.5: 300 year mean model wind stress vector (dynes.cm^{-2}). Horizontal axis is Longitude (°E) and vertical axis is Latitude (°S).

Water mass identification

To identify the mean position and strength of water masses I use meridional and zonal sections of oceanographic properties. As discussed in Chapter 1, Antarctic Intermediate Water (AAIW) is typically identified by a presence of a salinity minimum (34.3 - 34.6 psu) at around 1000 m in the Southern Ocean (Hanawa and Talley, 2001). Sub Antarctic Mode Water (SAMW) source regions are identified by a thick wintertime mixed layer depth (McCartney, 1977). The summer and wintertime properties are indicated by showing properties in January and July respectively (Figures 2.6 to 2.9). We first examine properties along 78°E (the South-East Indian Ocean). In July (Figure 2.6), a thick layer of constant density (a pycnostad) exists between 35 and 50°S at depths to 500 m. This pycnostad is indicated by the near vertical contours of density, temperature and (to a lessor extent) salinity to about 500 m. The layers of homogeneous density indicates an area where formation of SAMW could occur. In January (Figure 2.7), the mixed layer is shallow and SAMW formation does not occur. That is, SAMW water exists as a subsurface layer of unstratisfied water capped by the warm (low density) summertime mixed layer. The SAMW occurs with density, temperature and salinity ranges of 26.0 to 27.2 $kg.m^{-3}$, 4 to 16°C and 34.1 to 35.1 psu, respectively.

Just south there is cool fresh surface water which extends northwards and underlies the SAMW. AAIW is identified by the salinity minimum at about 1000m. The ranges for density, temperature and salinity exhibited by AAIW

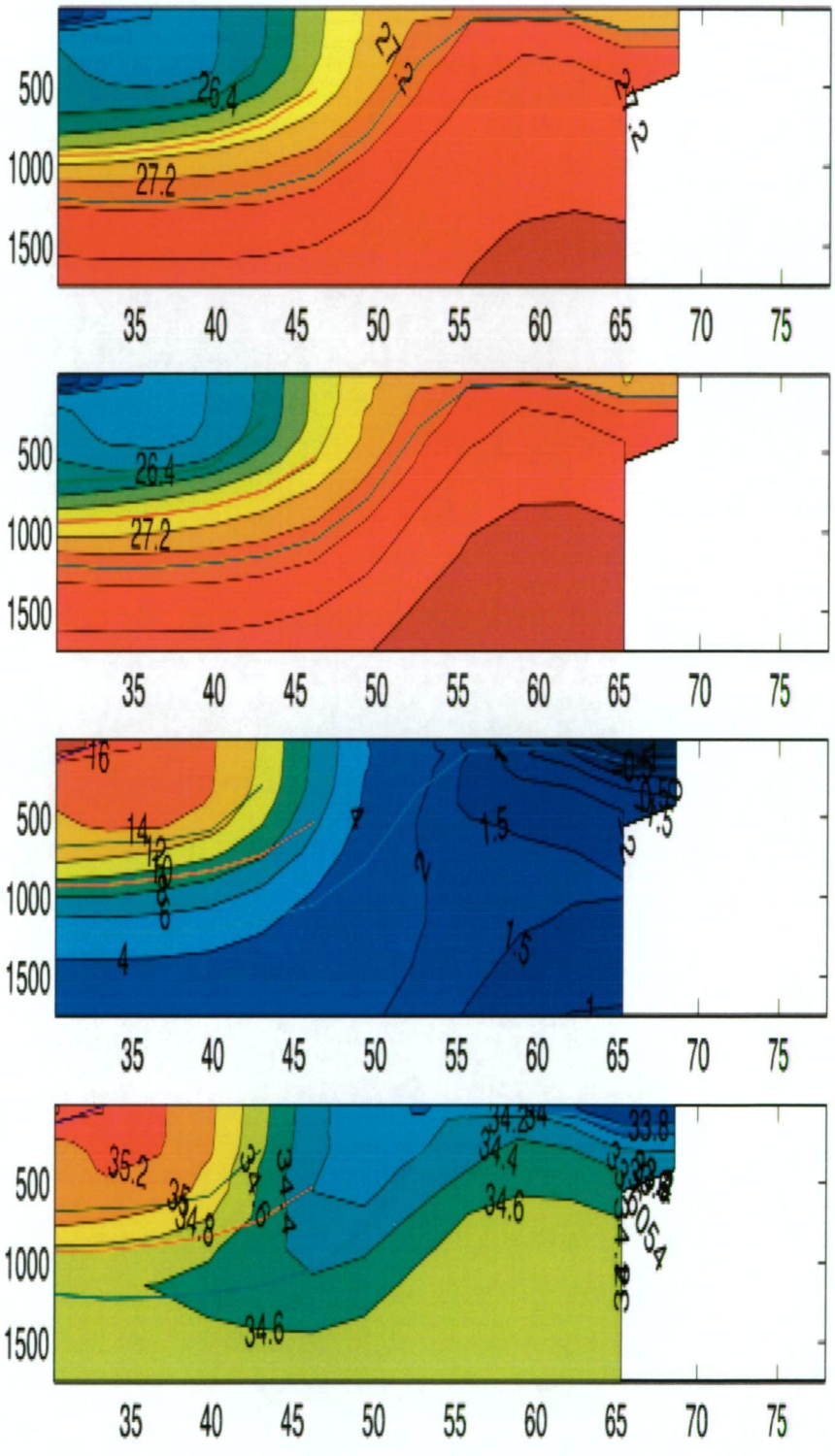

Figure 2.6: Wintertime properties along 78°E (for depths to 1500 m) in July 1880. Upper panel is density (kg.m^{-3}). Second panel is neutral density (kg.m^{-3}). Third panel is potential temperature (°C) and the lower panel is salinity (psu). Horizontal axis is Longitude (°E) and vertical axis is Depth (m).

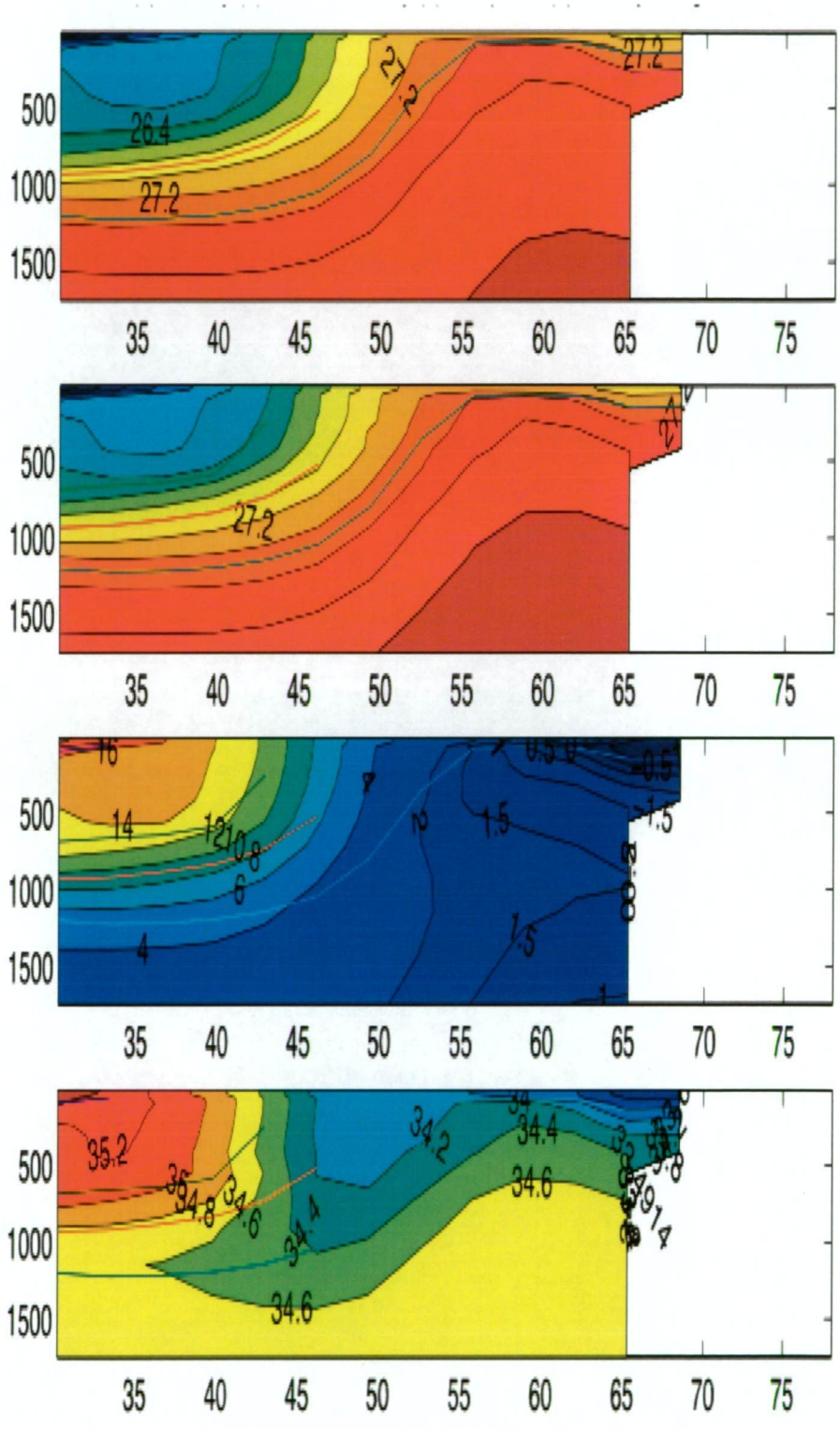

Figure 2.7: Summertime properties along 78°E (for depths to 1500 m) in January 1880. Upper panel is density (kg.m^{-3}). Second panel is neutral density (kg.m^{-3}). Third panel is potential temperature (°C) and the lower panel is salinity (psu). Horizontal axis is Longitude (°E) and vertical axis is Depth (m).

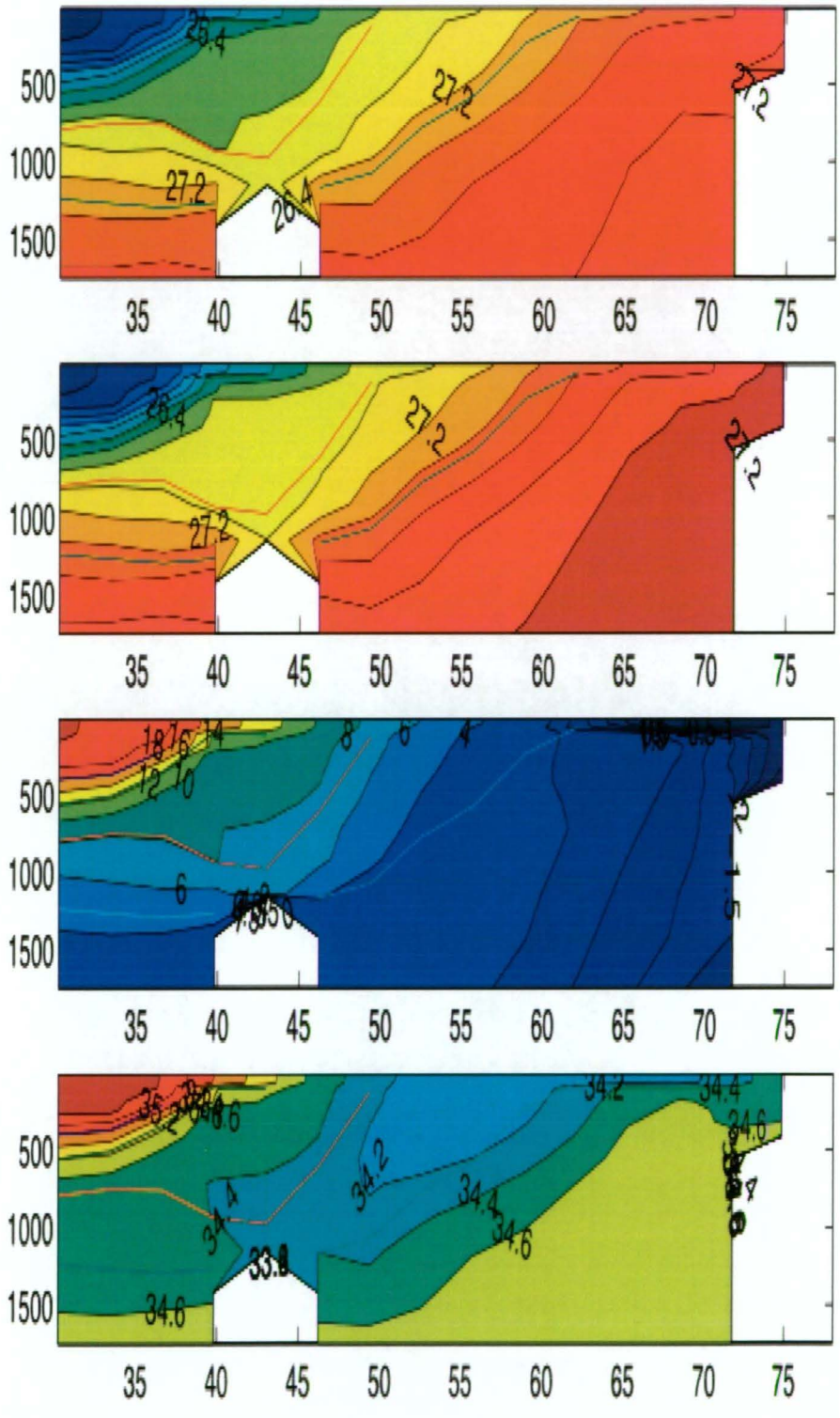

Figure 2.8: Wintertime properties along 180°E (for depths to 1500 m) in July 1880. Upper panel is density (kg.m^{-3}). Second panel is neutral density (kg.m^{-3}). Third panel is potential temperature (°C) and the lower panel is salinity (psu). Horizontal axis is Longitude (°E) and vertical axis is Depth (m).

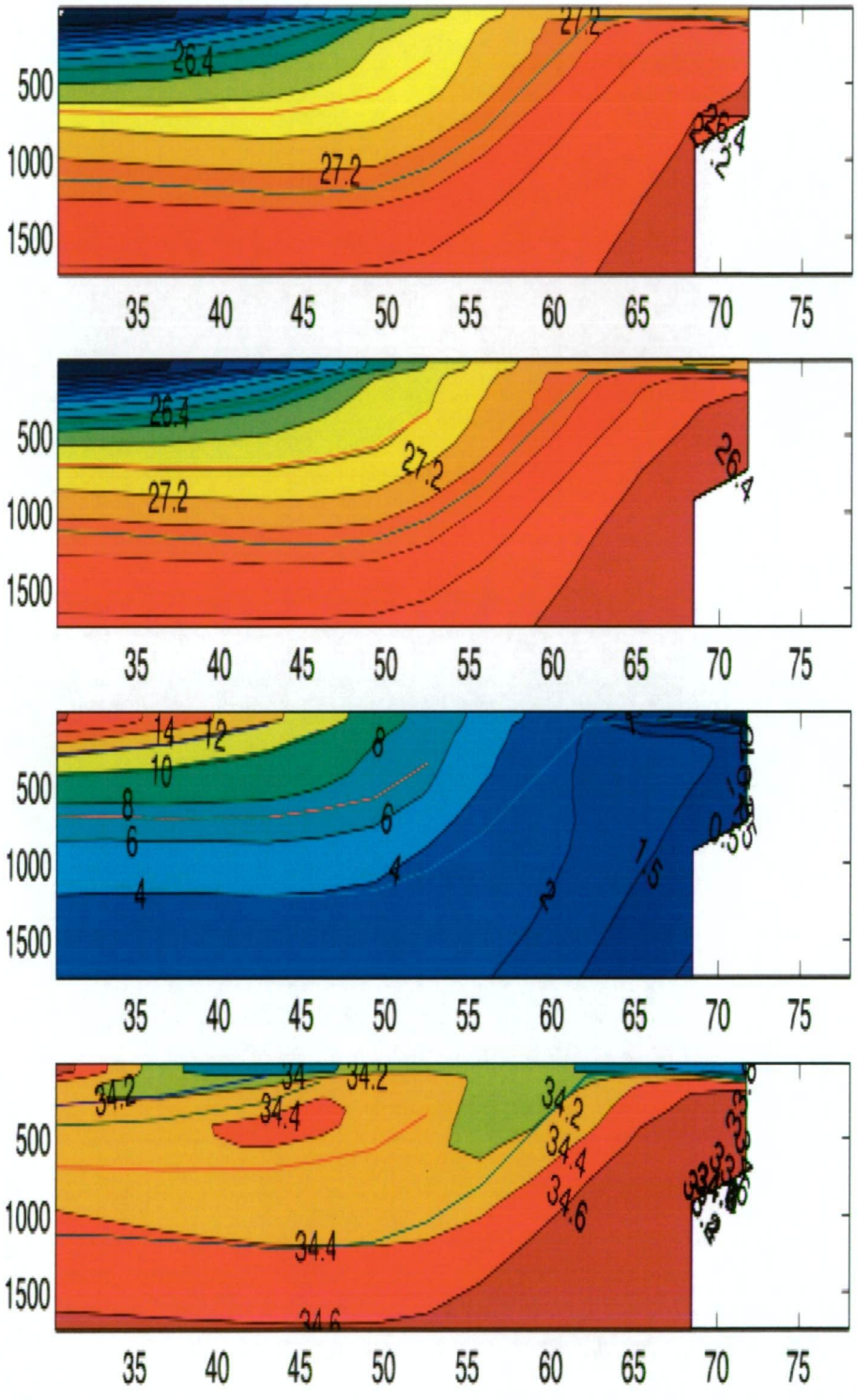

Figure 2.9: Wintertime properties along 270°E (for depths to 1500 m) in July 1880. Upper panel is density (kg.m^{-3}). Second panel is neutral density (kg.m^{-3}). Third panel is potential temperature (°C) and the lower panel is salinity (psu). Horizontal axis is Longitude (°E) and vertical axis is Depth (m).

are 27 to 27.4 kg.m^{-3}, 2 to 10°C and 34 to 34.8 psu respectively. North of SAMW, there is a layer of central water or subtropical gyre water that is just visible on these sections.

The region of thick wintertime mixed layer in the model (SAMW formation) continues east to at least 130°E but moves further south (Figure not shown). This is caused by the ACC moving south due to the presence of the Australian landmass. Further east at 180°E in the Pacific Sector (Figure 2.8), the wintertime thick mixed layer is indicated by isopycnals that outcrop. However there is still a layer of thick subsurface layer of unstratified water between 37 and 47°S. This suggests SAMW has advected from the west, from the formation regions to the west. The ranges for density, temperature and salinity for SAMW and AAIW respectively are 26.6 to 27.0 kg.m^{-3}, 7 to 10°C, 34.3 to 34.6 psu and 26.8 to 27.6 kg.m^{-3}, 1 to 8°C, 34 to 34.6 psu .

Following the ACC into the East Pacific Sector of the Southern Ocean, the water column has freshened (Figures 2.8 to 2.9). There is a small region between 45 and 55°S and depths 100 and 700 m where density and temperature are somewhat unstratified. This represents the advected SAMW and shows properties with ranges 26.8 to 27.1 kg.m^{-3}, 6 to 8°C and 34.2 to 34.4psu. The AAIW salinity minimum tongue appears to occur at the surface (and to depths of aver 1000 m) south and directly adjacent to the SAMW. Density, temperature and salinity ranges are 27 to 27.8 kg.m^{-3}, <0 to 9°C, and 34 to 34.6 psu. Approaching the Drake Passage (Figure 2.9), south of 50°S, surface stratification increasingly weakens. This coincindes

with fresh surface waters (source of AAIW) occurring further North. As a result, the South-East Pacific region is an important source region of AAIW. According to literature (discussed in chapter 1), these cool fresh waters in the southeast Pacific are an important source of AAIW and were originally SAMW which has been modified as it is advected westwards. The SAMW is formed by wintertime mixing in the Indian to western Pacific (around 50 to 150°E) and is subjected to subsurface advection and gradual modification and is subducted in the South East Pacific.

A table of model water mass properties in various ocean basins (Table 2.1) has been created. The criteria for watermass identification is the existance of a thick wintertime mixed layer (SAMW) and the presence of a salinity minimum (AAIW). The table reveals that moving east from the Indian Ocean to the east Pacific Ocean, the SAMW minimum density increases and the maximum temperature and salinity both decrease. This is consistent with observed SAMW which is progressively cooler, fresher and denser moving east (McCartney, 1982).

Properties on neutral density surfaces

Upon a constant neutral density surface, properties of temperature, salinity and pressure change predominantly across ACC. Figures 2.10 to 2.15 show temperature and pressure on a neutral surface in the Southern Ocean. On density surface 26.5 $kg.m^{-3}$ temperature (and salinity) are highest throughout the Atlantic and Indian Oceans and decrease east through the Pacific (Figure 2.10). The corresponding depth of the surface show that the surface

is deepest in the Indian Ocean Region (Figure 2.11). On surface 27 kg.m^{-3}, temperature (Figure 2.12) are largest in the Indian Ocean north of 45°S. Along the outcropping of the surface, temperature (and salinity) are lowest in the Atlantic Sector and gradually increase moving east through the Indian and Pacific Sectors of the Southern Ocean. This surface is most shallow in the Atlantic Ocean Sector where low temperatures are also seen (Figure 2.13). On a deeper surface (27.5 kg.m^{-3}) we see a similar pattern except the pressure difference is not as large between the Atlantic Ocean and other oceans as seen on shallower surfaces (Figures 2.14 and 2.15).

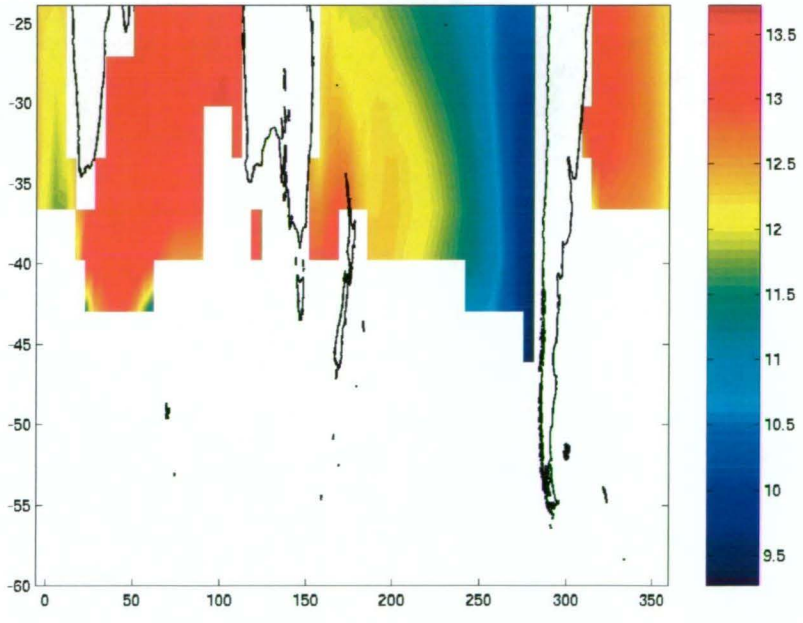

Figure 2.10: 100 year mean potential temperature (°C) on neutral density surface $\gamma = 26.5$ kg.m^{-3}.

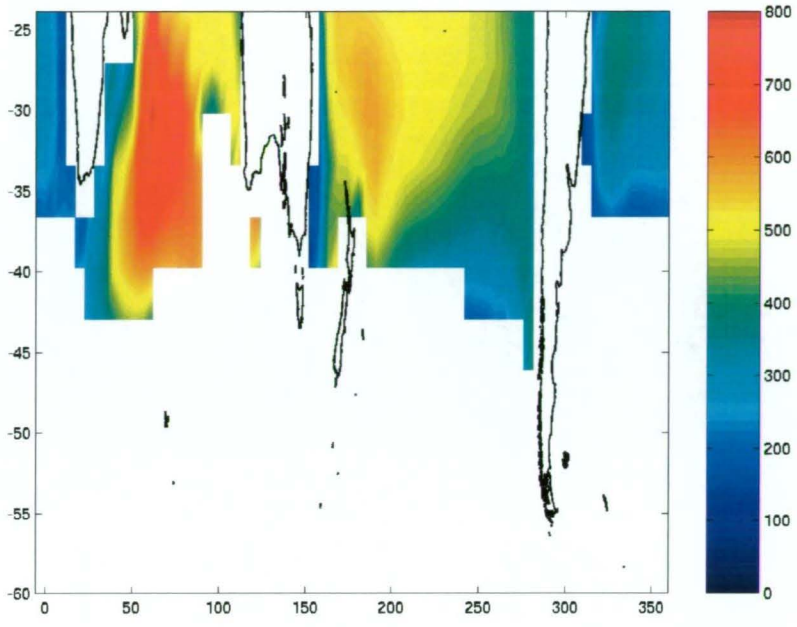

Figure 2.11: 100 year mean pressure (dbar) on neutral density surface $\gamma = 26.5$ kg.m^{-3}.

Mixed Layer Depth

A diagram of the estimated mixed layer depth (Figure 2.16) is used to confirm the above results that identify SAMW and AAIW formation regions. Winter mixed layer depth is a useful indicator of vigorous surface layer processes and preconditioning for overturn (Talley, 1999). We estimate the mixed layer depth as a 0.1 kg.m^{-3} density change from the surface. The deepest mean mixed layer depths occur in the South East Indian Ocean as well as below Australia and in the South East Pacific Ocean. These regions are identical to the regions which we identified as SAMW/AAIW source regions from an examination of meridional sections. Also, the thick mixed layer depths agree with the description by McCartney (1977) of observed thick mixed

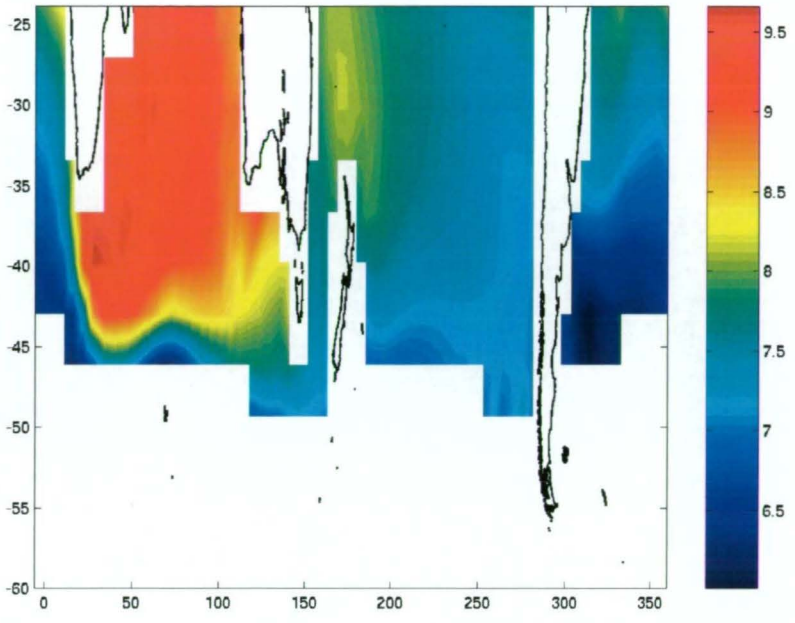

Figure 2.12: 100 year mean temperature (°C) on neutral density surface $\gamma = 27$ kg.m^{-3}.

layers and SAMW sources. The RMS variability in the mixed layer depth shows variability is high about the ACC with peaks in the region south of Australia (SAMW formation). This indicates there is change in the strength of wintertime convection that occurs each year. This phenomena is discussed further in future chapters on variability.

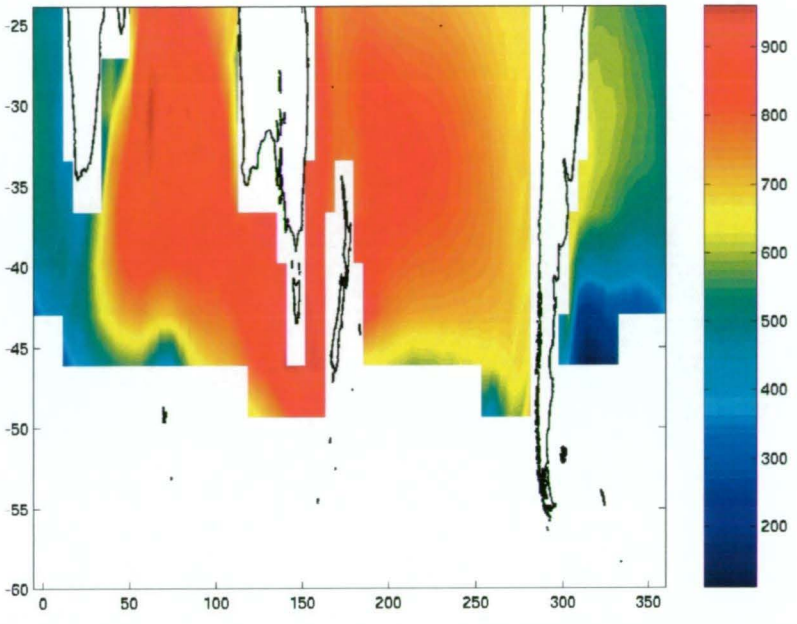

Figure 2.13: 100 year mean pressure (dbar) on neutral density surface $\gamma =$ 27 kg.m^{-3}.

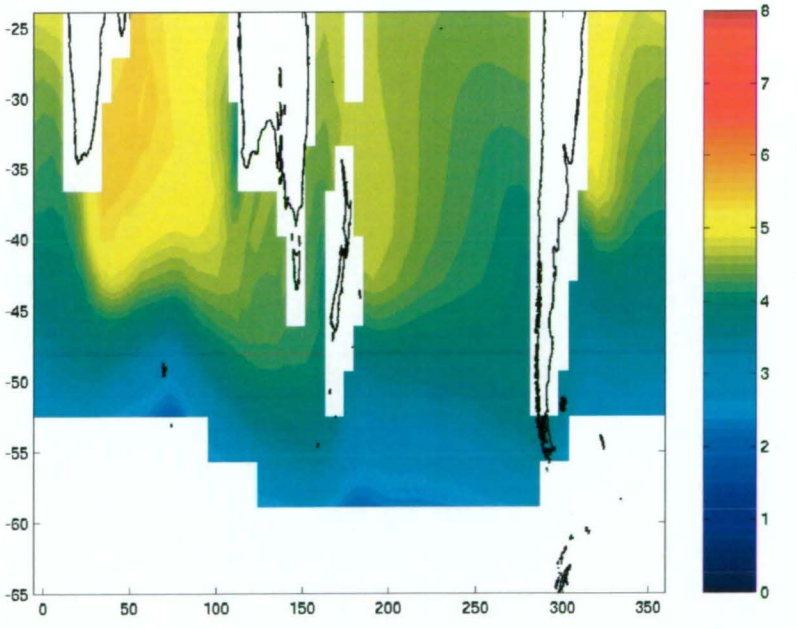

Figure 2.14: 100 year mean temperature (°C) on neutral density surface $\gamma =$ 27.5 kg.m^{-3}.

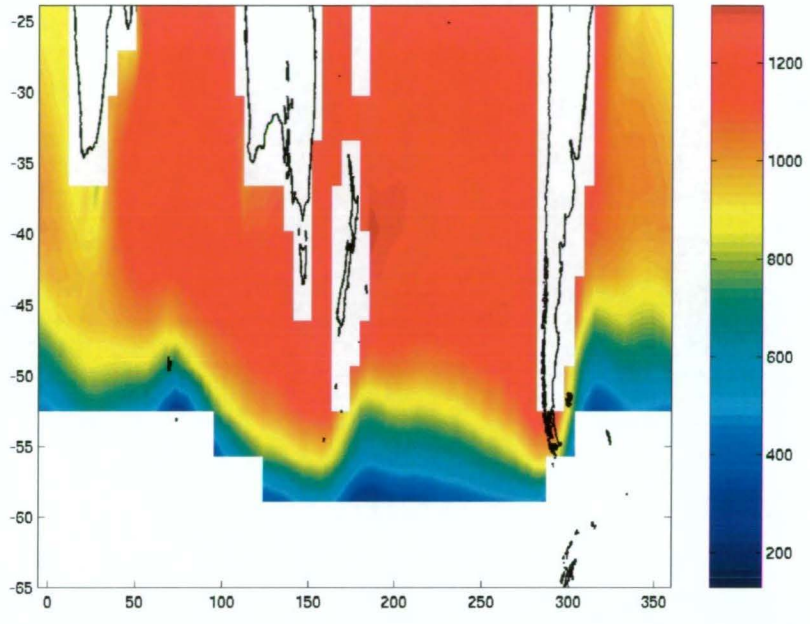

Figure 2.15: 100 year mean pressure (dbar) on neutral density surface $\gamma = 27.5$ kg.m^{-3}.

SAMW (Lat range)	Density (kg.m^{-3})	Temperature (°C)	Salinity (psu)
80°E Indian (35-50°S)	26.0 to 27.2	4 to 16	34.1 to 35.1
180°E Pacific (37-47°S)	26.6 to 27.0	7 to 10	34.3 to 34.6
270°E Pacific (45-55°S)	26.8 to 27.1	6 to 8	34.2 to 34.4
AAIW			
80°E Indian	27 to 27.4	2 to 10	34 to 34.8
180°E Pacific	26.8 to 27.6	1 to 9	34 to 34.6
270°E Pacific	27 to 27.8	< 0 to 8	34 to 34.6

Table 2.1: Density, Temperature and Salinity of SAMW and AAIW at various locations in the Indian and Pacific Oceans.

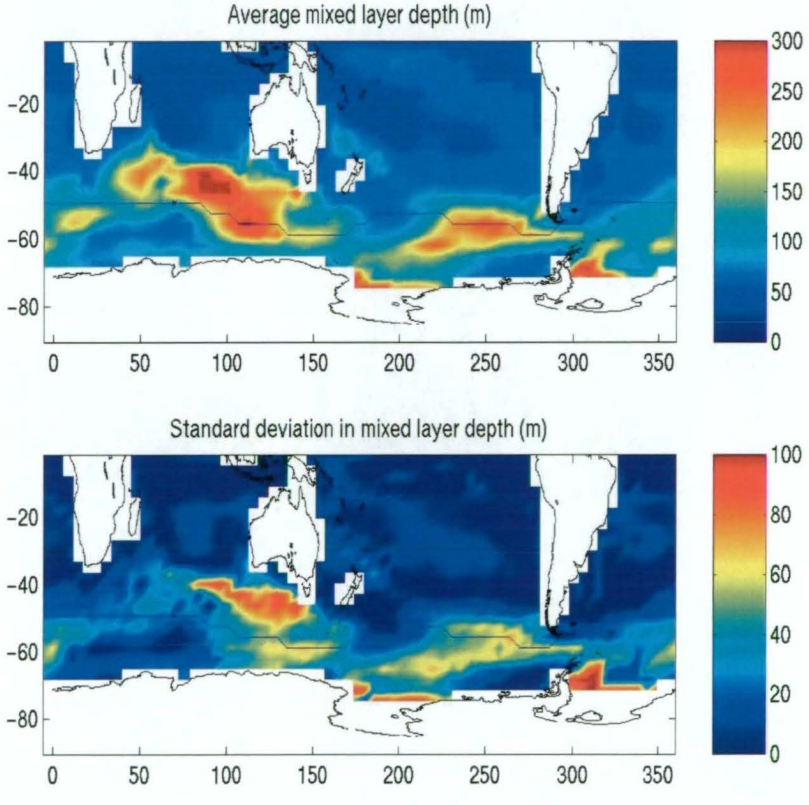

Figure 2.16: Mean (upper panel) and RMS variability (lower panel) of mixed layer depth (m) over 100 years.

Chapter 3

Variability and spatial propagation of anomalies in the Antarctic Circumpolar Current

In Section 3.1 we carefully select a number of paths that are representative of the ACC flow. For each of these paths we create Hovmoeller diagrams of temperature to determine the propagating component. Further, we use a box filter and Fourier analysis to filter anomalies into various frequencies which are also displayed as Hovmoeller diagrams.

In Section 3.2 we examine the propagation of potential temperature anomalies as compared to the current speed. Using Hovmoeller diagrams from Section 3.1, we define a 'persisting' and 'tracked' anomaly as one which exists for at least 10° of longitude. The speed of the anomaly is then calculated and plotted against the average current speed along the anomaly path. The

resultant scatterplot is used to discuss means for propagation of anomalies in the ACC.

3.1 Spatial Propagation of signals along 1 dimensional paths

To examine the spatial propagation of signals and the existence of ACW-like propagating anomalies I employ a number of methods. First, an important stage involves determining the analysis region for the ACW. This involves choosing an appropriate path in the horizontal plane, in which to analyse vertical sections. Secondly, Hovmoeller diagrams are created using anomalies along the chosen paths. Hovmoeller plots is one method that allows us to identify whether anomalies show propagation.

Stage 1- Choosing a path: Is maximum u at 400 m an appropriate choice?

Here I choose a 1 dimensional path in the xy plane suitable for tracking ACW-like interannual propagating anomalies. First I select a line of constant latitude. This replicates various studies of the observed ACW. Plotting anomalies along latitude 55°S (not shown), shows that anomalies do persist (propagate), but there are numerous discontinuities. These discontinuities indicate that choosing a line of constant latitude does not sufficiently allow for north/south variations of the ACC in the Southern Ocean. Therefore,

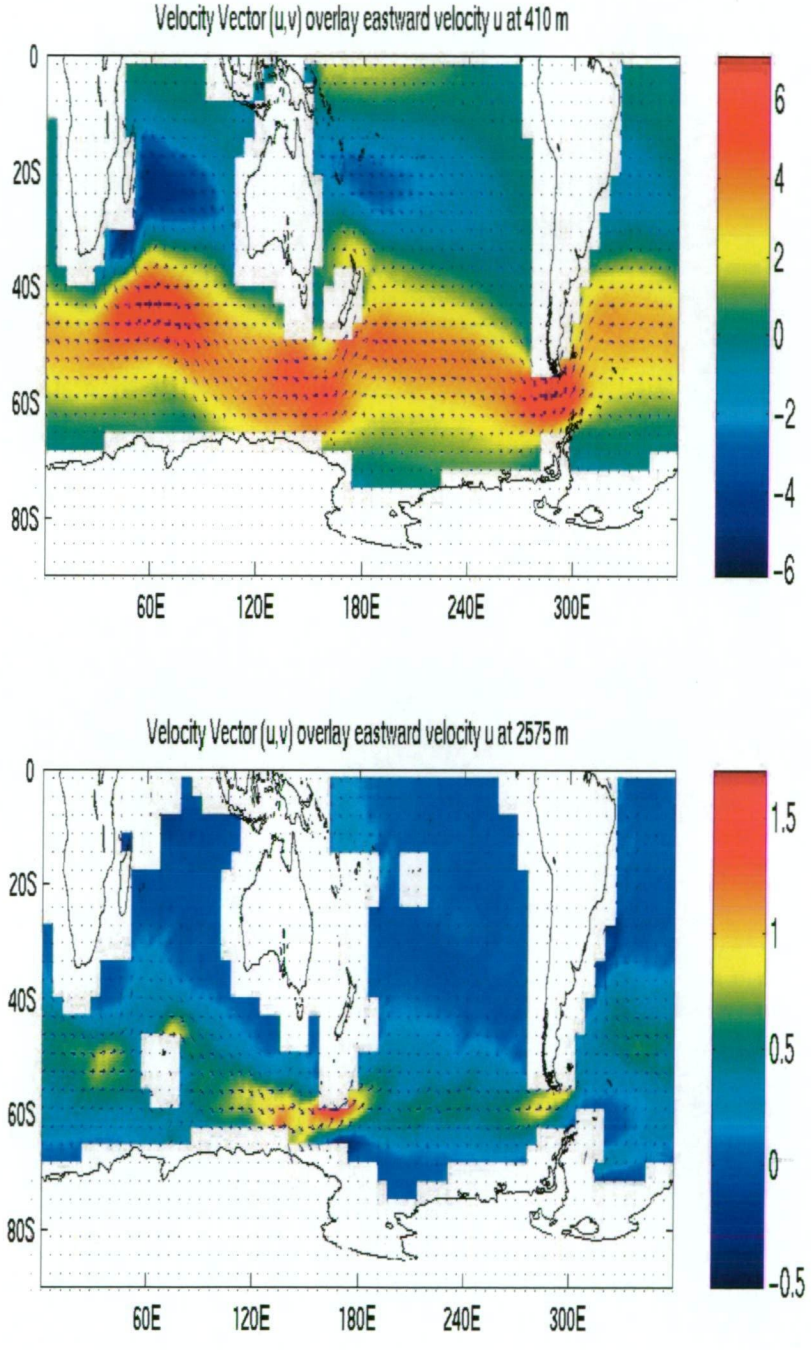

Figure 3.1: Velocity vector (arrows) ($cm.s^{-1}$) overlaying strength of the eastward velocity (colour map) ($cm.s^{-1}$) at 410 m depth (Upper panel) and 2575 m (Lower Panel). Values are an annual mean of 1880 from the c12 control model run.

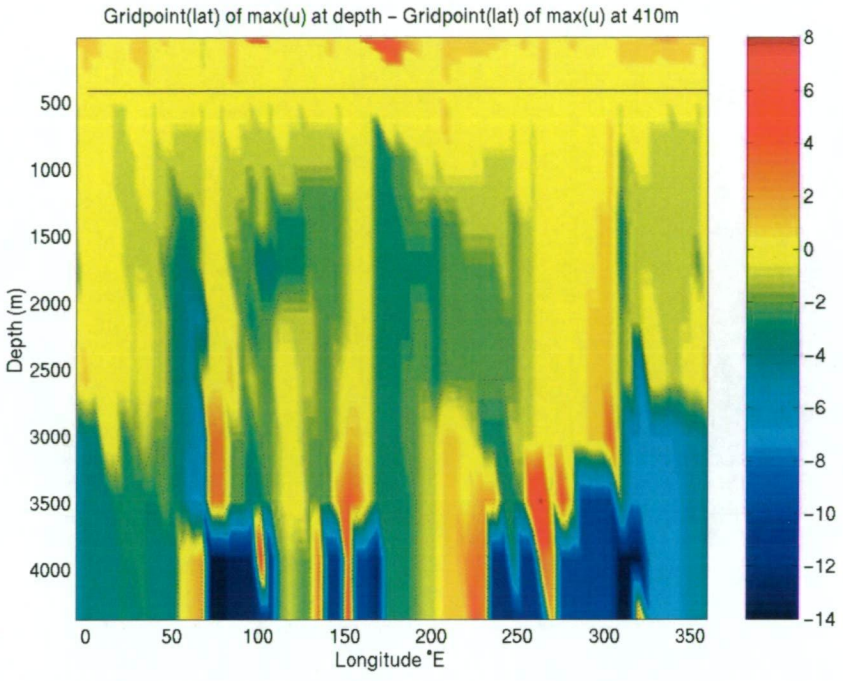

Figure 3.2: Number of latitude gridpoints that the position of the maximum eastward velocity (for each depth) varies from the latitude position of the maximum eastward velocity at 410 m depth. Values are calculated using 64 year mean values from the c12 control model.

next I choose a suitable path in the xy plane along which anomalies are more likely to propagate.

A more suitable path is defined by the maximum of mean eastward velocity (u) at a chosen depth. To choose an appropriate depth I use a simple plot. Figure 3.1 shows the average u (using 64 years), as well as velocity vector (u,v) at 410 m and 2575 m. The peaks (for u at least) occur at similar latitudes for both depths. This indicates that using the latitude location of maximum u at 410 m may be an adequate representation of the latitude of maximum u at depths to around 2000 m.

What about other depths? Figure 3.2 compares the latitude of maximum

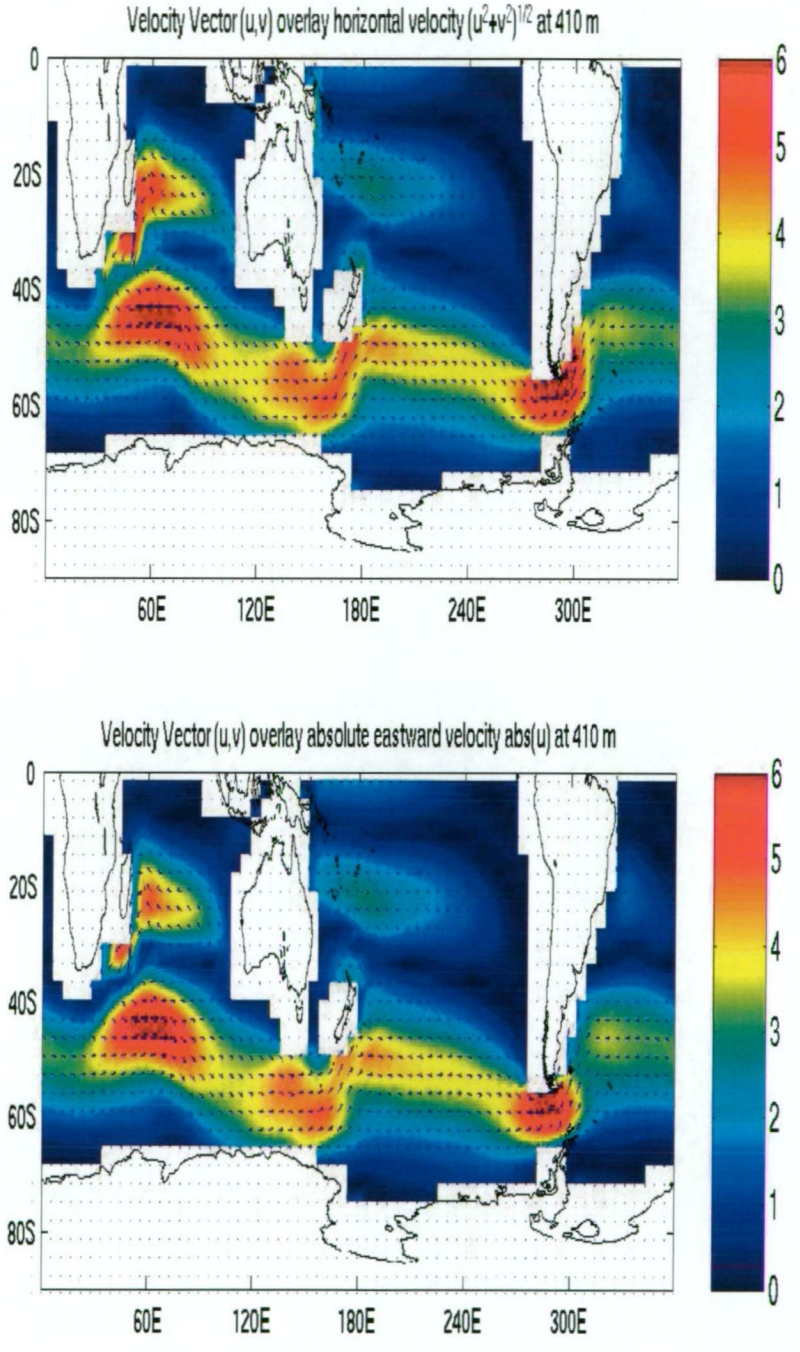

Figure 3.3: Upper Panel: Velocity vector (arrows) ($cm.s^{-1}$) at 410 m depth overlaying the magnitude of the velocity vector (colour map) ($cm.s^{-1}$) at 410 m depth. Lower Panel: Velocity vector (arrows) ($cm.s^{-1}$) at 410 m depth overlaying strength of the eastward velocity (colour map) ($cm.s^{-1}$) at 410 m depth. Values are an annual mean of 1880 from the c12 control model run.

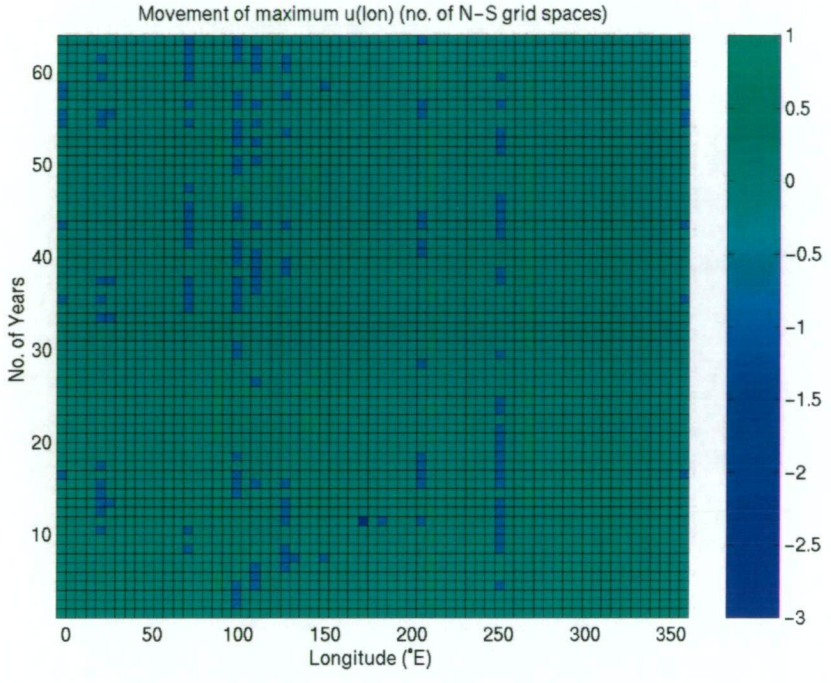

Figure 3.4: Number of latitude grid points that the position of the maximum easterly velocity (for each of 64 years) moves from the latitude position of the maximum easterly velocity of the mean easterly velocity of 64 years of the c12 control model.

u for all depths with the path of maximum u at 410 metres. The dashed contours indicate where the difference between locations exceeds 2 latitudinal grid points. At depths to about 3000 metres, the location of maximum(u) does not generally move beyond 2 gridpoints, except at around 50, 100, 200 and 300°E. Below 3000 m, the bottom topography tends to control the current flow patterns at these depths. We consider the reasons why for the depths where the latitude of maximum u is further than two grid points from the latitude of maximum u at 410 m (50, 100, 200 and 300°E). For the regions around 200 and 300°E (at least), there is a large north/south component of velocity in the ACC (can be seen in Figure 3.1). At depth, these strong currents tend to decrease rapidly, thereby moving the location of strongest

eastward flow and this may be a dominant factor.

To explore further, I compare maximum eastward velocity (u) to maximum horizontal velocity (u, v). Figure 3.3 displays the magnitude of horizontal velocity in the top diagram and the absolute magnitude of east velocity in the lower diagram. They are virtually identical. The difference between them is that the peaks are slightly more spread out for maximum horizontal velocity. This result slightly favours the use of the zonal component of current as opposed to the magnitude of the current. This is because numerical routines used to choose the correct path will be simpler as the peaks are more clearly defined.

Hence, I use a path based upon the average maximum(u) at 410 m to explore the next question: Is the location of mean maximum u sufficient, alternatively, how much does maximum u vary in space and time? To answer this question, Figure 3.4 plots the movement of maximum u (as a function of longitude and time) as the number of latitudinal grid points from the mean latitudinal grid point position. The maximum observed movement is 3 latitude grid points, which occurs only once in 64 years. The average variation is by 1 grid point. This suggests that in space, maximum u usually varies between ± 1 gridpint.

You will notice that at some longitudes (eg. 100 and 250°E) maximum u will consistently move one grid space north (or south). Intuitively, this is unexpected - since we are using an average value we expect there to be movements both north and south. This occurs because as the mean value

we are using the maximum of mean u, not mean maximum u. This problem is fixed by either choosing maximum u from more than one meridinal grid points; or calculating maximum u for each year, then averaging. The first method is a sound method for analysis of vertical sections. It requires slightly more computational work for all vertical analysis (since all properties need to be averaged over two latitudes).

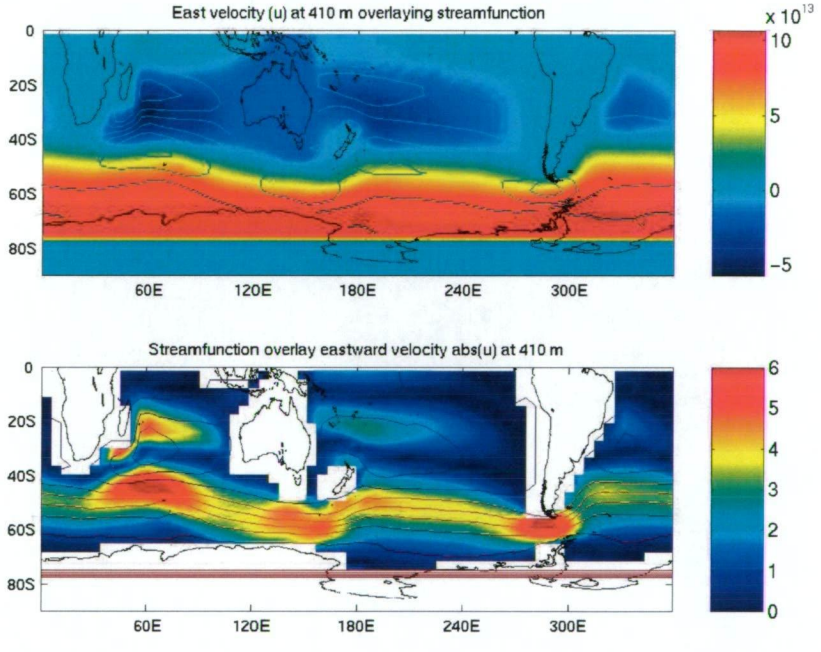

Figure 3.5: Upper Panel: Contours of constant values of eastward velocity ($cm.s^{-1}$) at 410 m depth overlaying the magnitude of the depth integrated streamfunction (colour map) ($cm^3.s^{-1}$) at 410 m depth. Lower Panel: Contours of constant values of depth integrated streamfunction ($cm^3.s^{-1}$) at 410 m depth overlaying the magnitude of the eastward velocity ($cm.s^{-1}$) (colour map) at 410 m depth. Values are an annual mean of 1880 from the c12 control model run.

I now also consider streamfunction as a path for tracking anomalies. To choose a streamline of transport, I overlay streamlines with velocity vectors (see Figure 3.5). The $5x10^{13}$ ($cm^3.s^{-1}$) streamline has a high degree of overlap

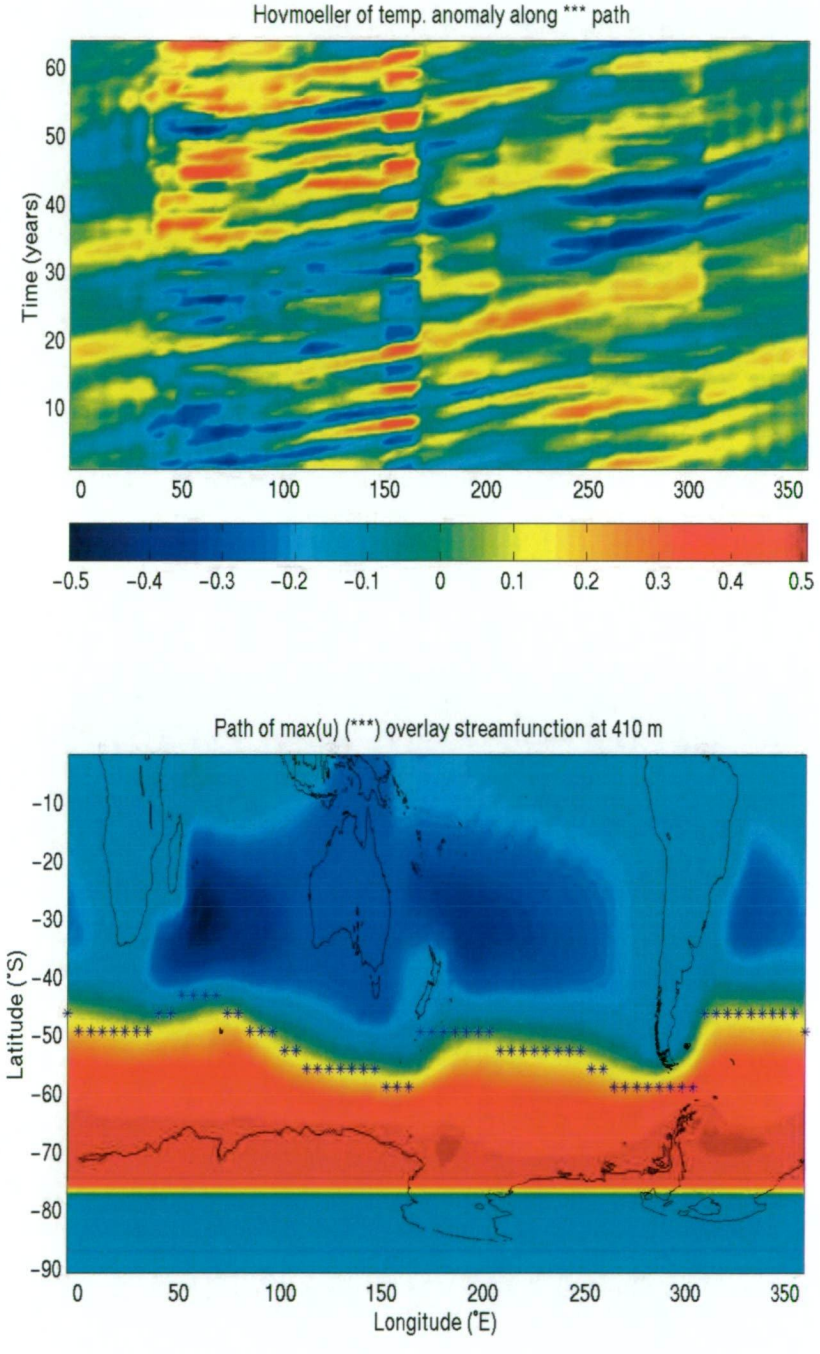

Figure 3.6: Upper panel: 64 year Hovmoeller diagram of potential temperature anomaly at 410 m along a chosen path based upon the maximum easterly current speed. Lower panel: The location of the maximum eastward velocity (for each longitude) (indicated by *) overlay the magnitude of the depth integrated streamfunction (colour map) ($cm^3.s^{-1}$) at 410 m depth. Values are from the c12 control model run.

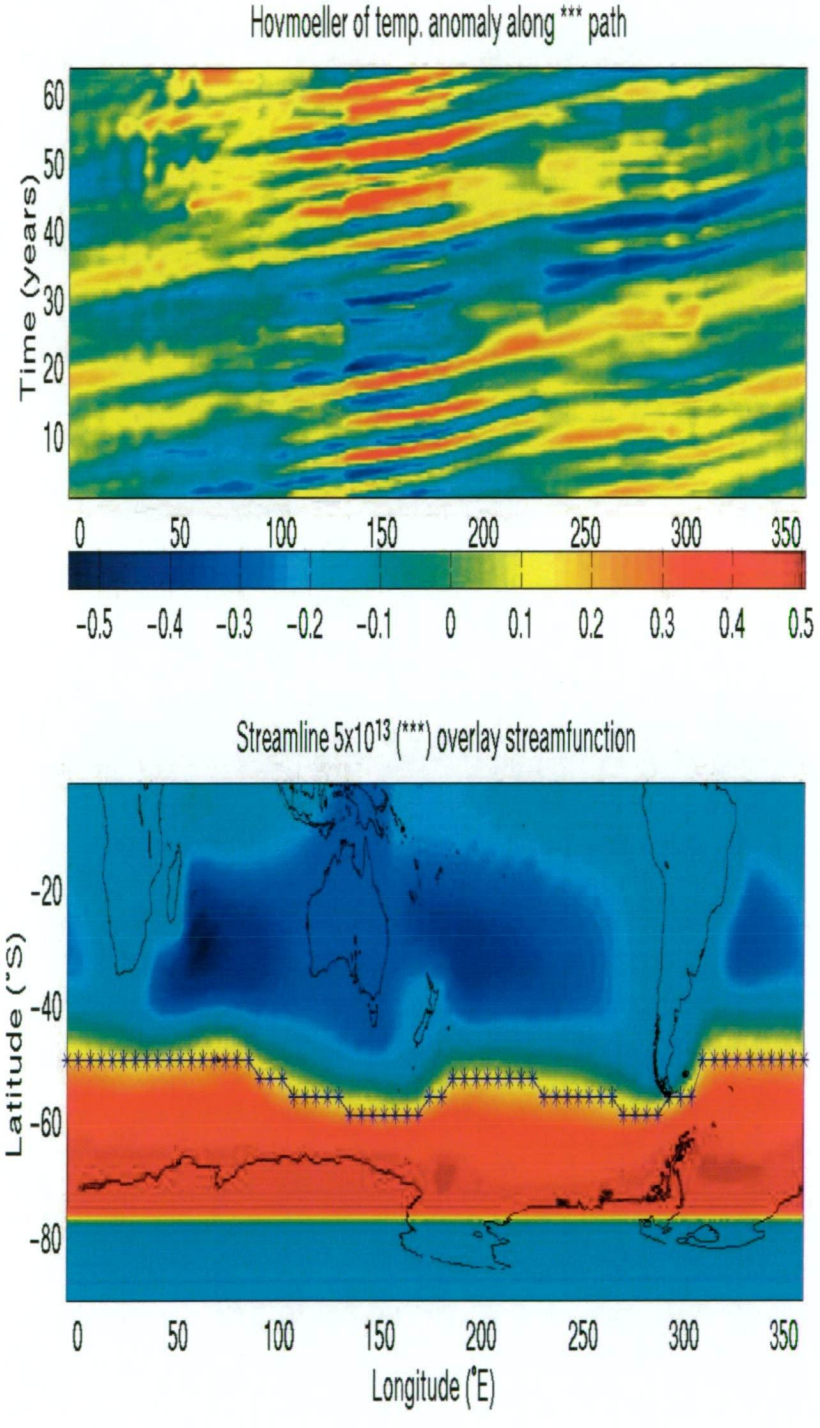

Figure 3.7: Upper panel: 64 year Hovmoeller diagram of potential temperature anomaly at 410 m along a chosen path based upon the 64 year mean position of the $5x10^{13}$ ($cm^3.s^{-1}$) depth integrated streamfunction. Lower panel: The location of the $5x10^{13}$ ($cm^3.s^{-1}$) depth integrated streamfunction (for each longitude) (indicated by *) overlay the magnitude of the depth integrated streamfunction (colour map) ($cm^3.s^{-1}$) at 410 m depth. Values are from the c12 control model run.

with the path of maximum u but is a smoother path. The $5x10^{13}$ ($cm^3.s^{-1}$) streamline most closely overlays the max(u) path and is chosen. This streamline is displayed with yellow colour scheme in Figure 3.5. To examine how anomalies propagate along the paths, we plot temperature anomalies along (1) maximum u and (2) streamfunction.

Figure 3.6 shows potential temperature anomalies along maximum u at 410 m. There are strong ACW-like anomalies (ie. anomalies with timescales 4-5 years). The speed of the ACW appears relatively constant throughout the circumnavigation. The Figures highlight a problem in choosing just one latitude for maximum u (as opposed to averaging over 2 or more latitudonal grid points). Between approximately 150° and 160°E, maximum u moves relatively far south. The corresponding anomalies show that the strength of anomalies to be far stronger here than at neighbouring longitudes. Some anomalies also appear to originate here. This indicates that the maximum u goes too far south in this region to properly show anomaly propagation.

Temperature anomalies, at 410 m and along the streamline are shown in Figure 3.7. The anomalies are more regular than those seen on maximum u, in that there are less discontinuities and perhaps a smaller range of wave speeds. Wave generation appears to occur below Australia at about 130°E. In answer to the question: 'Is maximum u at 400 m an appropriate choice?', this discussion suggests that an averaged streamline is a more appropriate choice, particulary for examining propagating anomalies in the 4-5 year time scale range. The Hovmoeller diagrams both showed propagating anomalies

with time scales 4-5 years. These are similar to observed anomalies (ACW) seen in the Southern Ocean. On both paths, the anomalies also clearly show strong variance on a longer timescale. This longer timescale is around 40 years, as there is around 1.5 cycles visible in the 64 year time series.

Summary.

Using a variety of different paths we are able to identify propagating anomalies in the Southern Ocean at 410 m (at least). These anomalies show dominant time scales similar to that of ACW. Use of a streamline (which was close to the maximum u flow), showed anomalies with the most fluid propagation. Around the ACC there were regions where the magnitude of anomalies peaked, indicating source regions for the variability. These regions included south of Australia at around 130°E. There is also strong variability on time scales around 40 years.

3.2 Anomaly propagation in the Antarctic Circumpolar Current

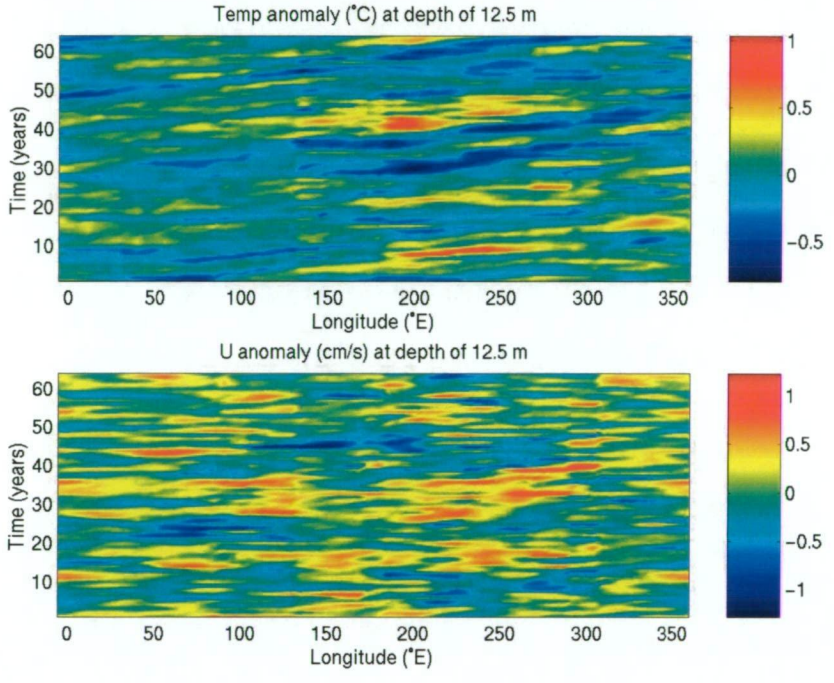

Figure 3.8: Upper panel: 64 year Hovmoeller diagram of potential temperature anomaly at 12.5 m along a chosen path based upon the 64 year mean position of the $5x10^{13}$ ($cm^3.s^{-1}$) depth integrated streamfunction. Lower panel: 64 year Hovmoeller diagram of eastward velocity anomaly at 12.5 m along a chosen path based upon the 64 year mean position of the $5x10^{13}$ ($cm^3.s^{-1}$) depth integrated streamfunction.

In this section I examine the speed of propagating anomalies and compare this to the current speed.

Initially 3 depths are chosen for comparison: 12.5, 410 and 2125 m. First of all, the temperature anomaly is plotted at 12.5, 410 and 2125 m (see Figures 3.8, 3.9 and 3.10). There is a substantial drop in wave speed from 410 to 2125 m. At 2125 m the period exceeds the data set length (64 years). The

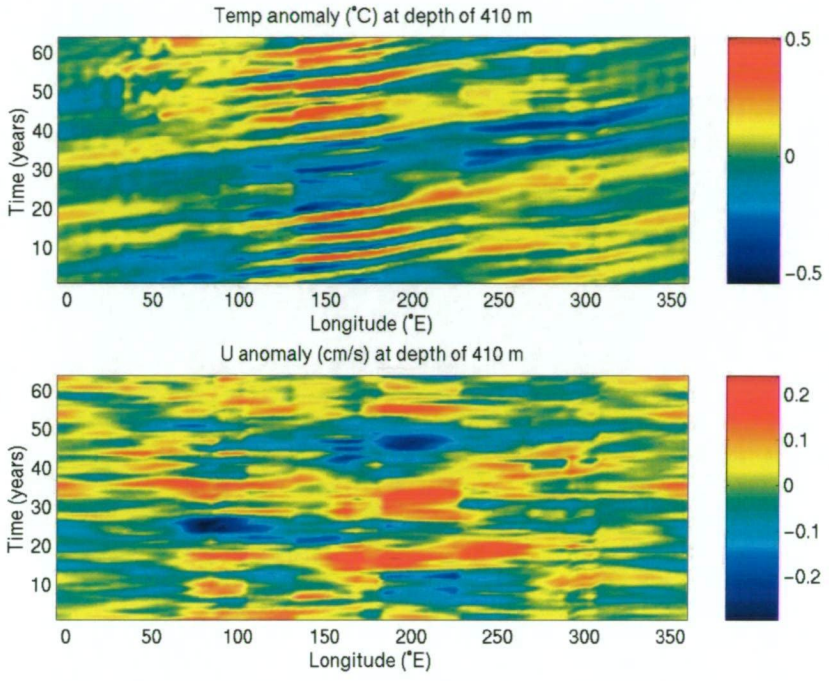

Figure 3.9: Upper panel: 64 year Hovmoeller diagram of potential temperature anomaly at 410 m along a chosen path based upon the 64 year mean position of the $5x10^{13}$ ($cm^3.s^{-1}$) depth integrated streamfunction. Lower panel: 64 year Hovmoeller diagram of eastward velocity anomaly at 410 m along a chosen path based upon the 64 year mean position of the $5x10^{13}$ ($cm^3.s^{-1}$) depth integrated streamfunction.

variability of ACC velocity also decreases considerably: at 410 m anomalies show a range of about ($\pm 0.2\ cms^{-1}$) to a range of about ($\pm 0.1\ cms^{-1}$) at 2125 m. This drop in variabilty is due, at least in part, to the drop in absolute velocities of the ACC with depth. So, ACW and ACC speeds decrease with depth. The question to now address is: Is the speed of the ACW a function of ACC speed?

From the Hovmoellers plots of temperature a number of propagating anomalies are chosen. I select initial and final locations of propagating anomalies with longitudes (x) and times (t): (x_i, t_i) and (x_f, t_f). Wave speeds are de-

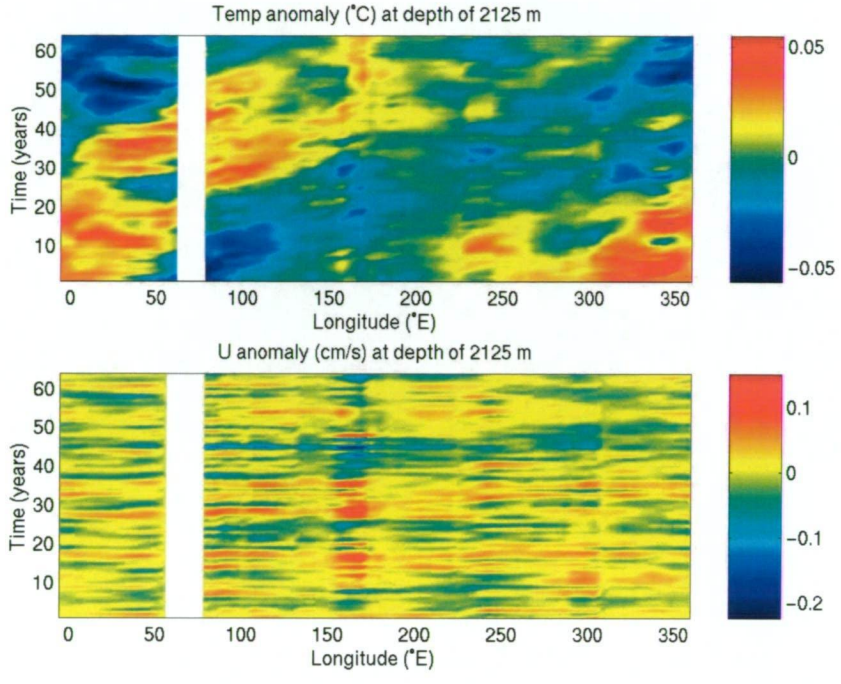

Figure 3.10: Upper panel: 64 year Hovmoeller diagram of potential temperature anomaly at 2125 m along a chosen path based upon the 64 year mean position of the 5x10^{13} (cm^3.s^{-1}) depth integrated streamfunction. Lower panel: 64 year Hovmoeller diagram of eastward velocity anomaly at 2125 m along a chosen path based upon the 64 year mean position of the 5x10^{13} (cm^3.s^{-1}) depth integrated streamfunction.

termined using these coordinates. Wave speeds are plotted against a number of variables: easterly current velocity at the initial location of the anomaly ($u_i = u(x_i, t_i)$); easterly current speed at the final location of the anomaly $u_f = u(x_f, t_f)$; average current speed of the initial and final locations of the anomaly $u_m = u(x_m, t_m) = u(0.5(x_i + x_f), 0.5(t_i + t_f))$ and average current speed of all the prior $u_a = (u_i, u_f, u_m)$. Note there are some caveats using this simple method. First, I choose the most visually dominant anomalies, which gives a bias in results. Second, in choosing initial and final coordinates to represent the wave, an error arises due to manual choosing and intuitively

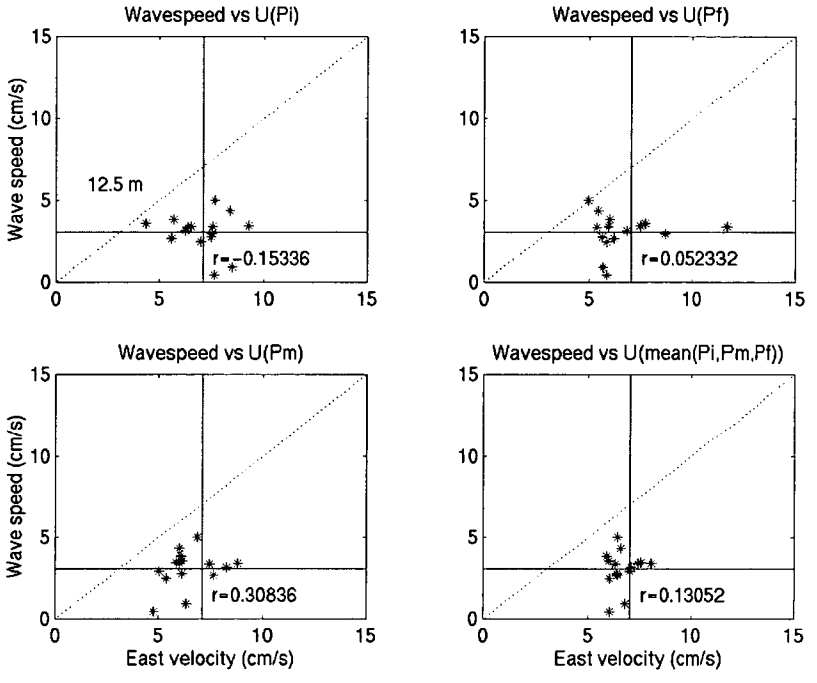

Figure 3.11: Scatter plots of anomaly propagation speed/wavespeed ($cm.s^{-1}$ at 12.5 m versus: eastward current speed at location of anomaly generation (upper left panel); eastward current speed at location of anomaly dissipation (upper right panel); eastward current speed at midpoint location between anomaly generation and dissipation; and mean eastward current speed calculated from the values at generation, dissipation and the midpoint.

trying to 'line them up' with other anomalies. In reality the true path is sometimes visually unclear. Therefore there is large enough error in the results that the Figures cannot be quoted for useful purposes. However, the results will provide the reader with qualitative descriptions that can be used to hypothesize on various processes which may be occurring.

The wave speeds are plotted against the variables: u_i, u_f, u_m and u_a. To determine where the strongest relationship exists. See Figures 3.11, 3.12 and 3.13 for 12.5, 410 and 2125 m. On each diagram there is a vertical line indicating average u along the streamline. This gives some idea of the

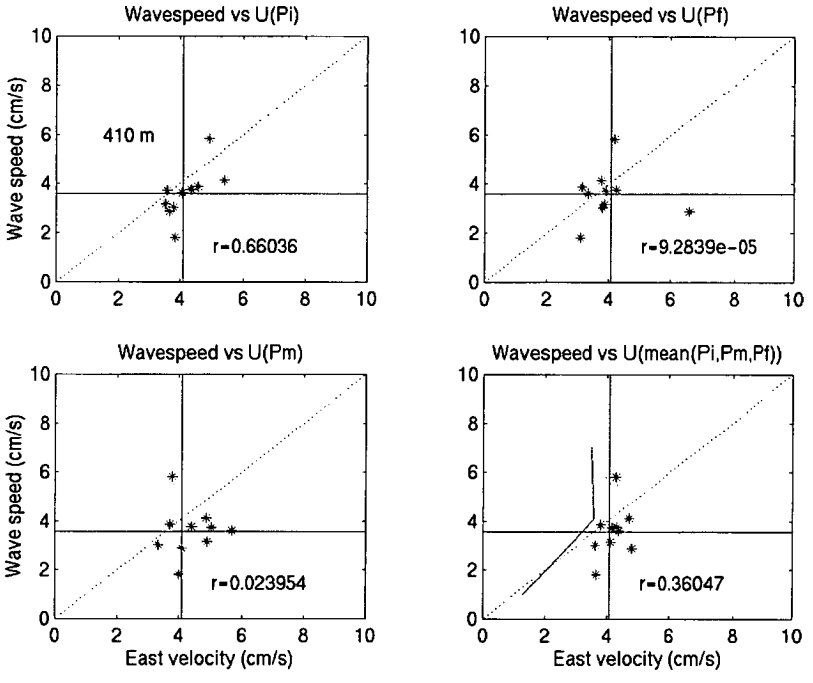

Figure 3.12: Scatter plots of anomaly propagation speed/wavespeed ($cm.s^{-1}$ at 410 m versus: eastward current speed at location of anomaly generation (upper left panel); eastward current speed at location of anomaly dissipation (upper right panel); eastward current speed at midpoint location between anomaly generation and dissipation; and mean eastward current speed calculated from the values at generation, dissipation and the midpoint.

relevance of the x axis values. There is also a horizontal line which displays the averaged wave speed. The diagonal line is to assist in determining how the ratio anomaly: ACC speeds compare to a perfect 1:1 relationship. At 410 m, u_a is about 4 cms^{-1} and mean anomaly speed is slightly less (about 3.5 cms^{-1}). At 2125 m both the mean u and mean anomaly speed are about 1 cms^{-1}. Obviously there is similarity between u_a and anomaly speed when comparing these two depths. At 410 m, there is a fair spread with the majority of points, showing that ACC > anomaly speed. As stated previously, these relationships are highly dependant on the choice of points,

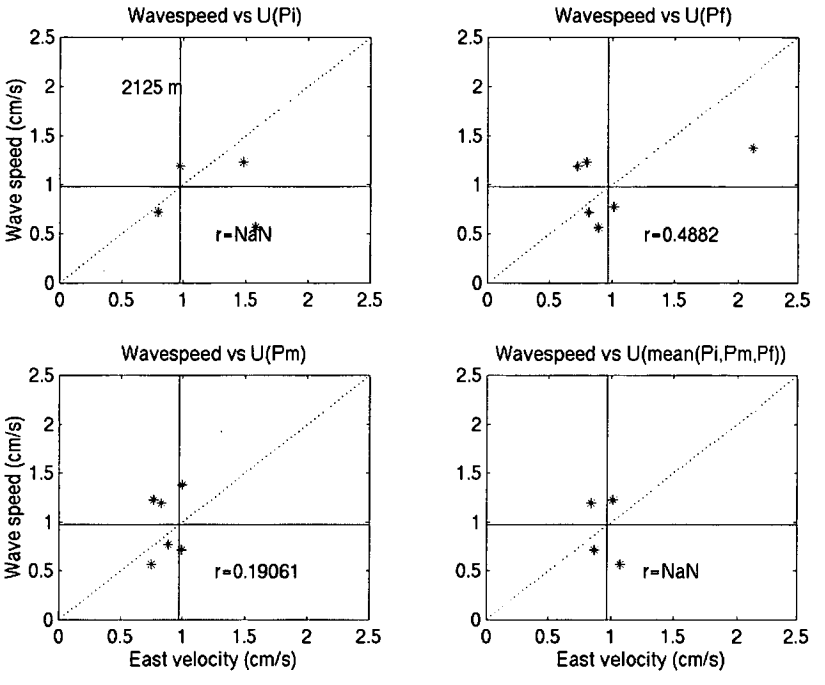

Figure 3.13: Scatter plots of anomaly propagation speed/wavespeed ($cm.s^{-1}$ at 2125 m versus: eastward current speed at location of anomaly generation (upper left panel); eastward current speed at location of anomaly dissipation (upper right panel); eastward current speed at midpoint location between anomaly generation and dissipation; and mean eastward current speed calculated from the values at generation, dissipation and the midpoint.

and are likely to vary each time a new finite set of points are chosen. The correlation values do not appear significant. This may be due to the error associated with the simple method used, or not enough data points, since one or two extreme points can largely determine the resulting correlation value.

Using this method, comparing anomalies with one of u_i, u_f, u_m, seems to give insignificant results. This may possibly be improved by choosing more data points, however, it seems that probably the best step from here is to determine an appropriate value for anomaly speed and compare this with u_a along the streamline for each depth. We do this for 4 different depths: 410,

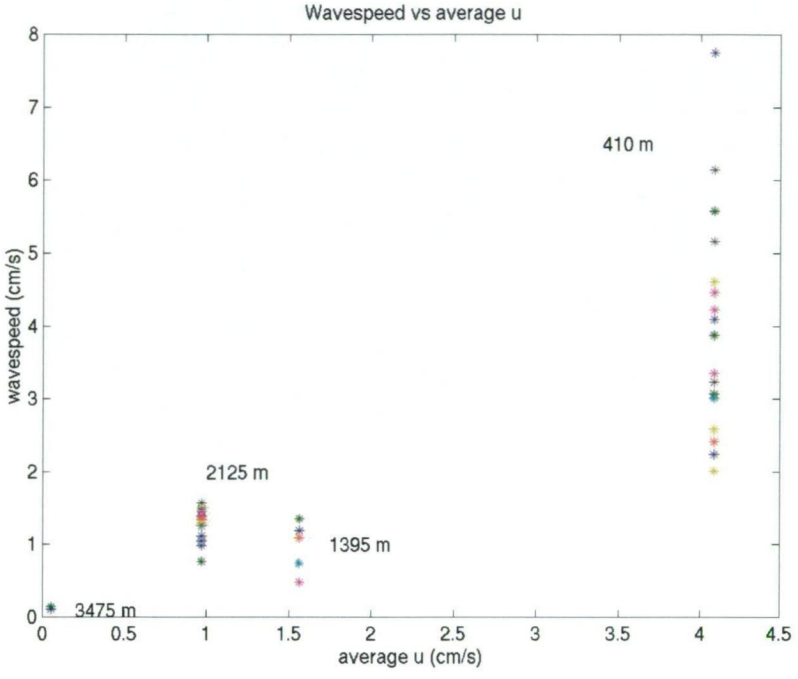

Figure 3.14: Wavespeed ($cm.s^{-1}$) versus mean eastward current speed (from east current at generation, dissipation and midpoint) for 12.5, 410 and 2125 m.

1395, 2125 and 3475 m. The results are compiled in Figure 3.14 showing wavespeed versus average u.

The results show that the comparison is not useful given the very different ranges of speeds at the different depths. Hence we repeat the experiment using only depths to 1400 m. Many propagating anomalies are identified and corresponding anomaly speed and easterly current speeds are plotted.

The scatter plot (see Figure 3.15) shows a clear relationship between ACC current speed and phase (anomaly) speed throughout the water column. The speed (period) of both signals decreases (increases) with depth. The correlation between current and anomaly speeds (see Figure 3.16) is strongest at intermediate depths (500 to 1500 m.). Here the anomalies are most strongly

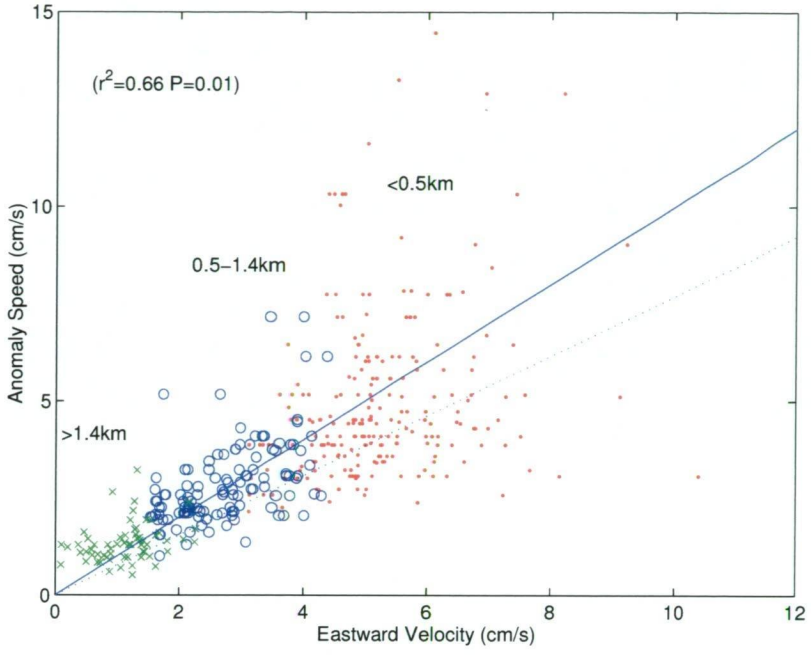

Figure 3.15: Scatter plot of estimated wavespeed/anomaly speed ($cm.s^{-1}$) and mean eastward current speed ($cm.s^{-1}$) (using eastward velocity at anomaly generation, dissipation and the midpoint). Crosses, circles and dots indicate anomalies occurring $>$ 1395 m, between 545 and 1130 m, $<$ 545m respectively. The regression line is shown as a dashed line below the 1:1 thick line.

advected and least subject to other influences such as convection, mixing and mid-ocean ridges.

Summary

Hence the results of this section indicate that propagating anomalies travel in the eastward direction generally slower than the easterly current speed. The anomaly speeds most resemble the current speed at the 410 m depth level, indicating that currents have a higher percentage of control over anomaly propagation than at other depths. At this depth there was a significant

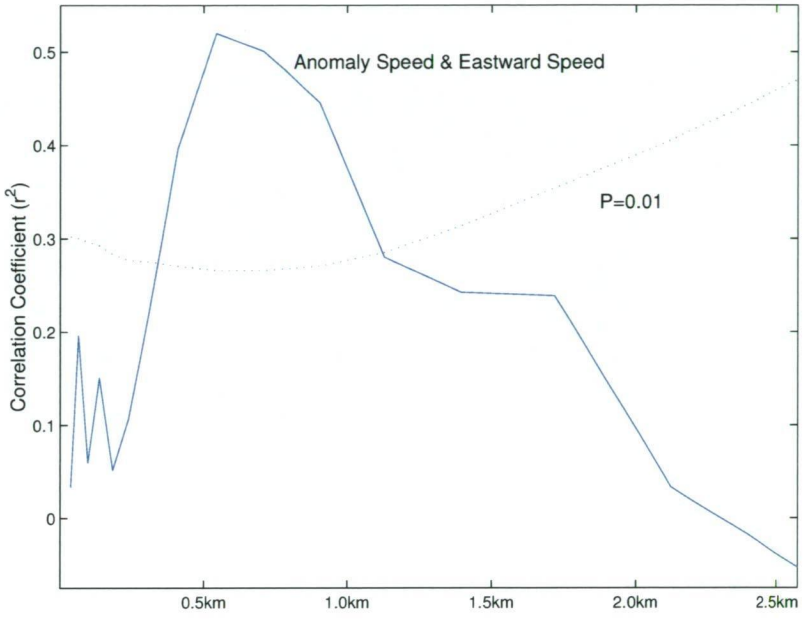

Figure 3.16: Correlation Coefficient between estimated wavespeed/anomaly speed (cm.s^{-1}) and mean eastward current speed (cm.s^{-1}) (using eastward velocity at anomaly generation, dissipation and the midpoint) versus depth (km). The 1% significance level is shown as a dashed line.

correlation between anomaly and current speed.

Chapter 4

Characterising natural variability of water masses in the modelled ocean.

Aims and Method

In this chapter I characterise the variability seen in two Southern Ocean water masses: Sub-Antarctic Mode Water and Antarctic Intermediate Water. The mean presence and properties of these water masses was described in Chapter 2. A number of methods are used to examine water mass variability. First, using a selection of depths and neutral density surfaces, I calculated RMS variability of temperature, salinity and pressure to determine spatial distribution of variance. Then, using a box filter and Fourier analysis, I filter the total variance into various period bands in order to identify dominant frequencies. After dominant frequencies and spatial regions are identified as

potential variability modes, the spatial and temporal evolution of statistical modes is analysed using Hilbert Empirical Orthogonal Functions (HEOFs). We calculated HEOFs of temperature, salinity and pressure anomalies aswell as time filtered anomalies of variability for SAMW and AAIW and their spatial and temporal evolution. A summary of the results is given in section 4.4.

4.1 Variability of Sub-Antarctic Mode Water

In this section I examine variability of temperature and salinity at depths of 12.5, 410 and 1130 m as well as heat flux and wind stresses at the sea surface. I do so to determine major spatial variance distributions and their dominant frequencies. Also, I will examine any obvious relationships between RMS temperature, salinity, heat flux, zonal and meridional wind variability.

RMS variability of potential temperature at various depths

Here I discuss the RMS variability of potential temperature as occurs on depth surfaces 12.5, 410 and 905 m. For each, I first consider the total RMS variability, then the variability contained within various period bands. The magnitudes of the RMS variability for each period are summarised in Table 4.1.

At 12.5 m, high variability in annually averaged temperature anomalies occurs in the Southern Ocean in a narrow latitude band and is largely circumpolar (Figure 4.1). One end of the band begins in the Pacific Sector at around

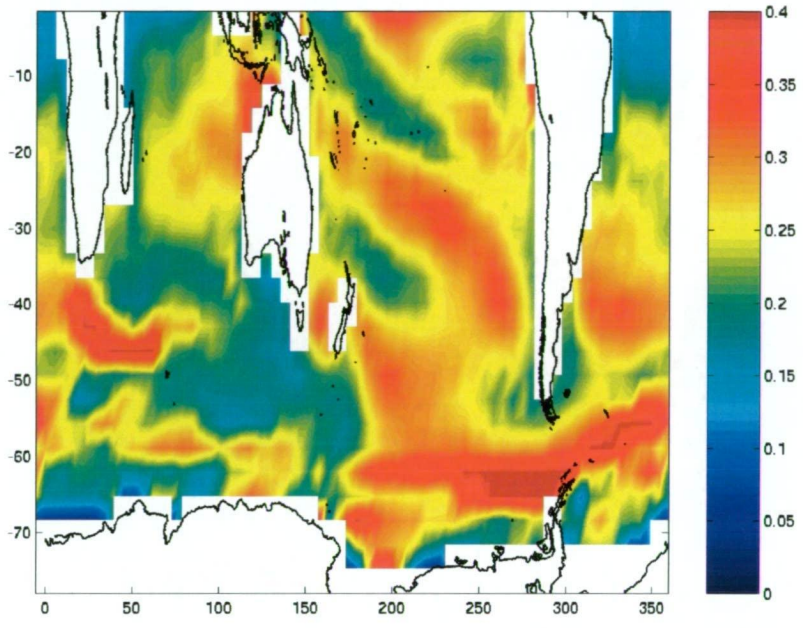

Figure 4.1: RMS variability of annually averaged potential temperature (°C) at 12.5 m depth level using control model years 1880-2179. Horizontal axis is Longitude (°E) and vertical axis is Latitude (°S).

60°S, 180°E. It continues east and then migrates northeast upon entering the Atlantic Sector. In the Indian Ocean sector the region of high variability is centred on the Agulhas retroflection which moves southeast until about 70°E where it moves northeast and eventually terminates at about 125°E. Much of this band coincides with the Agulhas western boundary current, suggesting that the Agulhas may be an important component in interannual anomaly

Band Pass Filter (years)	> 1	1 - 3	3 - 8	8 - 16	16 - 32	32 - 64
12.5 m	0.4	0.2	**0.25**	0.2	0.15	0.15
410 m	0.2	0.07	**0.15**	0.1	0.1	0.07
1130 m	0.06	0.01	0.025	0.025	0.025	n/a

Table 4.1: Typical magnitudes of RMS variability of annually averaged potential temperature (°C) at various depths and bandpass filters.

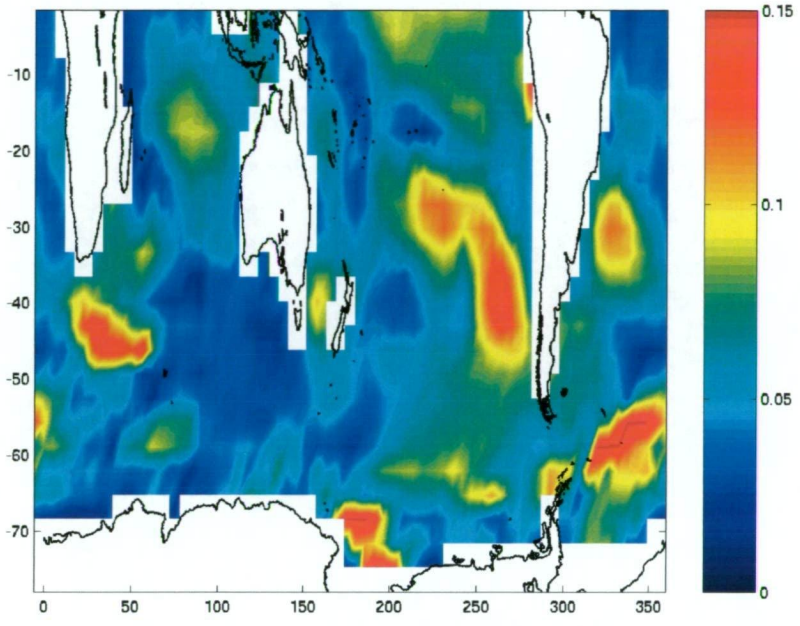

Figure 4.2: Filtered RMS variability (32-64 years) of annually averaged potential temperature (°C) at 12.5 m depth level using control model years 1880- 2179. Horizontal axis is Longitude (°E) and vertical axis is Latitude (°S).

creation and propagation in the Southern Ocean. The typical magnitude of the RMS variability is 0.4°C for regions of high variability in the Southern Ocean.

To determine which timescales are dominant, I used a Fourier bandpass filter to calculate the energy within individual period bands (1-3, 3-8, 8-16, 16-32

Band Pass Filter (years)	> 1	1 - 3	3 - 8	8 - 16	16 - 32
12.5 m	> 0.1	> 0.04	> 0.06	> 0.05	> 0.05
410 m	> 0.03	> 0.007	> 0.02	> 0.02	> 0.02
1130 m	> 0.008	> 0.002	> 0.002	> 0.004	> 0.004

Table 4.2: Annually averaged salinity RMS variability (psu) peaks at various depths and bandpass filters.

and 32-64 years). For period bands 1-3 to 8-16 years, the resulting spatial distribution of variability (not shown) is similar to that seen in Figure 4.1 with magnitudes of 0.2 and 0.25°C (see Table 4.1). At larger period (16-32 and 32-64 years) the areas of high variance become more confined to more localised regions (Figure 4.2) and magnitudes are slightly less at around 0.15°C.

The highest RMS variability occurred in the 3-8 year band (see Table 4.1). Such time scales include signals typically associated with the ACW (4-5 year cycles). Since the resultant spatial distribution of variability is similar to Figure 4.1 and consists of mostly circumpolar energy, we note that the model shows circumpolar variability in on ACW timescales.

These results suggest that there is one dominant mode occurring: A mode of variability which occurs in the Southern Ocean primarily along the ACC. This mode of variability operates on timescales between 1 and 8 years and showed its highest energy in the 3-8 year period band (where the Antarctic Circumpolar Wave was found (White and Peterson, 1996)).

Depth surface 410 metres

At 410 m, the RMS variability of annually averaged temperature anomalies shows a pattern of strong circumpolar variability (Figure 4.3). There is high variability over the entire ACC apart from a small region around the Drake Passage. There is also high energy on the south east and west coasts of Australia. The magnitude of RMS variability is around 0.2°C.

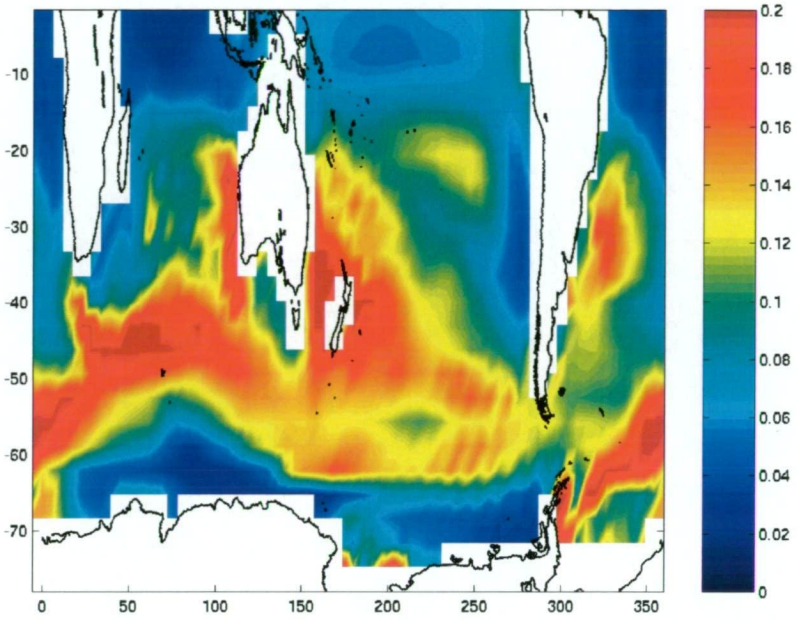

Figure 4.3: RMS variability of annually averaged potential temperature (°C) at 410 m depth level using control model years 1880-2179. Horizontal axis is Longitude (°E) and vertical axis is Latitude (°S).

By filtering in various period bands, variability about the Australian coast shows a weak presence in period bands 1-3 and 3-8 years (see Figure 4.4 for 3-8 year band). At these periods the circumpolar variability is clearly the dominant feature with magnitudes of around 0.07 to 0.15°C (see Table 4.1). Also, variability on these timescales which is circumpolar is similar to observed ACW variability. As the period increases (Figure 4.5), the Australian coastal variability becomes a dominant feature. Also, there is also relatively high variability throughout the ACC, particularly in and around the Atlantic and west Pacific sectors. Magnitudes on these timescales are around 0.1°C. Regions near Antarctica show high energy, including the Ross and Weddell Sea. Here, surface water sinks and becomes Antarctic Bottom

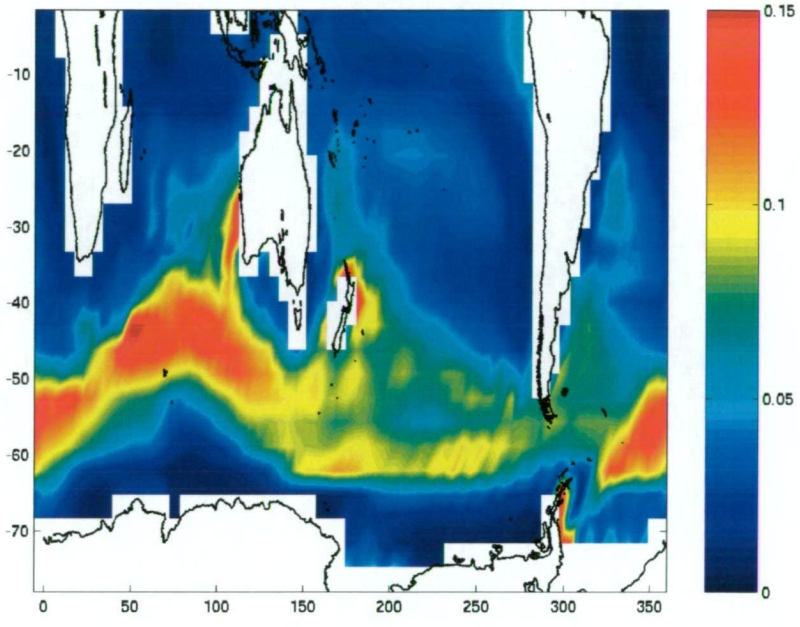

Figure 4.4: Filtered RMS variability (3-8 years) of annually averaged potential temperature (°C) at 410 m depth level using control model years 1880-2179. Horizontal axis is Longitude (°E) and vertical axis is Latitude (°S).

Water (Hanawa and Talley, 2001).

Looking at the 1130 m depth level (Figure 4.6), high variability occurs in the Southern Ocean around Australia and New Zealand as well as in the Ross and Weddell seas. These regions show magnitudes of around 0.06°C. Using filters, the spatial pictures (not shown) are very similar for all frequencies, although the longer period bands contain the most energy (Table 4.1) and are most similar to the spatial map of total variability (Figure 4.6). Dominance of the long periods reflects how the ocean filters short term variability signals with depth. In terms of relative energy, the 3-8 year period band showed the highest relative energy with peaks occurring along the ACC with magnitudes

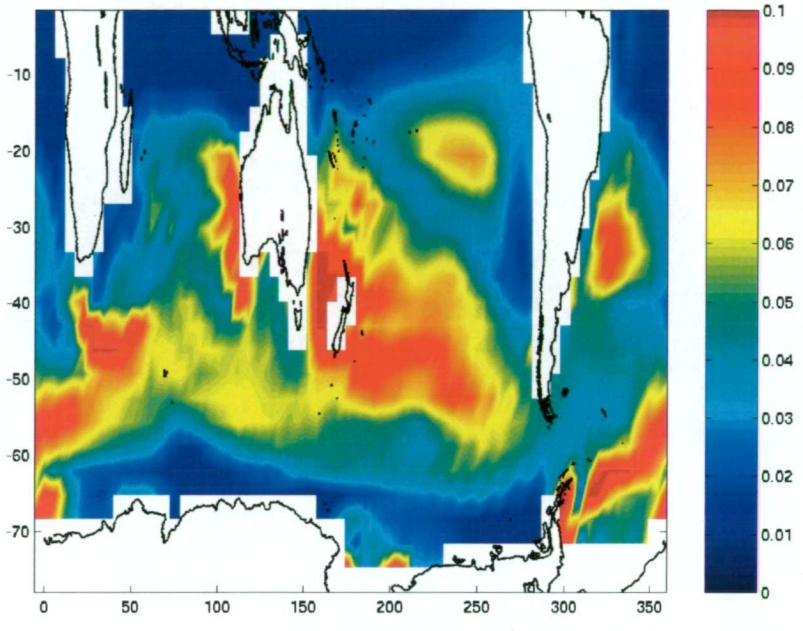

Figure 4.5: Filtered RMS variability (16-32 years) of annually averaged potential temperature (°C) at 410 m depth level using control model years 1880-2179. Horizontal axis is Longitude (°E) and vertical axis is Latitude (°S).

of around 0.15°C (see Table 4.1).

These results suggests there are at least two modes of temperature variability at 410 m: (1) On short period bands (1-10 years) there is high energy seen throughout most of the ACC. The highest energy band (3-8 years) includes that of the observed ACW, (2) Using longer periods bands (¿ 16 years), the highest energy occurs in the ACC flow, as well as off the south east and west Australian coast and in regions near Antarctica. According to previous study, regions at depth which do exhibit higher variance are either dynamically closer to the surface source regions or are undergoing internal dynamic processes such as Rossby waves rather than thermodynamic processes related

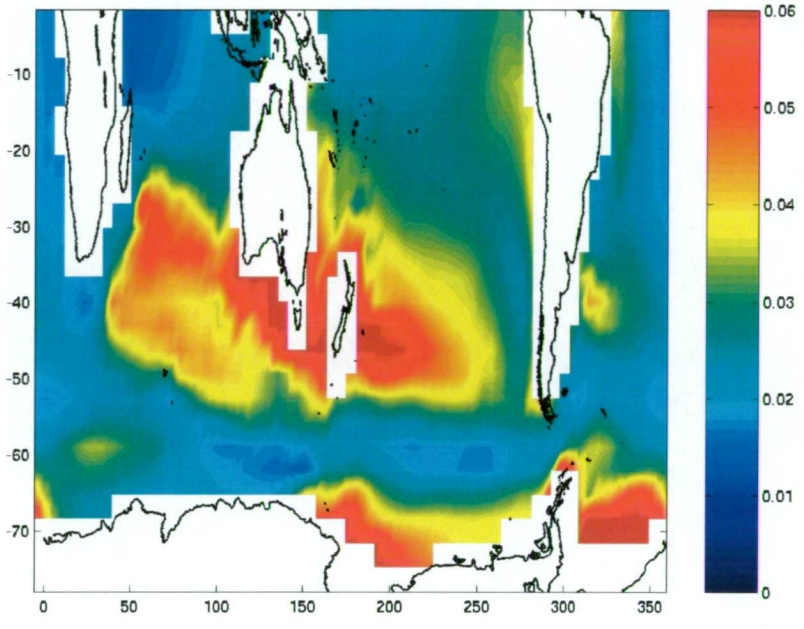

Figure 4.6: RMS variability of annually averaged potential temperature (°C) at 1130 m depth level using control model years 1880-2179. Horizontal axis is Longitude (°E) and vertical axis is Latitude (°S).

to water mass formation.

Salinity at depth 12.5 metres

RMS variability of salinity at 12.5 m (Figure 4.7) shows high energy about the coast of Antarctica as well as a band of high variability (hereafter Atlantic variability band) beginning at the Antarctic coast and extend north into the ACC. The Atlantic variability band begins in the Ross sea, continues east through Drake passage, continues northeast through the Atlantic Ocean and terminates southwest of Australia around 40°S, 100°E. The Indian Sector of the Southern Ocean shows relatively low salinity variability against Antarctica. Overall, the regions of high variability show RMS magnitudes

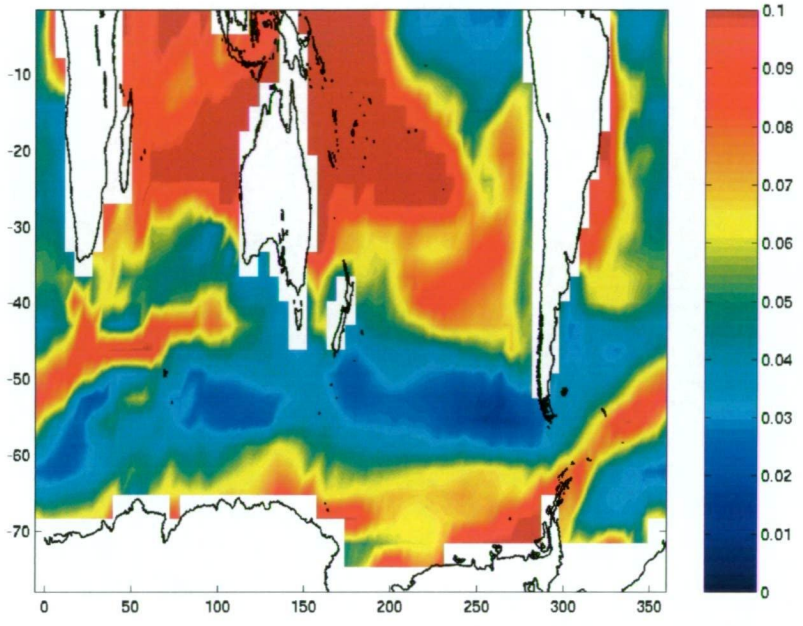

Figure 4.7: RMS variability of annually averaged salinity (psu) at 12.5 m depth level using control model years 1880-2179. Horizontal axis is Longitude (°E) and vertical axis is Latitude (°S).

$>$ 0.1 psu. Using the bandpass filters, the Atlantic variability band is seen clearly in short periods (1-8 years) (Figures not shown). The 3-8 year filter shows the highest energy peaks (see Table 4.1) and the Atlantic variability band shows a strong presence. The spatial picture of variability using the 3-8 year filter is similar to Figure 4.7 except that there is low variability off the Antarctic coast (except between 240 and 360°E where there is moderate energy). Using longer periods (8-32 years) the Atlantic variability band has less relative energy (8-32 years) (see Figure 4.8 for 16-32 year cycles). At these timescales the highest variability occurs as peaks around the Antarctic coastline (Figure 4.8) particularly in the Ross Sea. This is likely due to long term fluctuation in sea ice and Antarctic Bottom water formation. Salinity

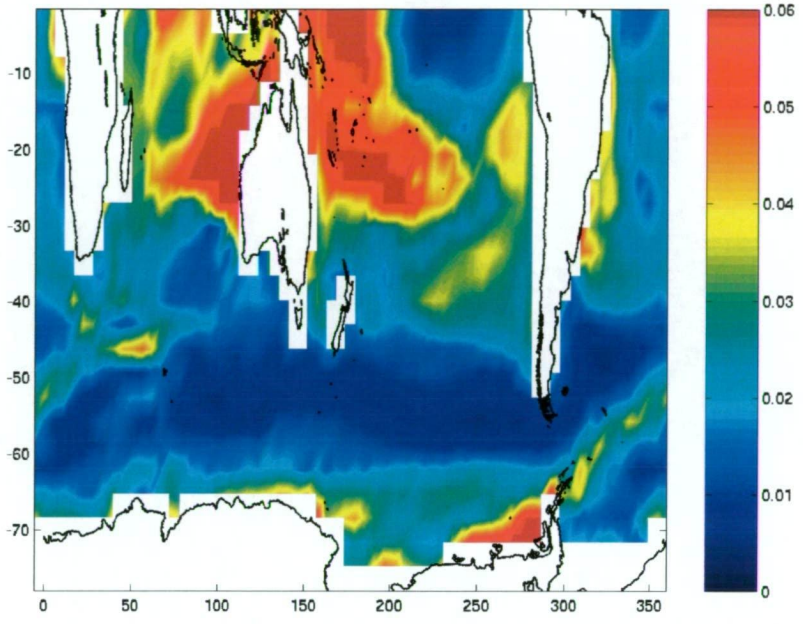

Figure 4.8: Filtered RMS variability (16-32 years) of annually averaged salinity (psu) at 12.5 m depth level using control model years 1880-2179. Horizontal axis is Longitude (°E) and vertical axis is Latitude (°S).

variability at 12.5 m reveals the following: (1) At high period there is high energy in the Atlantic variability band. This area of variability does not geographically overlap the circumpolar band of high temperature variability, at this depth level. (2) Using longer periods there is high energy along the coastline of Antarctica, most likely reflecting the variability in sea ice and water mass formation.

Salinity at depth 410 metres

At 410 m, there is high salinity variability around Australia and some areas of Antarctica (Figure not shown) with magnitudes greater than 0.02 psu. Using the band pass filters, the spatial variability is similar to the total variability

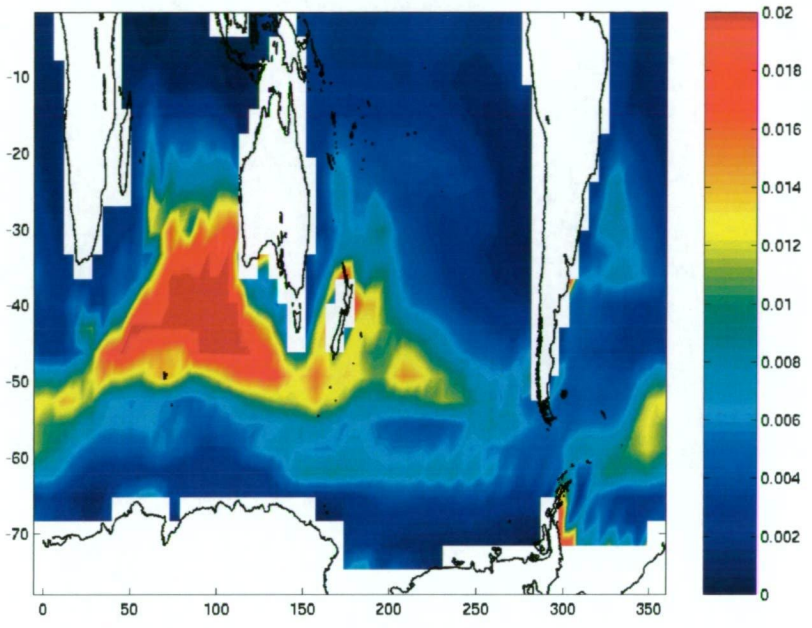

Figure 4.9: Filtered RMS variability (3-8 years) of annually averaged salinity (psu) at 410 m depth level using control model years 1880-2179. Horizontal axis is Longitude (°E) and vertical axis is Latitude (°S).

except that there is more energy in the ACC region in the higher frequencies (see Figures 4.9 and 4.10 for comparison). The 3-8 year band shows the highest energy peaks within the Southern Ocean (see Table 4.1 and Figure 4.9). Longer periods (cycles > 8 years) (Figure 4.10) also have high energy peaks, however these are located further north of the ACC as well as adjacent to the Australian coast. This result is qualitatively similar to temperature variability at 410 m. This indicates that temperature and salinity at 410 m have similar causes for variability unlike the 12.5 m depth level, discussed earlier.

Deeper, at 1130 m, variability in salinity is circumpolar and coincides clearly with the ACC (Figure 4.11). Two variability peaks clearly occur. These

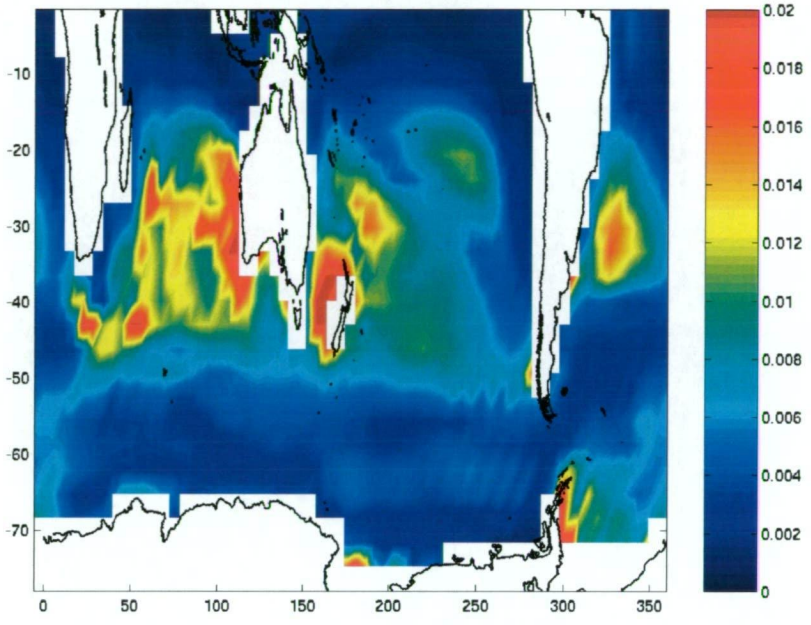

Figure 4.10: Filtered RMS variability (16-32 years) of annually averaged salinity (psu) at 410 m depth level using control model years 1880-2179. Horizontal axis is Longitude (°E) and vertical axis is Latitude (°S).

are in the Pacific and Indian Ocean sectors. The magnitudes of variability peaks are greater than .008 psu. All filtered bands show the circumpolar distribution of variability (Figures not shown). The lower frequencies also show the Pacific and Indian Ocean sectors energy peaks and contain more energy overall (see Table 4.2). This result is very interesting as it is in complete contrast with temperature variability which showed little energy directly in the ACC. This result may reflect seasonal formation or movement of AAIW which is typically identified by a salinity minimum at around 1000 m.

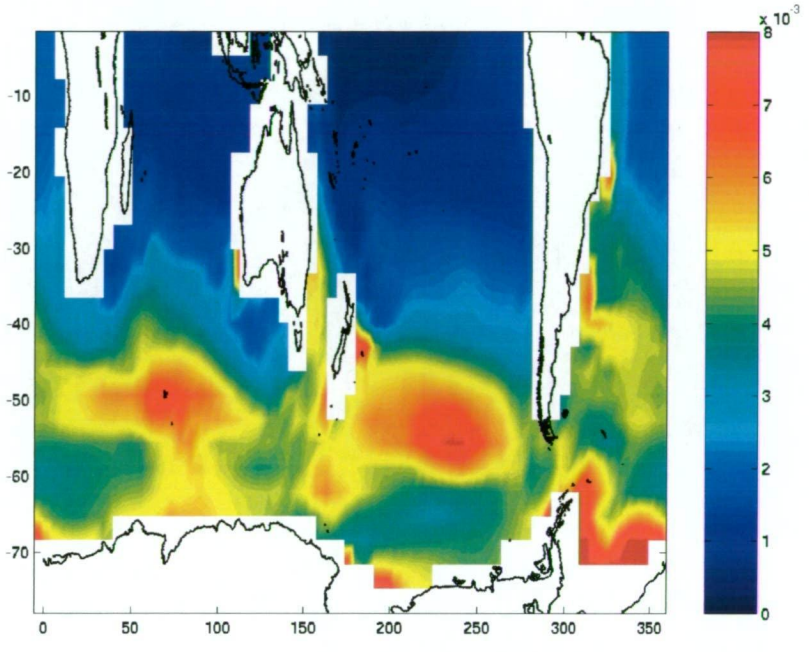

Figure 4.11: RMS variability of annually averaged salinity (psu) at 1130 m depth level using control model years 1880-2179. Horizontal axis is Longitude (°E) and vertical axis is Latitude (°S).

Summary

In Section 4.1 I have examined the RMS variability of temperature, salinity, heat flux, zonal and meridional winds. Temperature variability at 12.5 m shows two dominant features: (1) A circumpolar band of variability, centred at 60°S, with high energy within 3-8 year period and similar to ACW; and (2) At longer periods, (> 16 year cycles) high variability occurs in regions where certain water masses form, including AABW. The former generally correlates well with annually averaged heat flux variability. Deeper, at 410 m, the variability is centered over the ACC flow. At the lower frequencies it tends to be more spread northward, perhaps representative of slower currents (part of the ACC system) that flow up the Australian west and east coast.

Deeper still at 1130 m there is less variability in the strong ACC flow. The high variability is now found in lower frequencies, indicating that the ocean has filtered much of the high period signal.

High salinity variability occurs near the surface as a narrow circumpolar band over part of the Southern Ocean (labeled the Atlantic variability band). Much of the variance occurred at high period. Low period energy occurred around Antarctica. At 410 m the salinity variability mirrored the temperature variability, occurring mainly in the ACC. At 1130 m, unlike temperature variability, the salinity variability is high over the ACC flow in the Southern Ocean. As previously mentioned, heat flux variability has a similar spatial picture to temperature variability (12.5 m) with high variability at most longitudes at 60°S. Wind stress variability (zonal and meridional) is high throughout the Southern Ocean, particularly in the Pacific Sector.

4.2 Variability on neutral density surfaces

In the following two sections I examine the spatial structure of RMS variability on neutral surfaces (section 4.1) and the spatial and temporal evolution of dominant modes (section 4.2) on neutral surfaces. The properties that I examine are temperature and pressure. As discussed in Chapter 2, salinity on a neutral surface correlates directly to temperature and so does not need to be analysed. Warm (cool) anomalies correspond to saltier (fresher) anomalies. The surfaces that we analyse in this chapter include surfaces in the range of 26 to 27.5 which include SAMW and AAIW.

RMS variability of annually averaged temperature and pressure on neutral surfaces.

In this section I examine the spatial structure of RMS variability for various neutral density surfaces. Neutral density surfaces used here are 26, 26.5 and 27 $kg.m^{-3}$ (Figures 4.12 to 4.17). The mean properties on these surfaces were discussed in chapter 2.

On neutral density surface 26 $kg.m^{-3}$ (Figure 4.12), RMS variability of potential temperature is generally high where the neutral density surface outcrops and is directly ventilated. Also, there is high variability in both corners of the Pacific Ocean, the southeast corner of the Indian Ocean and also through most of the Atlantic. These regions are subject to or are close to regions of seasonal outcropping (and direct ventilation). RMS variability of potential temperature has magnitudes of around 0.2°C.

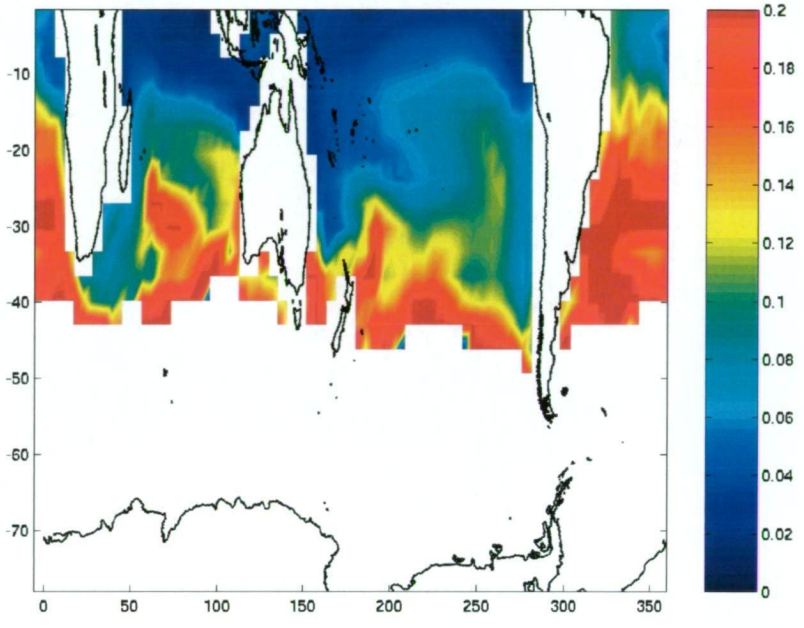

Figure 4.12: RMS variability of annually averaged potential temperature (°C) on neutral density surface $\gamma = 26.0$ kg.m^{-3} using 300 years of c17 control model output.

Variability of pressure on 26 kg.m^{-3} (Figure 4.13) shows regions of high RMS variability with magnitude of about 20 metres. Generally, large variability occurs along and near the outcrop line (similar to the map of potential temperature variability). The numerical calculation of RMS variability uses only points where the surface exists, such that there are some regions on the outcrop line that have low variability (eg. 35°S, 180°E). This is due to a low number of sample points and should be ignored. On the western side of each ocean there is low variability in pressure. This occurs because the surface is relatively deep here due to the presence of the subtropical gyre. High variability also occurs north of 20°S along the east coast of South America due to Kelvin wave generation. This is not associated with high variability

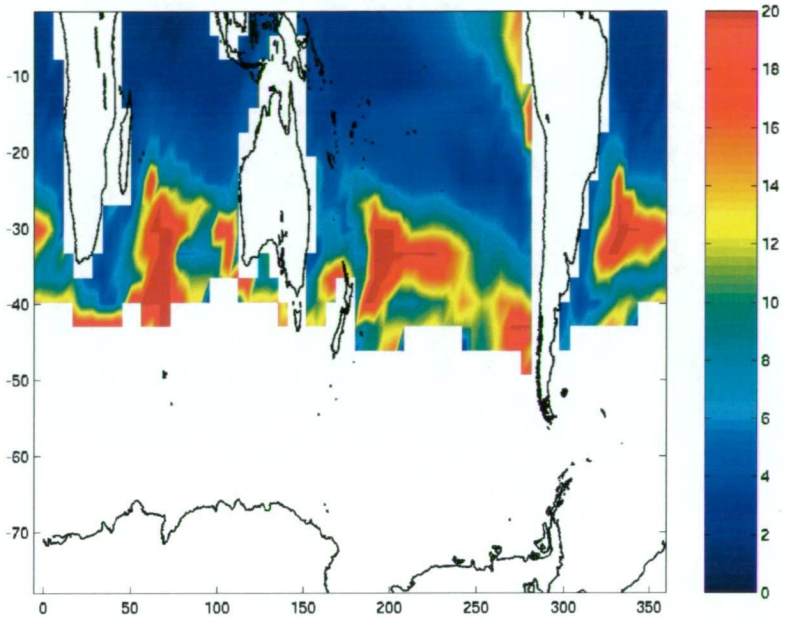

Figure 4.13: RMS variability of annually averaged pressure (dbar) on neutral density surface $\gamma = 26.0$ kg.m^{-3} using 300 years of c17 control model output.

in temperature on the neutral density surface (as occurred for other regions of high pressure variability). This is because the density surface does not outcrop. Outcropping of the surface leads to ventilation and temperature variability on the surface. Pressure variability in this area would impact on temperature on constant depths surfaces only. Note that temperature variability can also occur due to mixing along isopycnals. However, the amounts are much less significant then when compared to temperature variability due to ventilation.

On denser surface 26.5 kg.m^{-3} (Figure 4.14), the spatial structure of temperature variability is quite similar to that on 26 kg.m^{-3} except there is less variability in the Atlantic (at latitudes north of 30°) and southeast Pacific

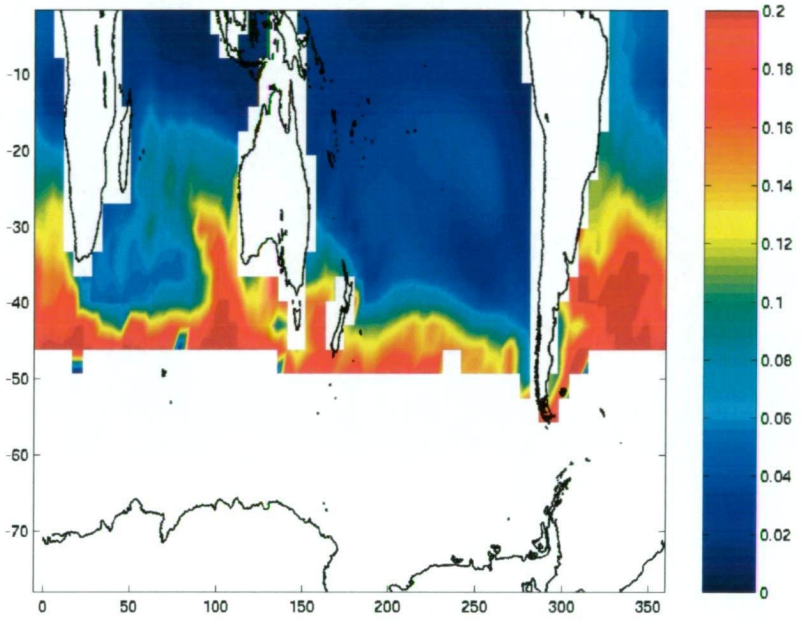

Figure 4.14: RMS variability of annually averaged potential temperature (°C) on neutral density surface $\gamma = 26.5$ kg.m^{-3} using 300 years of c17 control model output.

Ocean. Figure 2.11 in section 2.3 reveals that the outcrop regions adjacent to South America do not extend as far north (as occurred on 26), and therefore ventilation (and temperature variability) was reduced. The regions of high variability include the southeast Indian and the Atlantic Ocean (to 30°N). The mean pressure field (from 100 years of data) on this surface (Figure 2.11) shows that outcropping occurs in the Indian Ocean as far north as 30°N. Hence, it is safe to assume that much of the temperature variability in these regions arises as a result of being directly adjacent to the outcrop, where ventilation occurs. The variability of pressure on this surface is similar in structure to the lighter surface, except that variability on 26.5 kg.m^{-3} extends less far north.

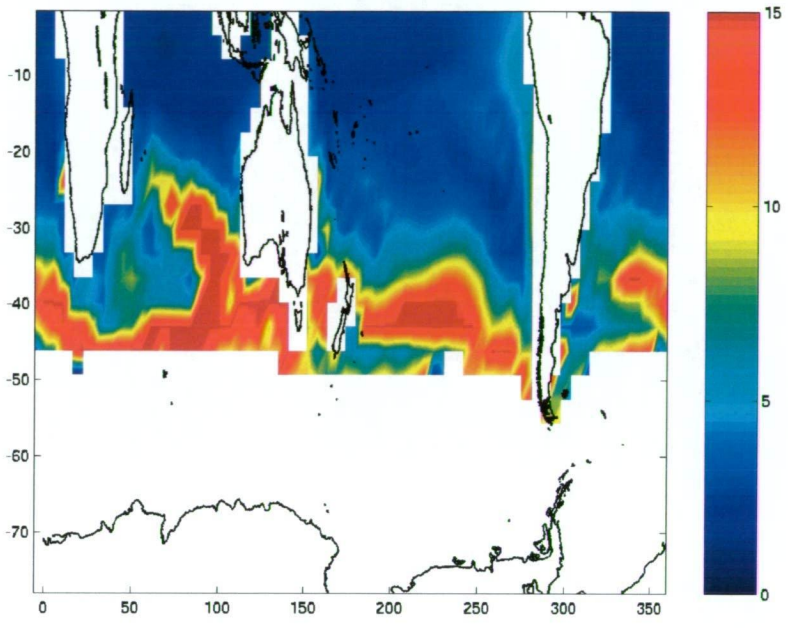

Figure 4.15: RMS variability of annually averaged pressure (dbar) on neutral density surface $\gamma = 26.5$ kg.m^{-3} using 300 years of c17 control model output.

Deeper, at 27 kg.m^{-3} the spatial structure of temperature and pressure variability (Figures 4.16 and 4.17) changes somewhat to that of 26 and 26.5 kg.m^{-3}. The temperature variability is south of 45°S and high energy occurs almost exclusively along the Southern Ocean outcropping line. The magnitude of RMS variability is around 0.2°C. A feature of this map is the lack of high variaibilty in the Indian Ocean (subtropical gyre) and off the east coast of South America in the Atlantic Ocean. This highlights the difference in the neutral density surfaces 27 kg.m^{-3} as compared to 26 and 26.5 kg.m^{-3}. Neutral density surfaces 26 and 26.5 kg.m^{-3} outcrop in the northern part of the ACC whereas 27 kg.m^{-3} outcrops toward the southern part. The former undergo wintertime convection in the southeast Indian Ocean (to form SAMW)

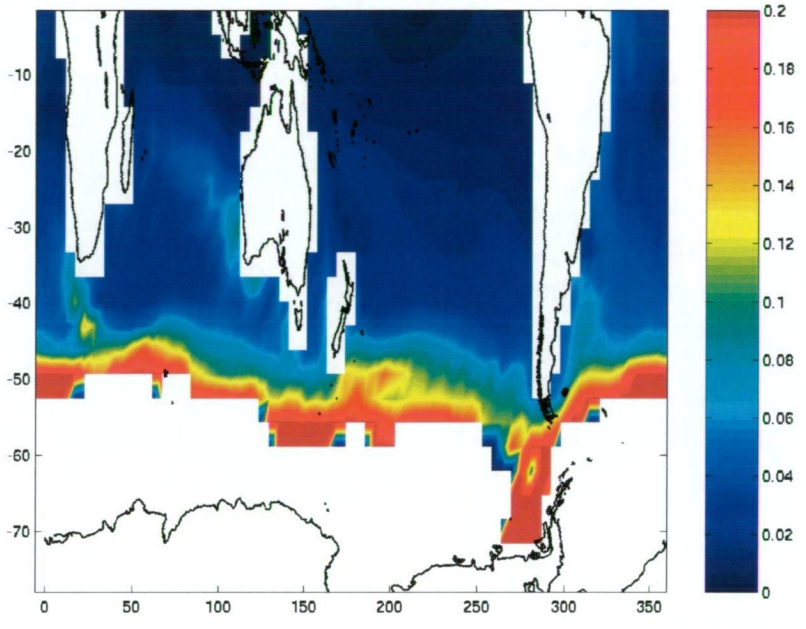

Figure 4.16: RMS variability of annually averaged potential temperature (°C) on neutral density surface $\gamma = 27.0$ kg.m^{-3} using 300 years of c17 control model output.

and outcrop further south in the summertime. The denser 27.5 kg.m^{-3} surface has a seasonal variation in outcropping latitude isn't as extreme. In fact in 100 winters it doesn't outcrop further north than 45°S in the Indian Ocean sector (see Figure 2.13) The spatial structure of pressure variability on 27 kg.m^{-3} shows that there is a general band of high variability at about 45 to 50°S which moves northward on the east coasts of New Zealand and South America. This occurs due to the surface being (on average) shallower in these regions and subject to seasonal outcropping.

The variability in pressure on neutral surfaces, arises due to vertical fluctuations of the the water column. Hence the large variability in the mid to southern corner of each ocean is likely due to the variation in strength of

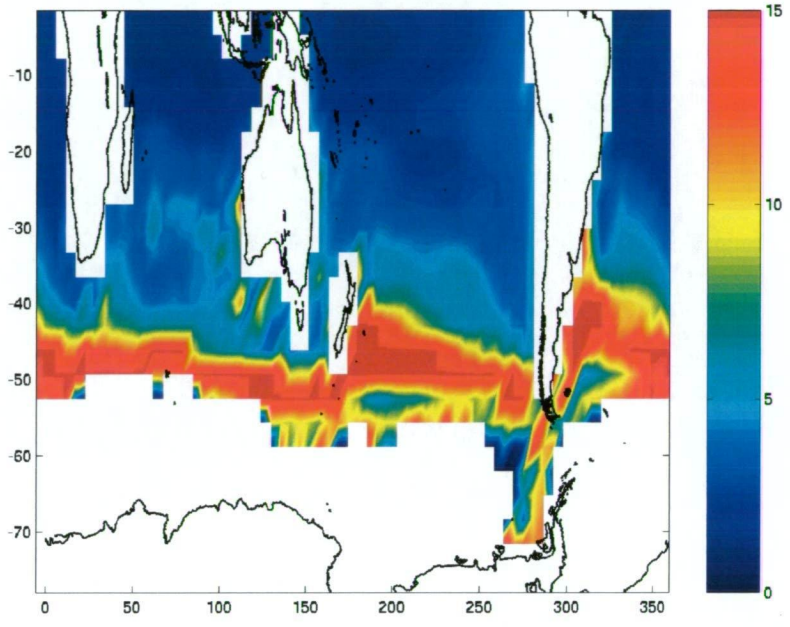

Figure 4.17: RMS variability of annually averaged pressure (dbar) on neutral density surface $\gamma = 27.0$ kg.m^{-3} using 300 years of c17 control model output.

seasonal convection levels which can lead to water mass formation. For example, on shallow surfaces (26.0 and 26.5) there is high pressure variability in SE Indian Ocean where SAMW typically forms. On the denser surfaces (27 and 27.5) there is less variability in the South East Indian Ocean but more in regions of AAIW formation such as in the South East Pacific Ocean.

Summary

In examining the variability of temperature and pressure on a neutral density surface alongside the mean pressure on that surface I have shown that high temperature variability is limited to regions near the outcropping of the surface. This prerequisite leads to ventilation and larger anomalies. For

example, on neutral density surface 26 $kg.m^{-3}$, there was large pressure variability near the equator on the west coast of America. Temperature variability did not occur here since the surface did not outcrop. On the other hand, regions which contained high variability in pressure, such as in the southeast Indian Ocean on neutral density 26.5 $kg.m^{-3}$, also showed high temperature variability. This occurred because the region was also subject to seasonal outcropping. The mean pressure on this surface (Figure 2.11 in Chapter 2.3) confirmed this. Generally the magnitude of RMS temperature variability seen on neutral density surface 26 to 27 $kg.m^{-3}$ was around 0.2°C. The magnitude of RMS pressure variability was around 20 m. These manitudes are much higher when directly adjacent to outcropping regions. Overall, variability on a neutral density surface is a cleaner signal than a signal on a depth surface which has a component of variability due to the vertical movement of the density surfaces.

4.3 HEOFs on depth surfaces

Here, I calculate Hilbert Empirical Orthogonal Functions (HEOFs) of various ocean and atmospheric properties. HEOFs are statistically significant modes which contain spatial and temporal evolution (see discussion in section 2). By calculating these modes I seek to further reveal the nature of variability in shallow waters. The properties I analyse are potential temperature at 12.5, 410 and 905 m, heat flux, salinity flux and meridional wind.

The spatial domain used in the analysis impacts on the resolution of spatial patterns to be detected. The grid area of all longitudes and latitudes between 20 and 80°S was chosen to represent the greater Southern Ocean. A summary of the variance attributable to each of the first 3 modes for each properties is summarised in Table 4.3.

Each HEOF contains a real and complex spatial map and a real and complex timeseries. The real and complex parts represent the evolving mode at 0° and 90°. To more easily comprehend the implication of the spatial maps, I show a series of spatial maps of reconstructed anomalies at various phases of the modes evolution. The phases are: 0°, 45°, 90°, 135° and 180°. The maps at 0° and 90° are, by definition, independant. The maps at 180° is, respectively the negative of the 0°. The time series maps are used to obtain the dominant frequency of the mode (by visual estimate or fourier analysis) and are generally not shown (see Figure 4.18 for example of real and imaginary timeseries).

In the following sections I describe the spatial and temporal characteristics

Variance Explained (%)	Mode 1	Mode 2	Mode 3
Potential Temperature (12.5 m)	13	7	6
Potential Temperature (410 m)	13	11	9
Potential Temperature (905 m)	18	12	11
Heat Flux	8	6	4
Salinity Flux	9	5	4
Meridional Wind Stress	14	11	6

Table 4.3: Variance in temperature, heat flux, salinity flux and meridional wind stress explained the first three modes of a HEOF analysis of a 300 year model run for all longitudes and latitudes between .

of up to the first three dominant modes.

HEOFs of potential temperature at 12.5 m

Figure 4.19 shows the spatial evolution of mode 1 HEOF throughout its spatial cycle. This mode contains 13% of variance and anomalies typically have magnitudes of around 0.2°C. The timeseries of this mode (Figure 4.18) shows that the average cycle of this mode is 6 years. Most of the spatial variance occurs in the Pacific Ocean. Its spatial struture consists of 3 distinct latitudional bands stretching almost across the Pacific Ocean: the first centred near the equator and of positive sign (at phase 0°), the second (of negative sign) centred at 20°S and oriented NW-SE, the third (of positive sign) occurs between 40 and 60°S with SW-NE orientation.

The band of anomalies at midlatitudes propagates eastward through the Pacific Ocean into the Atlantic Ocean and then to the Indian Ocean. In the Indian Ocean, anomalies move up the west coast of Australia toward Indonesia. Hence the mode involves circulation around the Southern Ocean as well as in the more tropical regions.

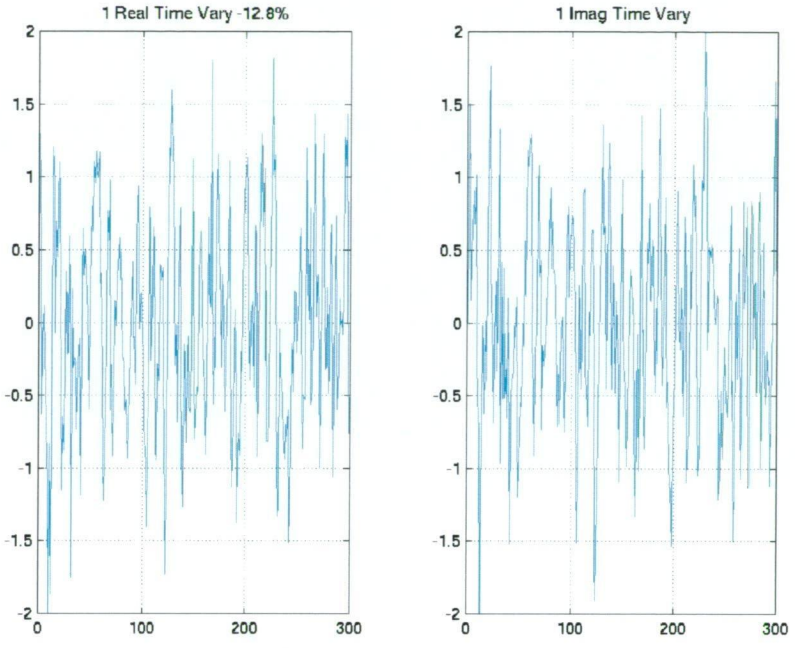

Figure 4.18: Real (left panel) and imaginary (right panel) components of the time evolution of Mode 1 of a HEOF of potential temperature at 12.5 m, showing the variation of magnitude of anomalies throughout the time series. Calculated using 300 years of the c17 control model run.

In the context of the anomalies travelling around Antarctica it is useful to define the zonal wavenumber of the anomaly. Here the spatial structure consists of a zonal wavenumber (number of cycles seen around the globe) of 2 to 3.

Mode 2 (Figure 4.20) contains around 7% of variance, timescales and magnitudes of anomalies are typically 5-6 years and 0.1°C respectively. Anomalies show propagation throughout much of the Southern Ocean with zonal wavenumber 3. High energy is seen in the east side of the Pacific Sector as well as through the Atlantic Ocean Sector of the Southern Ocean. In the Pacific Ocean there is high energy along (and to the north) 60°S between

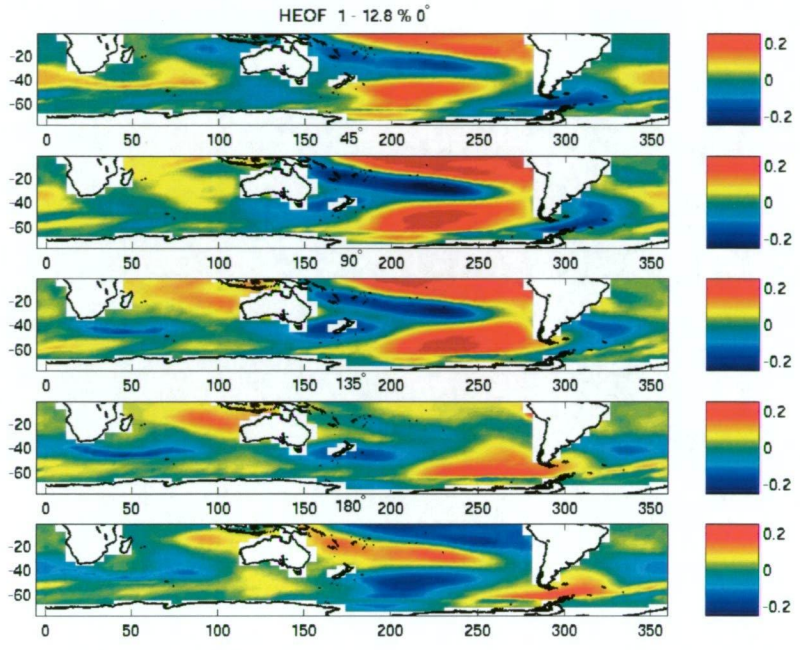

Figure 4.19: Spatial evolution of Mode 1 HEOF of potential temperature at 12.5 m calculated using 300 years of the c17 control model. The first panel shows the spatial state at the beginning (0°) of the cycle; the second panel shows the new spatial state after evolution through one eighth (45°) of a cycle; third, fourth and fifth panels show the spatial states at one quarter (90°), three eighths (135°) and one half (180°) of evolution of a cycle respectively.

180 and 300°E. This is consistent with results in section 3.1 which showed the highest RMS energy at 12.5 m to occur in this region, and further, with interannual timescales. In Figure 4.20, at the south east corner of the Pacific and Atlantic Oceans, anomalies travel north along the coast, similar to the flow which occurs in the real ocean.

Mode 3 (Figure 4.21) consists of 6% of the variance. The timescales of anomalies is around 6 years and magnitudes are typically 0.1°C. These anomalies show near perfect circumpolar propagation with zonal wavenubmer varying between 1 and 2.. Anomalies are strong throughout all latitudes south of the

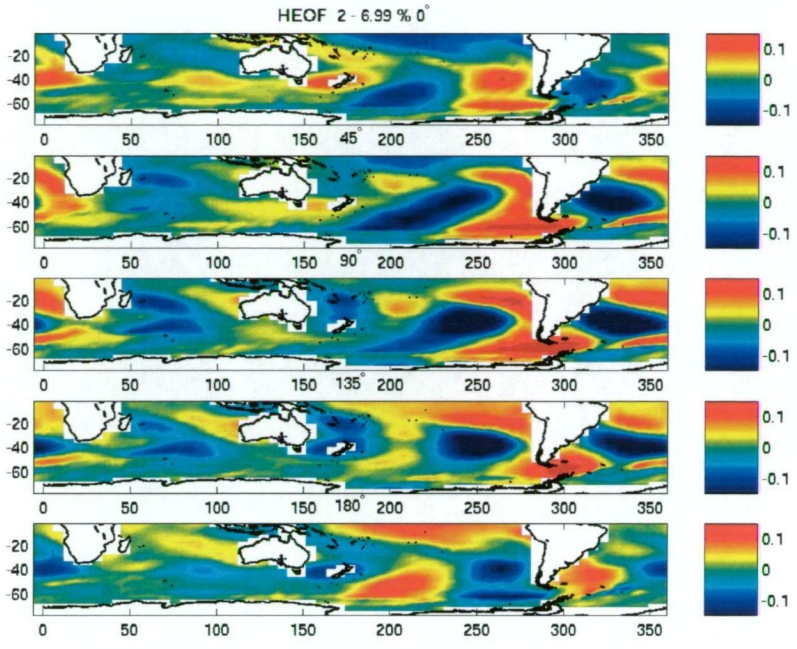

Figure 4.20: Spatial evolution of Mode 2 HEOF of potential temperature at 12.5 m calculated using 300 years of the c17 control model. The first panel shows the spatial state at the beginning (0°) of the cycle; the second panel shows the new spatial state after evolution through one eighth (45°) of a cycle; third, fourth and fifth panels show the spatial states at one quarter (90°), three eighths (135°) and one half (180°) of evolution of a cycle respectively.

equator and are most likely be linked to atmospheric forcing. Three features of this mode (interannual variability, circumpolar propagating anomalies and zonal wavenumber 2 structure) make it compare will with the observed ACW (timescales 4-5 years, circumpolar, propagating zonal wavenumber 2 anomalies). Hence the use of HEOFs has been able to detect a significant mode in line with observations, that simple RMS variability and Hovmoeller plots were unable to detect.

At 12.5 m, the first three modes are interannual cycles (timescales 6 to 7 years) which include anomalies which propagate around the ACC. These

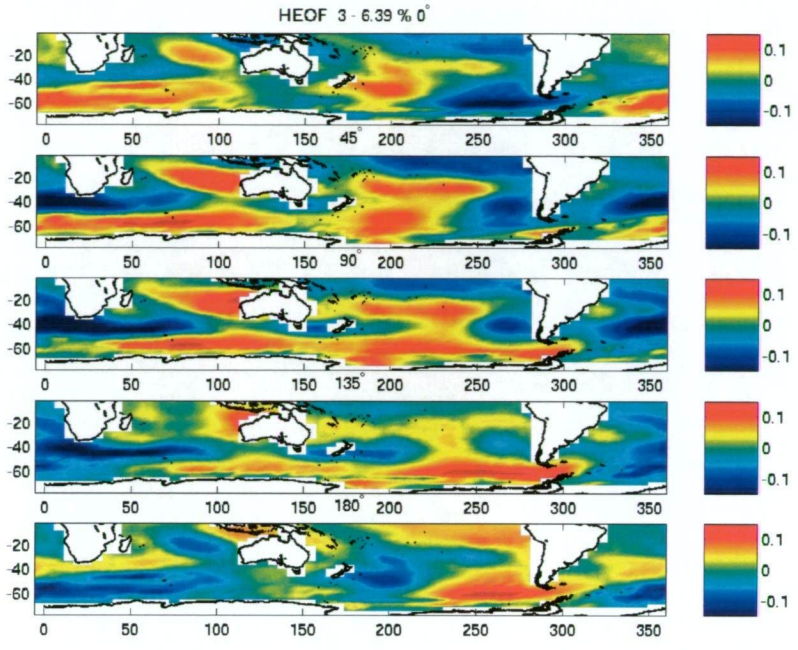

Figure 4.21: Spatial evolution of Mode 3 HEOF of potential temperature at 12.5 m calculated using 300 years of the c17 control model. The first panel shows the spatial state at the beginning (0°) of the cycle; the second panel shows the new spatial state after evolution through one eighth (45°) of a cycle; third, fourth and fifth panels show the spatial states at one quarter (90°), three eighths (135°) and one half (180°) of evolution of a cycle respectively.

results are consistent with results in section 3.1, which showed progating anomalies at the surface with high energy in the Pacific Ocean and on inter-annual time scales. Further, the use of the HEOFs have allowed us to detect new characteristics of variability at this depth. As well as showing spatial propagation around the ACC, the HEOFs show spatial propagation around the globe into and from the ocean basins. The separation of modes based on spatial and temporal dominance has identified a mode which is similar to the ACW in its temporal and spatial evolution.

HEOFs of potential temperature at 410 m

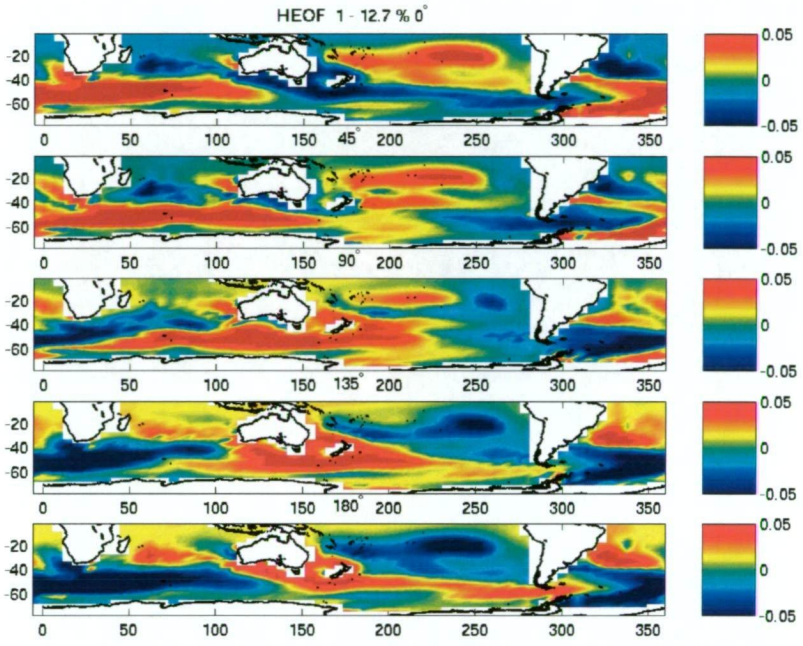

Figure 4.22: Spatial evolution of Mode 1 HEOF of potential temperature at 410 m calculated using 300 years of the c17 control model. The first panel shows the spatial state at the beginning (0°) of the cycle; the second panel shows the new spatial state after evolution through one eighth (45°) of a cycle; third, fourth and fifth panels show the spatial states at one quarter (90°), three eighths (135°) and one half (180°) of evolution of a cycle respectively.

At 410 m, mode 1 (Figure 4.22) contains anomalies which are dominated by cycle lengths of around 10 years. The magnitude of anomalies is approximately 0.05°C. Circumpolar navigation of anomalies is clearly apparent: At 0° positive (negative) anomalies occur throughout the ACC in the Atlantic and Indian Oceans and negative anomalies occur throughout the Pacific Ocean. Hence, the zonal wavenumber of anomalies is approximately 1. Anomalies are the same strength throughout the ACC except in the south-east Pacific where they are slightly weaker.

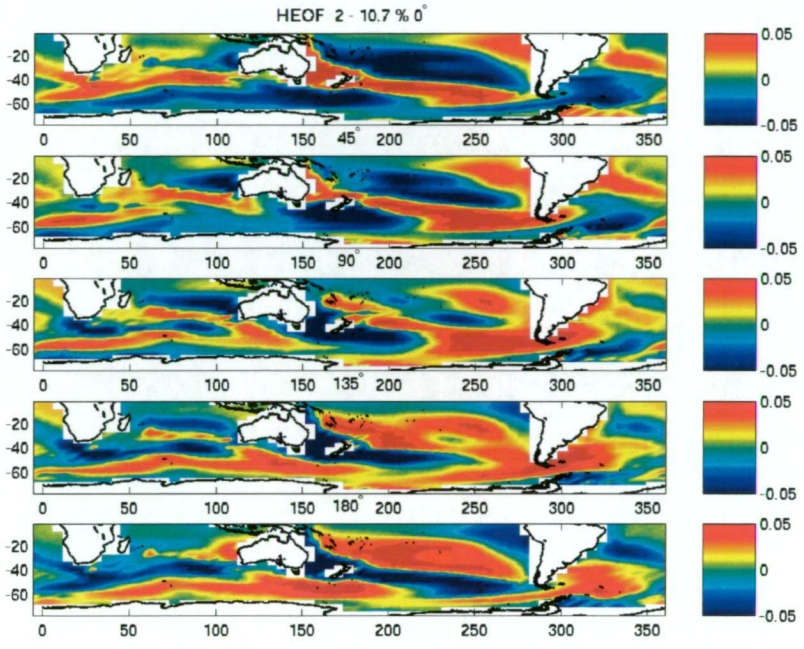

Figure 4.23: Spatial evolution of Mode 2 HEOF of potential temperature at 410 m calculated using 300 years of the c17 control model. The first panel shows the spatial state at the beginning (0°) of the cycle; the second panel shows the new spatial state after evolution through one eighth (45°) of a cycle; third, fourth and fifth panels show the spatial states at one quarter (90°), three eighths (135°) and one half (180°) of evolution of a cycle respectively.

These results compare well with previous results showing high RMS energy in the ACC at this depth. The HEOF have revealed the zonal structure of the anomalies to be wavenumber 1 and that the frequency is on average slower (around 10 years) compared with the average frequency at 12.5 m (around 6 years). This mode also shows high energy about Australia, which is consistent with the high RMS variability around Australia at this depth (as discussed in section 3.1).

Mode 2 (Figure 4.23) contains 11% of variance and timescales are typically 9-10 years. Here, mode 2 shows propagating anomalies around the ACC

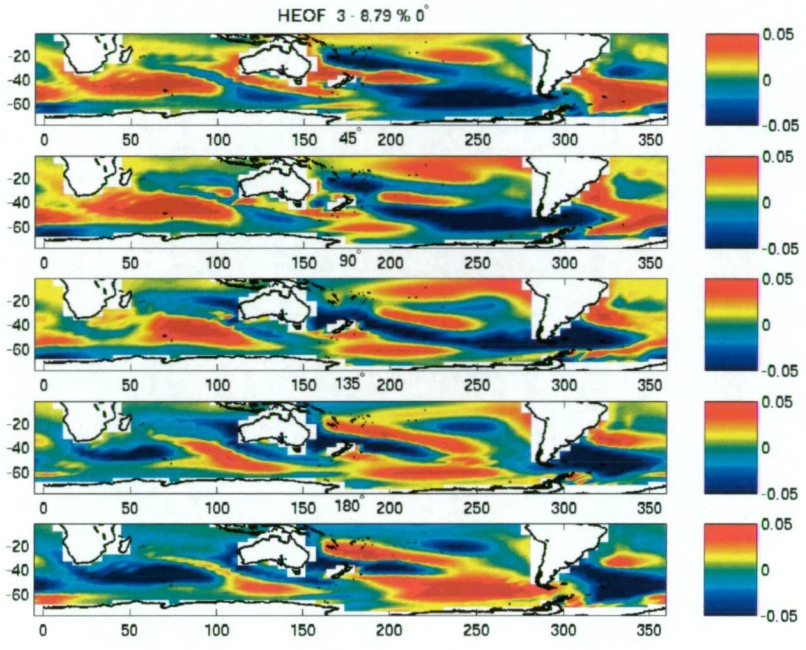

Figure 4.24: Spatial evolution of Mode 3 HEOF of potential temperature at 410 m calculated using 300 years of the c17 control model. The first panel shows the spatial state at the beginning (0°) of the cycle; the second panel shows the new spatial state after evolution through one eighth (45°) of a cycle; third, fourth and fifth panels show the spatial states at one quarter (90°), three eighths (135°) and one half (180°) of evolution of a cycle respectively.

with spatial zonal wavenumber 2 and magnitudes of approximately 0.05°C.. Variance is high over all longitudes. Anomalies also propagate from the ACC into the individual oceans. In the Indian and Pacific Ocean this occurs at their south east corner. Anomalies enter the Atlantic basin as a result of anomalies propagating through Drake Passage east and northward. The zonal wavenumber structure and circumpolar propagation contained in this mode is similar to that of the observed ACW. The period is longer (9-10 years) than the observed signal (4-5 years) however, as Sections 3.1 - 3.3 found, anomalies have incresing longer periods with increasing depth.

Mode 3 (Figure 4.24) contains 9% of variance and has periods of mainly around 7 years and magnitudes of 0.05°C (similar to modes 1 and 2 at 410 m). Here circumpolar propagation is occurring and it appears that anomalies arise in the Pacific Ocean off the coast of Australia. High energy is seen in the Pacific Ocean. The anomalies show a dominante zonal wavenumber of 3. This structure was seen clearly in Hovmoeller diagrams of potential temperature at 410 m. Hence, the use of HEOF analysis has revealed the spatial evolution of this ACW-like variability.

Hence at 410 m, we see the first three modes all contain anomalies which propagate around the globe. The strongest mode shows zonal wavenumber 1 structure and frequencies of 10 years; the second mode show zonal wavenumber 2 structure with frequencies of 9-10 years also; and the third mode shows zonal wavenumber 3 structure with frequencies of around 7 years. So the increasing modes generally have increasing wavenumber and shorter periods.

HEOFs of potential temperature at 905 m

At 910 m (Figure 4.25), mode 1 contains 18% of variance. The cycles show two peaks in frequency: one of around 15 years and the second on 100 years. Hence, at these intermediate depths multi-decadal signals are increasingly dominating the variability in the model run. The spatial structure of mode 1 consists of a dominant N-S pattern with very little propagation in the E-W direction. This is a stationary wave rather than a propagating wave. The NS component is similar to that of zonal wind stress anomaly (discussed later in this chapter).

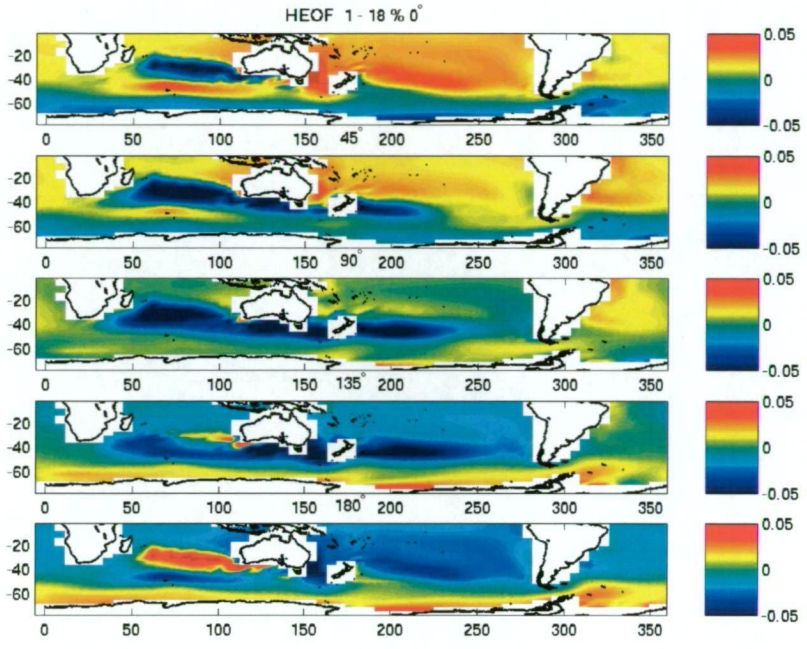

Figure 4.25: Spatial evolution of Mode 1 HEOF of potential temperature at 905 m calculated using 300 years of the c17 control model. The first panel shows the spatial state at the beginning (0°) of the cycle; the second panel shows the new spatial state after evolution through one eighth (45°) of a cycle; third, fourth and fifth panels show the spatial states at one quarter (90°), three eighths (135°) and one half (180°) of evolution of a cycle respectively.

Mode 2 (not shown) operates on around 12.5 years and is very similar in spatial structure and evolution to mode 1. High energy occurs in the Indian and Pacific Oceans (around Australia) where anomalies evolve and dissolve between the Indian and Pacific. Circumpolar Propagation does not occur and there is little energy in the East Pacific and Atlantic Oceans. The mode is also stationary rather than propagating and hence is likely to be the stationary counterpart of mode 1. Therefore, mode 1 and 2 represent a stationary wave which consists of oscillating anomalies predominantly in the Indian and southwest Pacific Ocean. The HEOF analysis seeks to maximise propagation

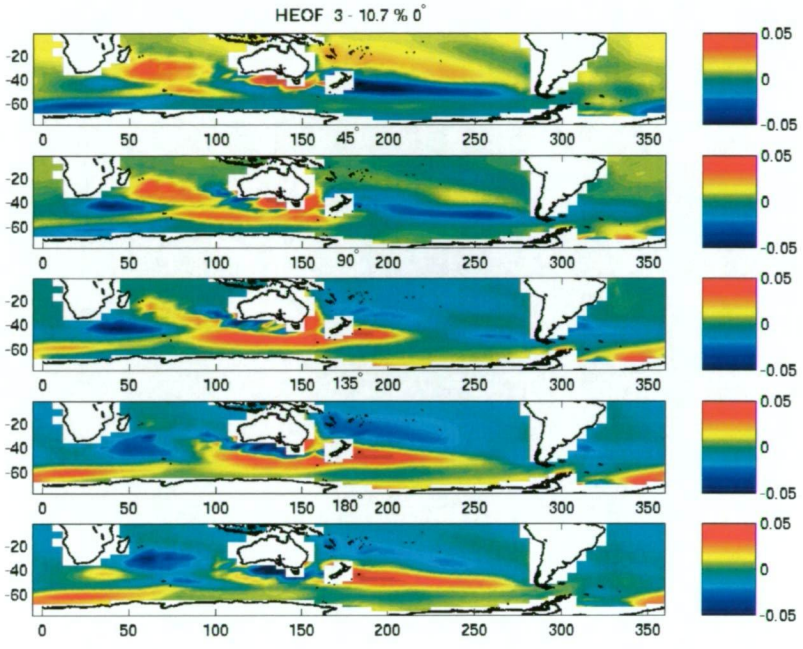

Figure 4.26: Spatial evolution of Mode 3 HEOF of potential temperature at 905 m calculated using 300 years of the c17 control model. The first panel shows the spatial state at the beginning (0°) of the cycle; the second panel shows the new spatial state after evolution through one eighth (45°) of a cycle; third, fourth and fifth panels show the spatial states at one quarter (90°), three eighths (135°) and one half (180°) of evolution of a cycle respectively.

and so that true stationary waves are revealed in HEOF analysis as two modes with contrary propagation.

Mode 3 (Figure 4.26) contains 11% of variance and cycles of approximately 15 years. Energy is dominant in the Indian Ocean and around Australia (ie. includes the far west Pacific Ocean) and occurs throughout much of the ACC, with the exception of around Drake Passage, where it is weak. There is easterly propagation occurring here and anomalies can be detected moving from the Atlantic Ocean through to the east Pacific Ocean. The zonal structure is dominated by wavenumber 2.

So at this depth level, HEOF modes are fairly well dominated by the Indian and west Pacific Ocean (around Australia) regions stationary mode 1 and 2. This is indicative of the deep mixed layer in this region which allows fast access for anomalies to reach depth. Circumpolar propagation is visible in mode 3 (mode 2) and all 3 modes were saturated by 12 to 15 year cycles.

Summary of potential temperature HEOFs

Timescales of HEOFs were 6 to 7 years at 12.5 m, 7 to 10 years at 410 m and 12 to 15 years at 905 m. Hence, as expected, timescales increased with depth.. The zonal structure of anomalies occurred as wavenumbers 1 to 3 at 12.5 m and 410 m, with dominance of wavenumber 3 at 12.5 m change to wavenumber 1 and 2 at 410 m. Zonal wavenumber 2 was detected at 905 m. Hence there is also a trend of increasing depth leading to a gradual decline of the dominant zonal wavenumber 3 structure to zonal wavenumber 2 stucture.

4.4 HEOFs of properties on neutral density surfaces

In this section I examine the spatial and temporal variability of potential temperature on neutral density surfaces by calculating HEOFs. The surfaces I examine here are 26.5, 27 and 27.5 kg.m^{-3}. The HEOF analysis discards grid points (longitude, latitude) where the neutral density surface has outcropped (at any point in time in the data set). Hence, the analysis is somewhat limited as the domain excludes much of the southern location of each surface. In particular, surfaces upon which SAMW formation occurs show a wide range of latitudes of outcropping areas (see section 2.3), therefore will be affected considerably. The variance explained by each mode is listed in Table 4.4.

HEOF of potential temperature on neutral density surface 26.5 kg.m^{-3}

On 26.5 kg.m^{-3} the first 4 modes contain over 70% of the total variance and are distributed as follows 34%, 20%, 10% and 7% for modes 1 to 4 respectively (Table 4.4). The magnitude of anomalies is typically 0.05°C. Modes 1 to 3 are low frequency, with timescales of around 15 to 20 years (Figure 4.27). Mode 4 (not shown) is the most dominant mode with a higher frequency (6 to 10 years).

Mode 1 (Figure 4.28) contains high variability (anomalies greater than 0.05°C)

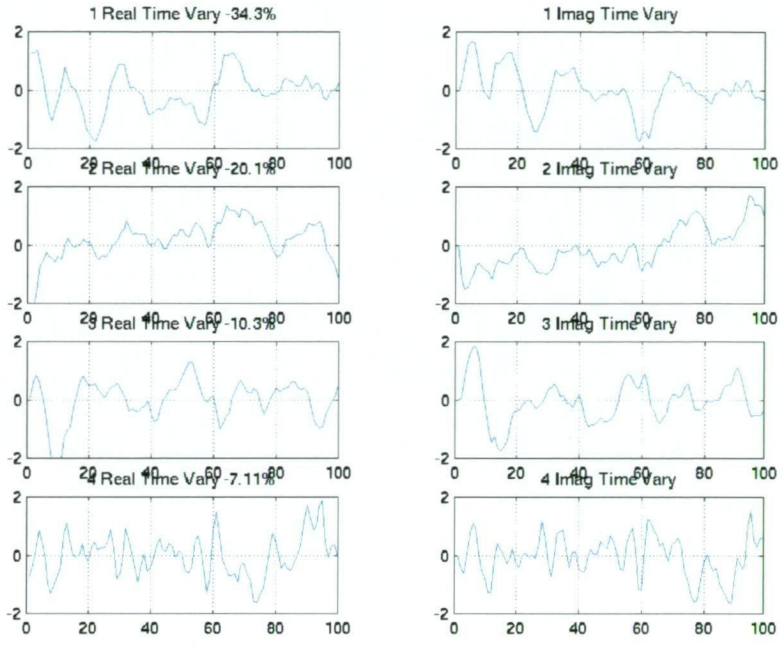

Figure 4.27: Real (upper left panel) and imaginary (upper right panel) components of the time evolution of Mode 1 of a HEOF of potential temperature on neutral density surface $\gamma = 26.5$ kg.m^{-3}, showing the variation of magnitude of anomalies throughout the time series. Second, third and bottom levels show equivalent Figures for modes 2 to 4. Calculated using 300 years of the c17 control model run.

in the Indian and Atlantic Oceans. The time varying component of this mode is on decadal timescales, with cycles averaging about 15-20 years (Figure 4.27 (a)). In the Indian Ocean, there is high variability occurring in the southeast. As the mode evolves, this extends west (south of 20°S) to the coast and then south. Here it either moves west around the African coast or meets similar sign anomalies from the west. In the Atlantic there is high variability of positive (negative) sign throughout most of the ocean to latitude 20°S. As the mode evolves an anomaly of opposite sign is generated from the south and gradually rise north. South of Australia appears to be a source of anomalies which then feed the southeast Indian Ocean and Pacific Ocean. About

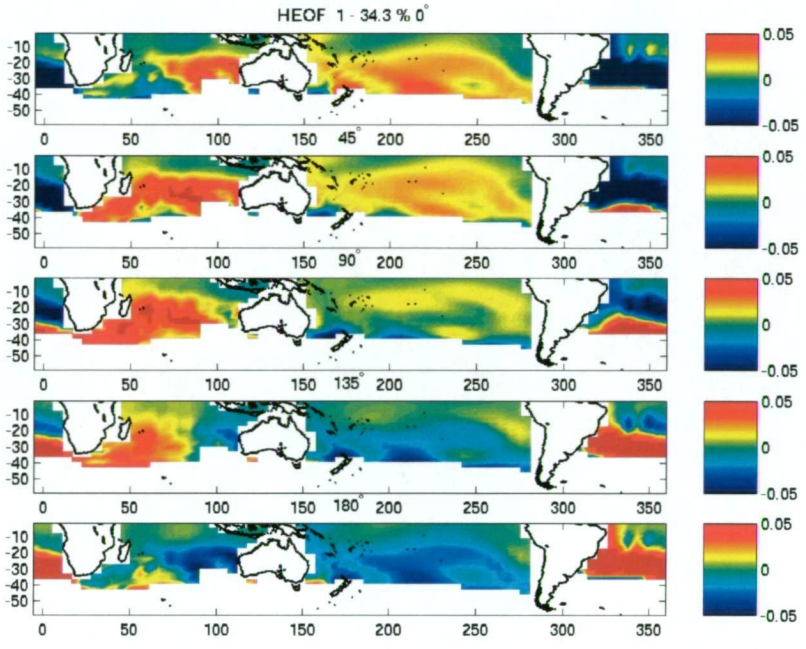

Figure 4.28: Spatial evolution of Mode 1 HEOF of potential temperature on neutral density surface $\gamma = 26.5$ kg.m^{-3}, calculated using 300 years of the c17 control model. The first panel shows the spatial state at the beginning (0°) of the cycle; the second panel shows the new spatial state after evolution through one eighth (45°) of a cycle; third, fourth and fifth panels show the spatial states at one quarter (90°), three eighths (135°) and one half (180°) of evolution of a cycle respectively.

the globe at any particular time there exists between 1 to 2 complete cycles (zonal wavenumber 1-2). However, it is hard to confirm this result given that the data excludes areas subject to seasonal outcropping.

Mode 2 (Figure 4.29) operates on similar frequency to mode 1 with average cycle length 15-20 years (Figure 4.27 (b)). Once again, the highest variability occurs in the Indian and Pacific Oceans where anomalies exceed 0.05°C. Similar to mode 1, in each ocean there tends to be a positive (negative) anomaly which dominates most of the ocean. This suggests that mode 1 and 2 may be a single stationary wave, with the variability being on an ocean

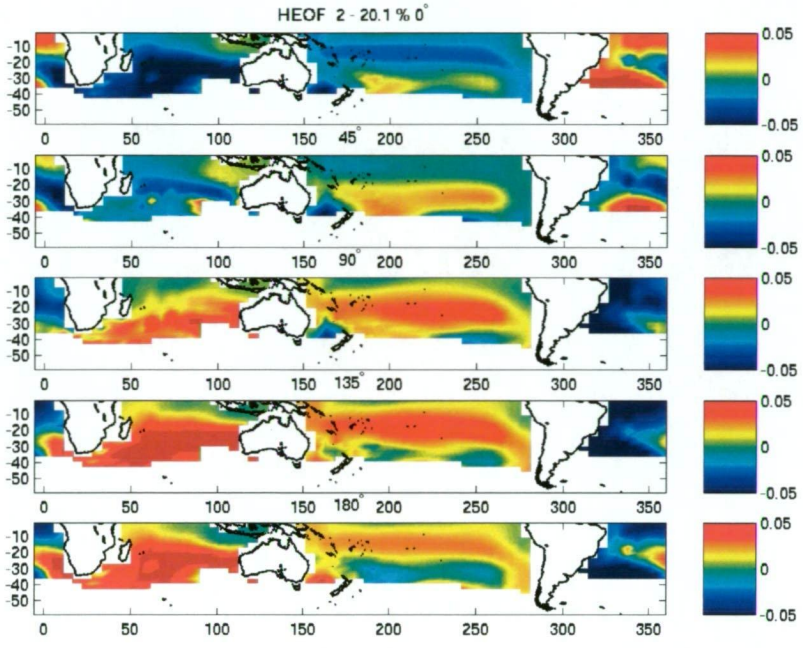

Figure 4.29: Spatial evolution of Mode 2 HEOF of potential temperature on neutral density surface $\gamma = 26.5$ kg.m^{-3}, calculated using 300 years of the c17 control model. The first panel shows the spatial state at the beginning (0°) of the cycle; the second panel shows the new spatial state after evolution through one eighth (45°) of a cycle; third, fourth and fifth panels show the spatial states at one quarter (90°), three eighths (135°) and one half (180°) of evolution of a cycle respectively.

basin scale.

The average cycle length of mode 3 (Figure 4.30) is also around 15-20 years (Figure 4.27) (e)). This mode differs substantially in spatial structure to modes 1 and 2. There is still relatively strong variability in the Indian and Atlantic (off east coast of South America) Oceans. However, much lower levels of variability occur within the ocean basins. Propagation around the ACC occurs in the Pacific Ocean but is not clear in the other ocean sectors.

Mode 4 (not shown) is stationary and dominated by anomalies in the Indian and Pacific Oceans. The ocean interiors show low levels of variability. The

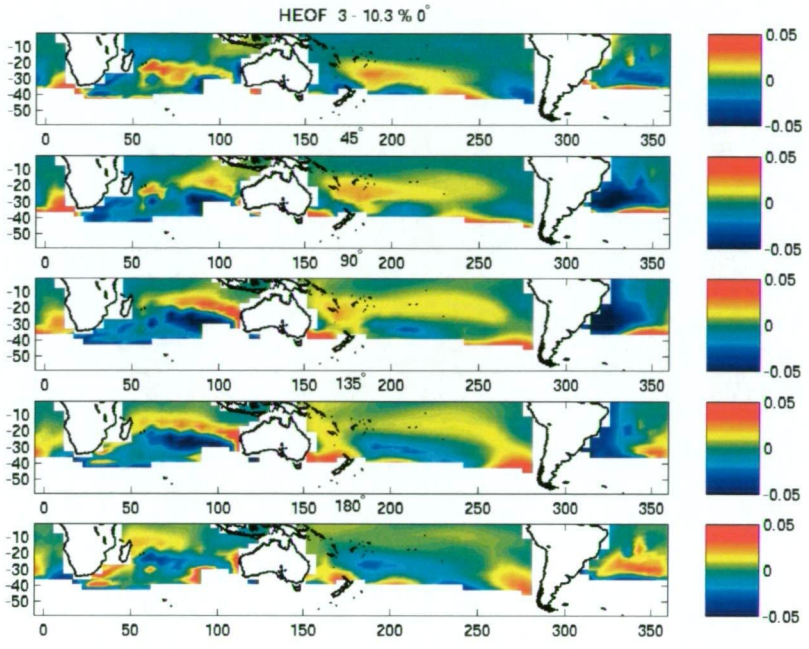

Figure 4.30: Spatial evolution of Mode 3 HEOF of potential temperature on neutral density surface $\gamma = 26.5$ kg.m^{-3}, calculated using 300 years of the c17 control model. The first panel shows the spatial state at the beginning (0°) of the cycle; the second panel shows the new spatial state after evolution through one eighth (45°) of a cycle; third, fourth and fifth panels show the spatial states at one quarter (90°), three eighths (135°) and one half (180°) of evolution of a cycle respectively.

zonal wavenumber structure is approximately 2 and the average cycle length is 6 to 10 years.

On 26.5 kg.m^{-3} the first 3 modes are dominated by low frequency (15 to 20 years). The zonal wavenumber was 1 or 2 for all modes except mode 3 which showed zonal wavenumber 3 structure. The dominance of the low frequency signal is likely due to the fact that the regions where this surface existed in the ACC had to be excluded due to their outcrop (at some point in the 100 year timeseries). This lead to the analysis being bias toward areas where the surface is deeper. However, we note that the results do tend to agree with

Variance Explained (%)	Mode 1	Mode 2	Mode 3	Mode 4
26.5 kg.m^{-3}	34	20	10	7
27 kg.m^{-3}	21	17	15	9
27.5 kg.m^{-3}	28	20	16	10

Table 4.4: Variance in temperature on neutral density surfaces explained by four modes of a HEOF analysis. The spatial domain of the density surface is the Southern Ocean.

previous results on depth surfaces of a decadal, zonal wavenumber 2 mode and an interannual zonal wavenumber 3 mode.

HEOF of potential temperature on 27 kg.m^{-3}

On 27 kg.m^{-3} the first four modes explain over 60% of the variance (21%, 17%, 15% and 9% respectively (Table 4.4)). It is interesting that the shallower surface (26.5 kg.m^{-3}) showed a higher concentration of energy in the first four modes (70%) as the reverse is intuitively expected (at deeper depths there should be less noise resulting in a smaller number of useful modes with high variance). As noted previously, the HEOF analysis discards the use of grid points where the surface has experienced outcropping. Neutral density surface 26.5 kg.m^{-3} experiences far more latitude movement of its outcrop area, and hence a lot of the shallower, well ventilated data, has been discarded. Hence, the larger proportion of variance in the denser surface, here equates to a larger amount of the data occurring at shallower depths, where more noise occurs. The large anomalies on the 27 kg.m^{-3} surface are about 0.01°C for an individual mode.

The first 2 modes (Figures 4.32 and 4.33) operate on low frequency (15 to 20

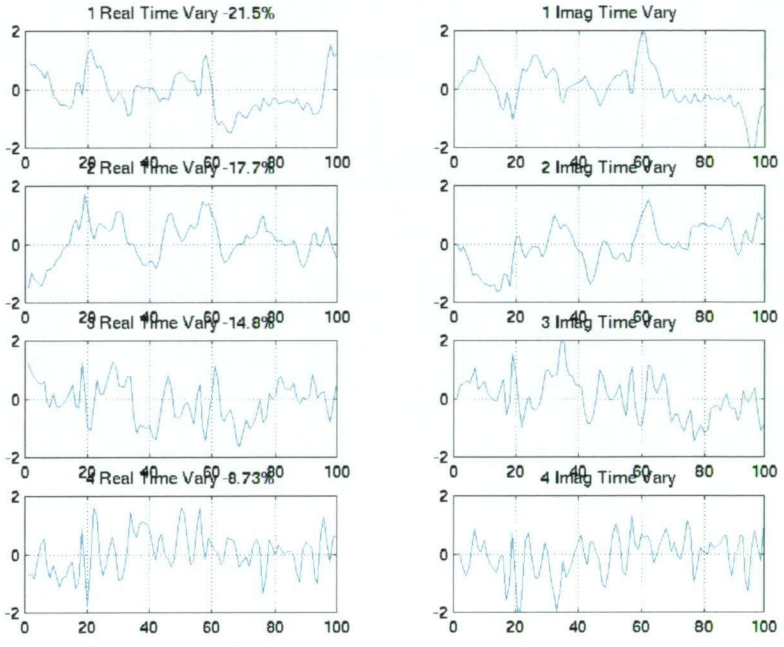

Figure 4.31: Real (upper left panel) and imaginary (upper right panel) components of the time evolution of Mode 1 of a HEOF of potential temperature on neutral density surface $\gamma = 27.0$ kg.m^{-3}, showing the variation of magnitude of anomalies throughout the time series. Second, third and bottom levels show equivalent Figures for modes 2 to 4. Calculated using 300 years of the c17 control model run.

years), whereas modes 3 and 4 (Figures 4.34 and 4.35) are higher frequency (4 to 5 years), (see Figure 4.31). Spatially, the first 3 modes contain high variability throughout each of the ocean basins, whereas mode 4 consists of high variability confined mainly near areas of outcrop in the ACC.

The first two modes (Figures 4.32 and 4.33) are composed of zonal wavenumber structure 1 to 2. There is some propagation in mode 1 but little to suggest circumpolar propagation in either of these modes. These modes most likely represent standing waves.

In mode 3 (Figure 4.34) there is more propagation. Anomalies appear to

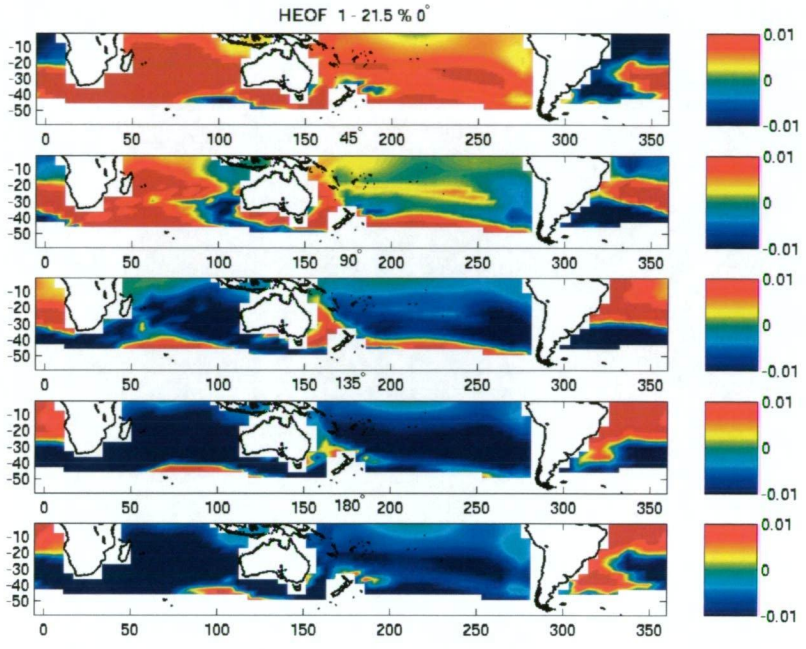

Figure 4.32: Spatial evolution of Mode 1 HEOF of potential temperature on neutral density surface $\gamma = 27.0$ kg.m^{-3}, calculated using 300 years of the c17 control model. The first panel shows the spatial state at the beginning (0°) of the cycle; the second panel shows the new spatial state after evolution through one eighth (45°) of a cycle; third, fourth and fifth panels show the spatial states at one quarter (90°), three eighths (135°) and one half (180°) of evolution of a cycle respectively.

originate in the Atlantic Ocean and propagate to the Indian Ocean. The propagation does not continue throughout the Pacific Ocean. The zonal wavenumber structure is 1 to 2 and the average cycle length is 4.5 years. The first 3 modes tend to have large anomalies throughout most of the Southern Hemisphere.

In the fourth mode (not shown) there is propagation in each of the oceans. It is unclear whether propagation is circumpolar. Here the zonal wavenumber varies between 2 to 4 and the average cycle length is 4 to 5 years.

On neutral density surface 27 kg.m^{-3}, the zonal wavenumber structure and

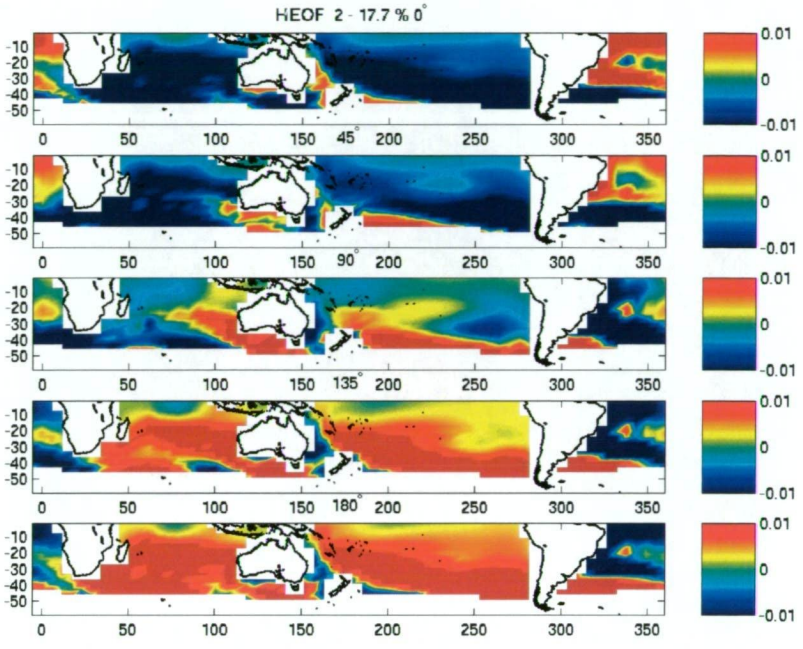

Figure 4.33: Spatial evolution of Mode 2 HEOF of potential temperature on neutral density surface $\gamma = 27.0$ kg.m^{-3}, calculated using 300 years of the c17 control model. The first panel shows the spatial state at the beginning (0°) of the cycle; the second panel shows the new spatial state after evolution through one eighth (45°) of a cycle; third, fourth and fifth panels show the spatial states at one quarter (90°), three eighths (135°) and one half (180°) of evolution of a cycle respectively.

frequency tended to increase with modes. Specifically, this surface is dominated by a decadal signal with zonal wavenumber structure of 1 to 2. Propagation is not detected. The higher modes show interannual variability of propagating waves with zonal wavenumbers of between 1 and 4. These results tend to confer with results seen on depth surfaces which revealed two dominant signals: a decadal signal of approximately zonal wavenumber 1 and an interannual signal of approximately zonal wavenumber 3.

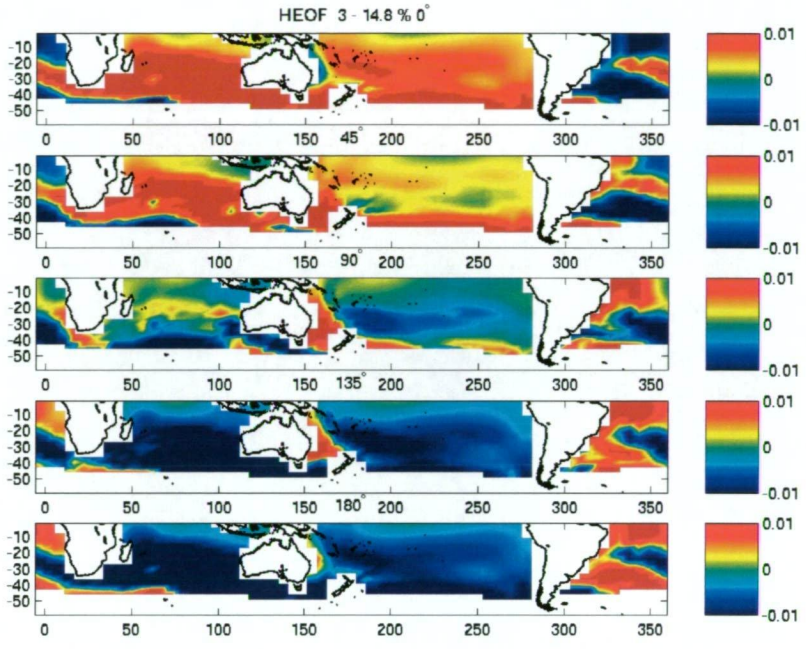

Figure 4.34: Spatial evolution of Mode 3 HEOF of potential temperature on neutral density surface γ = 27.0 kg.m^{-3}, calculated using 300 years of the c17 control model. The first panel shows the spatial state at the beginning (0°) of the cycle; the second panel shows the new spatial state after evolution through one eighth (45°) of a cycle; third, fourth and fifth panels show the spatial states at one quarter (90°), three eighths (135°) and one half (180°) of evolution of a cycle respectively.

HEOF of potential temperature on 27.5 kg.m^{-3}

On neutral density surface 27.5 kg.m^{-3}, the first 4 modes make up over 74% of the variance (28%, 20%, 16% and 10%) (Table 4.4). As expected, the variance explained by the top 4 modes has increased as we move to a denser, deeper level. All 4 modes at this level showed clear propagation that is mostly circumpolar (Figures 4.37 to 4.39). Anomaly size is around 0.01°C

Mode 1 (Figure 4.37) shows a zonal wavenumber structure of 1. Anomalies are restricted to within around 10° or 20° of latitude to the outcrop and

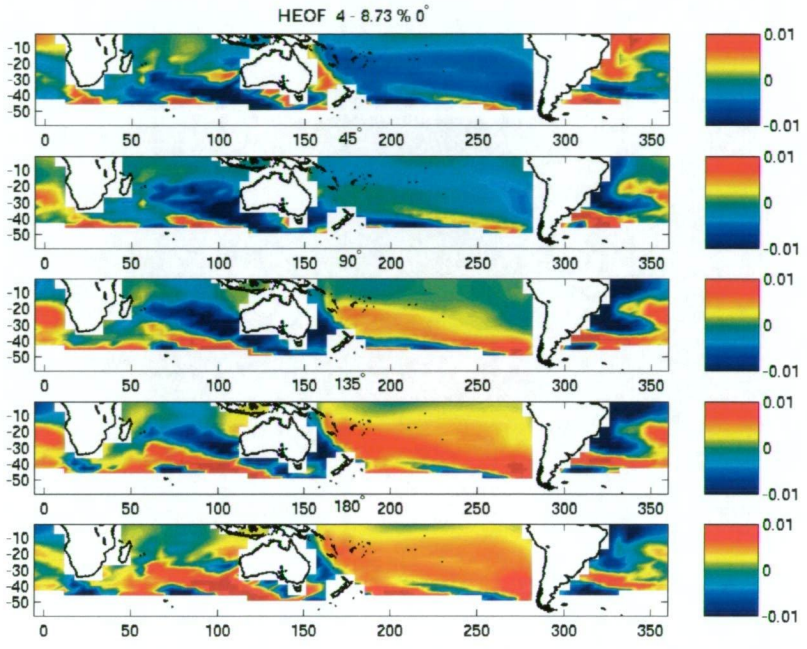

Figure 4.35: Spatial evolution of Mode 4 HEOF of potential temperature on neutral density surface $\gamma = 27.0$ kg.m^{-3}, calculated using 300 years of the c17 control model. The first panel shows the spatial state at the beginning (0°) of the cycle; the second panel shows the new spatial state after evolution through one eighth (45°) of a cycle; third, fourth and fifth panels show the spatial states at one quarter (90°), three eighths (135°) and one half (180°) of evolution of a cycle respectively.

clearly circumnavigate the globe. The average cycle length is 5 or 6 years.

Model 2 (Figure 4.38) shows a zonal wavenumber 2. Again, anomalies can be tracked traveling around the globe and are restricted to below around 30°S. The timescales of these anomalies is around 4-5 years.

Mode 3 (Figure 4.39) shows a dominant zonal wavenumber 3 structure and circumpolar propagation. Similar to mode 2, cycles in mode 3 are on timescales 4-5 years and occur mainly south of 30°S

Mode 4 (not shown) is zonal wavenumber 1 and is the lowest frequency, acting on timescales 6 or 7 years. These anomalies show some propagation

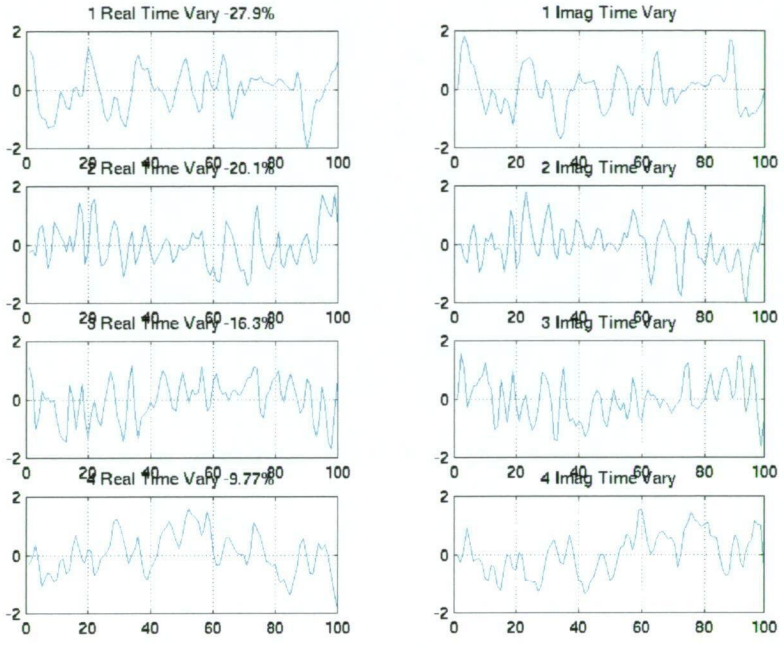

Figure 4.36: Real (upper left panel) and imaginary (upper right panel) components of the time evolution of Mode 1 of a HEOF of potential temperature on neutral density surface $\gamma = 27.5$ kg.m^{-3}, showing the variation of magnitude of anomalies throughout the time series. Second, third and bottom levels show equivalent Figures for modes 2 to 4. Calculated using 300 years of the c17 control model run.

(mainly in the Atlantic and Indian Oceans) however it does not appear to be circumpolar propagation. The Pacific Ocean tends to show a standing wave pattern.

On neutral density surface 27.5 kg.m^{-3}, circumpolar propagation occurred on all dominant modes. This compares well with hovmoeller diagrams of potential temperature anomalies seen in Section 4.1. The first 3 modes were all interannual signals with timescales of 4 to 6 years. This is similar to observed variability in the ACC. Interannual variability also occurred in HEOFs of potential temperature on depth surfaces, but the spatial structure of

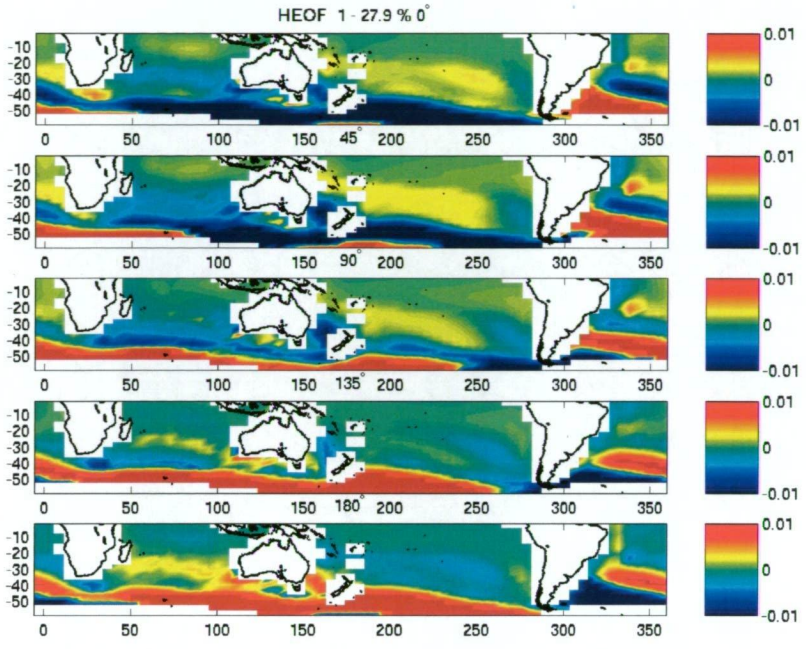

Figure 4.37: Spatial evolution of Mode 1 HEOF of potential temperature on neutral density surface $\gamma = 27.5$ kg.m^{-3}, calculated using 300 years of the c17 control model. The first panel shows the spatial state at the beginning (0°) of the cycle; the second panel shows the new spatial state after evolution through one eighth (45°) of a cycle; third, fourth and fifth panels show the spatial states at one quarter (90°), three eighths (135°) and one half (180°) of evolution of a cycle respectively.

variability was much less clear than occurred here.

Summary

For all neutral density surfaces, large amounts of variance were concentrated in the first 3 modes (>50%). This is compared with the results in section 4.3 where HEOFs of potential temperature anomalies on depth surfaces contained much less variance in the first 3 modes (<40%). This is because signals in properties on surfaces of constant depth have a component of variability due to the vertical fluctuation of isopycnals. Whereas, variability on neu-

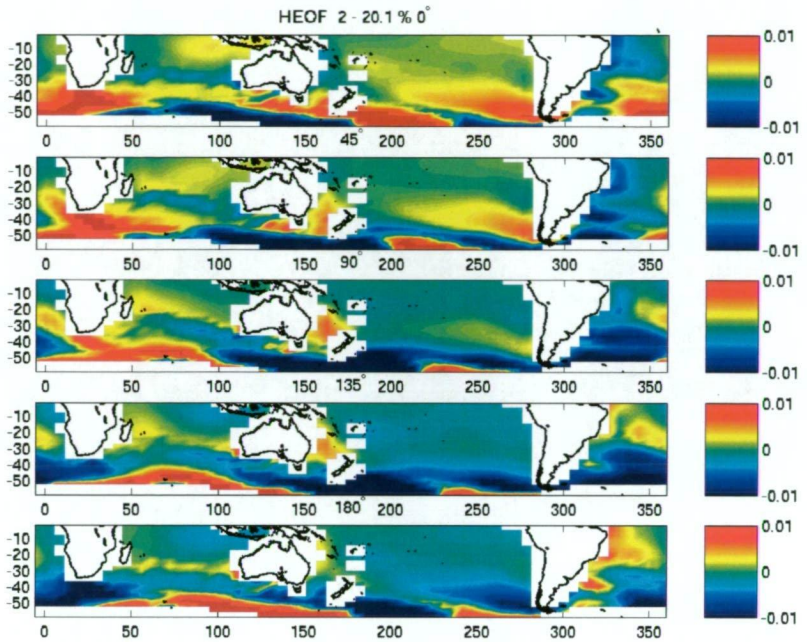

Figure 4.38: Spatial evolution of Mode 2 HEOF of potential temperature on neutral density surface $\gamma = 27.5$ kg.m^{-3}, calculated using 300 years of the c17 control model. The first panel shows the spatial state at the beginning (0°) of the cycle; the second panel shows the new spatial state after evolution through one eighth (45°) of a cycle; third, fourth and fifth panels show the spatial states at one quarter (90°), three eighths (135°) and one half (180°) of evolution of a cycle respectively.

tral density surfaces give information on surface forcing only. This leads to generally more noise on constant depths surfaces.

Also, on increasing constant depth surfaces, the concentration of variance within the first few modes increased. This was expected since the ocean naturally filters noise from signals. This result differed on constant neutral density surfaces. Here the lighter neutral density surface 26.5 kg.m^{-3} (71% in the first 4 modes) had a greater concentration of variance than a denser surface 27 kg.m^{-3} (62% in the first 4 modes). The densest surface (27.5 kg.m^{-3}) showed 74% of variance in the first 4 modes. The reason for this is

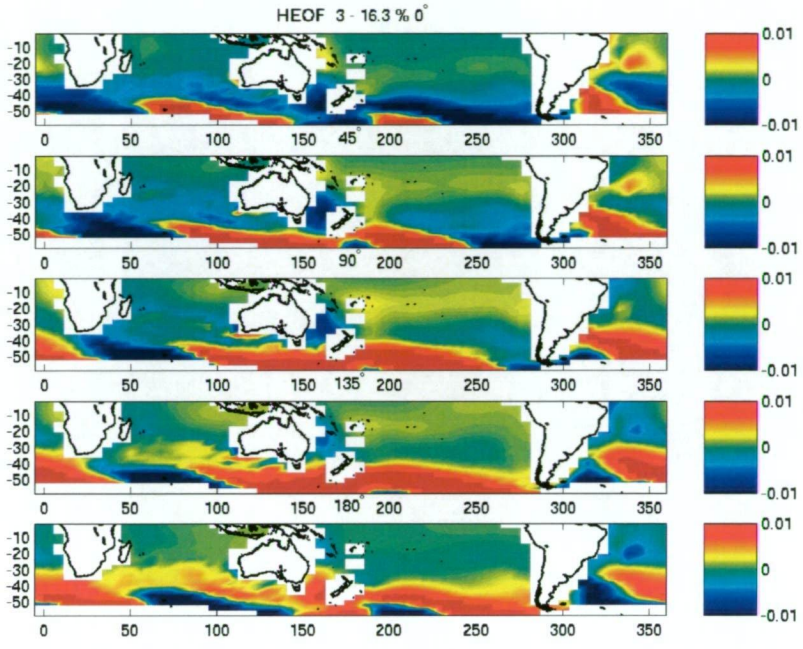

Figure 4.39: Spatial evolution of Mode 3 HEOF of potential temperature on neutral density surface $\gamma = 27.5$ kg.m^{-3}, calculated using 300 years of the c17 control model. The first panel shows the spatial state at the beginning (0°) of the cycle; the second panel shows the new spatial state after evolution through one eighth (45°) of a cycle; third, fourth and fifth panels show the spatial states at one quarter (90°), three eighths (135°) and one half (180°) of evolution of a cycle respectively.

that the dataset for the lighter surface was considerably limited due to the large latitude movement of its outcrop region. In the HEOF, although the surface is lighter, there was overall less data that was "shallow" compared to the denser surface. Hence the variability that occurred on the lighter surface tended to have less noisy signals, which in turn increased the variance in regular modes. Overall, potential temperature on neutral density surfaces showed two differing dominant signals. The first was a decadal signal with a zonal wavenumber 1 to 2. The second was an interannual signal with zonal wavenumber 3 to 4. The interannual variability was dominant on the denser

surface (27.5 $kg.m^{-3}$) because this surface showed the least movement in its outcrop region and allowed more shallow data to be included in the analysis. The less dense surfaces were less reliable in this sense and as a result the interannual variability showed a weaker presence. Also due to being reduced datasets, circumpolar navigation could not be resolved in the two shallower surfaces. On the denser surface (27.5 $kg.m^{-3}$), circumpolar propagation was seen clearly.

Chapter 5

Atmosphere and Ocean interaction and Ocean Variability

5.1 Atmosphere Forcing and Water Mass variability

Here I discuss the distribution of RMS variability in heat flux and winds. In this area I have calculated RMS variability using both monthly and annually averaged data sets. Further, using the annually averaged data sets, I then used a filter to determine variability in individual period bands (similar to those applied to the salinity and temperature data sets). The results were such that the spatial distribution was similar for all period bands. Also, the variance simply dropped off as period increased (see Table 5.1). This reflects

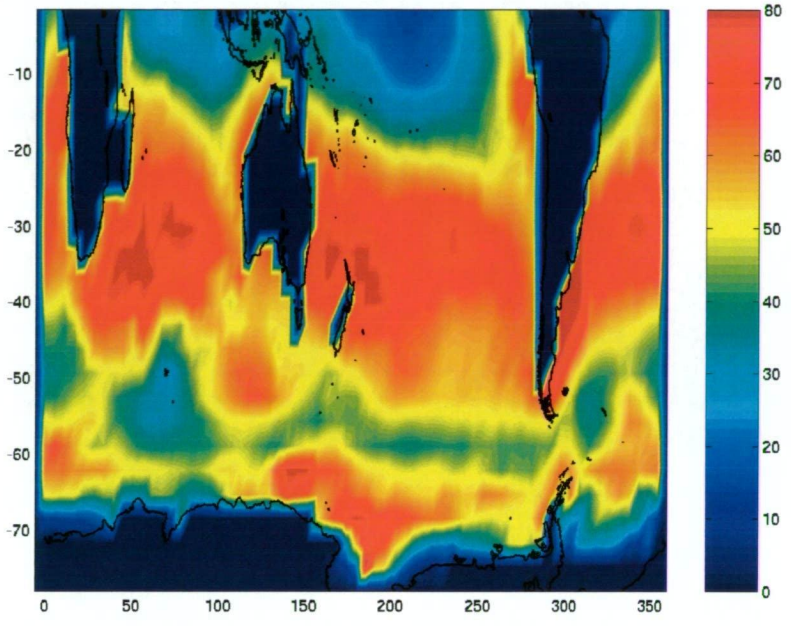

Figure 5.1: RMS variability of monthly averaged heat flux ($W.m^{-2}$) using control model years 1880-2179.

the high period nature of atmospheric variables. As a result I will discuss only the monthly and annually averaged results. Using annual averages, the RMS variability of heat flux (see Figure 5.2) shows that the largest heat flux variations are seen in the Pacific and Atlantic sectors at about 60°S as well as in the Indian ocean (40-45°S). This clearly corresponds well with temperature variability at 12.5 m. It is worth exploring whether this result is due to the variation of sea ice extent which would prevent much heat exchange in winter months. The equivalent picture using monthly averages (Figure 5.1) shows a very different spatial picture and around four times the energy in variability peaks (approx. $> 80\ W/m^2$ compared to $> 20\ W/m^2$) compared to that using annual averages. Areas of high variability (monthly averages) occur

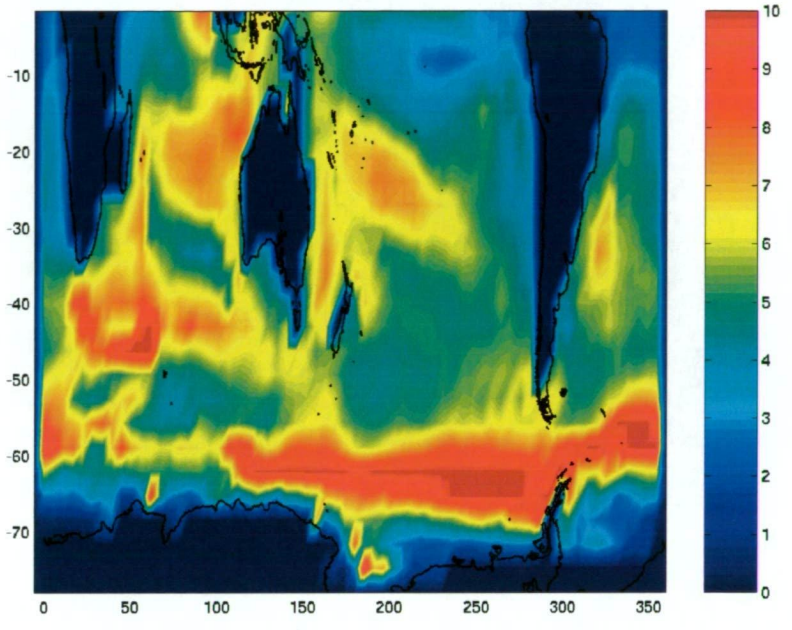

Figure 5.2: RMS variability of annually averaged heat flux ($W.m^{-2}$) using control model years 1880-2179.

Band Pass Filter (years)	> 1	$1-3$	$3-8$	$8-16$	$16-32$
Heat Flux ($W.m^{-2}$)	> 10	> 7	> 7	> 5	> 4
Zonal Winds ($dynes.cm^{-1}$)	> 0.2	> 0.1	> 0.1	> 0.07	> 0.05
Meridional Winds ($dynes.cm^{-1}$)	> 0.12	> 0.07	> 0.07	> 0.04	> 0.04

Table 5.1: Energy of annually averaged variability peaks for heat flux, zonal winds and meridional wind; and bandpass filters.

between 40° and 10°S. This reflects regions where there is a large change in ocean temperature between summer and winter.

Zonal wind stress RMS variability patterns using annually and monthly averaged data (Figures 5.4 and 5.3 respectively) reveal similar spatial distributions. Both showed high variability over the entire Southern Ocean. Exceptions to the high variability include regional activity on and around Antarctica (using monthly averages) and relatively high variance in the Indian ocean at around 45°S (also using monthly averages). The magnitude of the peaks

was about four times larger using monthly averages ($> 0.8\ dynes.cm^{-1}$ compared to $> 0.2\ dynes.cm^{-1}$).

Meridional wind stress spatial variability patterns are also similar for both annually and monthly averaged data (Figures 5.6 and 5.5 respectively). With the exception of strong regional variability in coastal areas in the monthly averaged results, high variability occurs throughout the Southern Ocean . Again the variability peaks show around 4 times the energy in the monthly averaged data ($> 0.5\ dynes.cm^{-1}$ compared to $> 0.12\ dynes.cm^{-1}$).

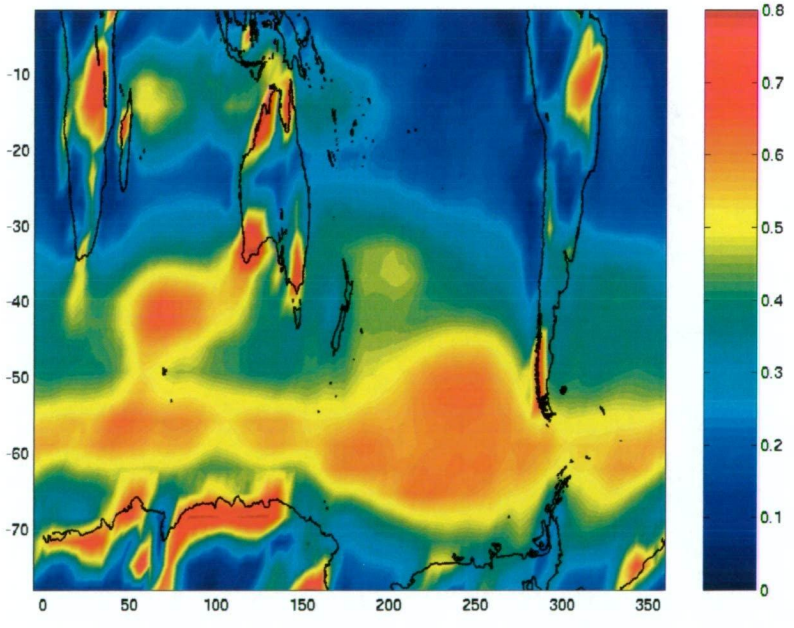

Figure 5.3: RMS variability of monthly averaged Zonal Wind Stress ($dynes.cm^{-1}$) using control model years 1880-2179. Horizontal axis is Longitude (°E) and vertical axis is Latitude (°S).

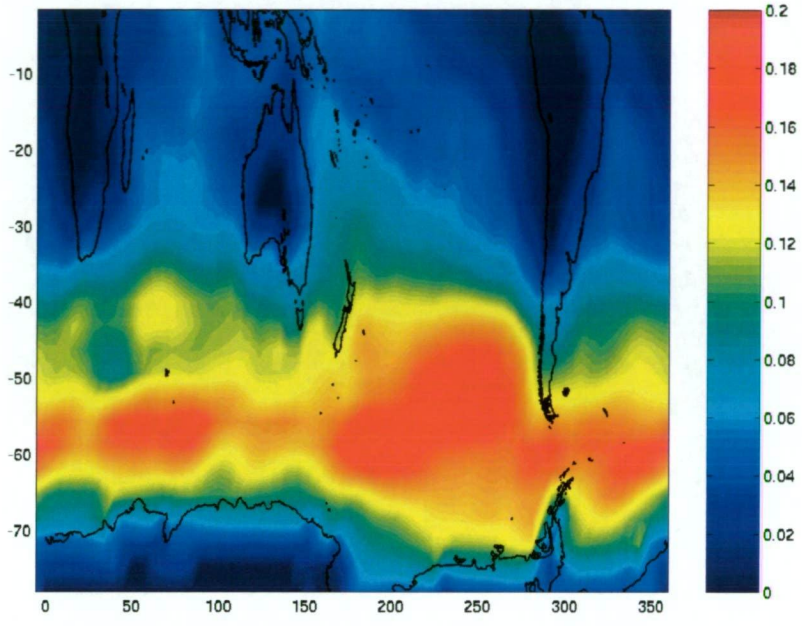

Figure 5.4: RMS variability of annually averaged zonal wind stress ($dynes.cm^{-1}$) using control model years 1880-2179. Horizontal axis is Longitude (°E) and vertical axis is Latitude (°S).

HEOFs of heat flux

Modes 1 and 2 of heat flux contain 8 and 6 % of variability respectively (Figures 5.7 and 5.8). They both show a propagating wave, with zonal wavenumber 3. The propagation in mode 1 is eastward and in mode 2 it is westward. Hence it is apparent that mode 1 and 2 of the HEOF analysis represent a dominant stationary wave with zonal wavenumber 3 structure. High frequency dominate this mode with cycles all shorter than 2 or 3 years. Compared with the RMS variability of heat flux (described in section 3.1) this HEOF is quite revealing. Using RMS variability we were able to determine that there was high energy in midlatitudes in total variability (inclusive of seasonal cycles). Using only annual averages revealed high RMS energy

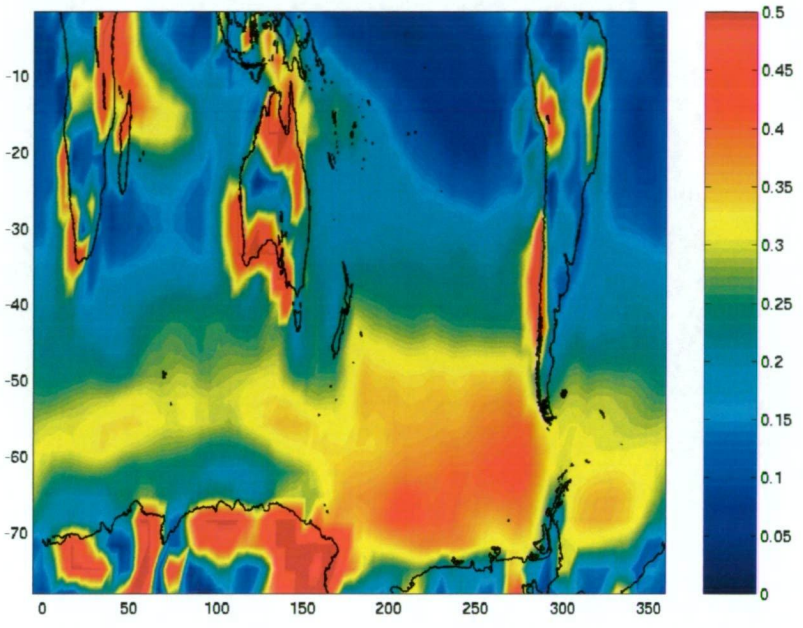

Figure 5.5: RMS variability of monthly averaged meridional wind stress ($dynes.cm^{-1}$) using control model years 1880-2179. Horizontal axis is Longitude (°E) and vertical axis is Latitude (°S).

primarily at around 60°S in the Pacific Ocean. Here, we see that there is a dominant stationary wave which operates at high frequency at all longitudes between 40 and 60°S. This was not revealed by analysis of RMS variability. Further, magnitudes of the mode are approximately 3 and the strongest anomalies occur within the Pacific Ocean (agrees with result determined in chapter 3.1)

Mode 3 (not shown) explains less variance (4%) with high frequency variations (< 3 years). The spatial structure of of anomalies around the globe is approximately zonal wavenumber 2.

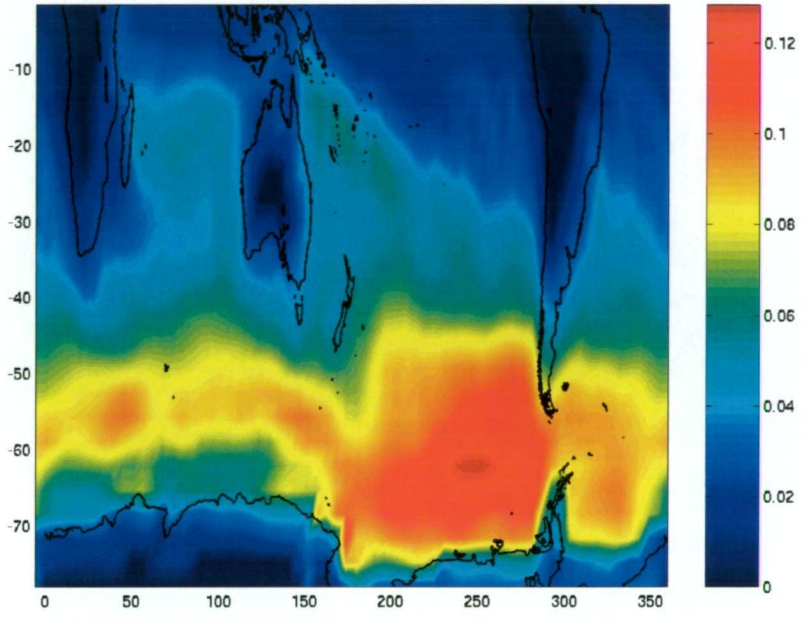

Figure 5.6: RMS variability of annually averaged meridional wind stress ($dynes.cm^{-1}$) using control model years 1880-2179. Horizontal axis is Longitude (°E) and vertical axis is Latitude (°S).

HEOFs of meridional wind stress

Mode 1 and 2 of the Meridional Wind stress anomaly (Figures 5.9 and 5.10) contains 13% and 10% of variance respectively. Mode 1 and 2 consist of eastward and westward propagating zonal wavenumber 3 waves respectively. Hence, similar to Modes 1 and 2 of potential temperature at 905 m and Modes 1 and 2 of heat flux anomaly, here the HEOF analysis has maximised the propagation by representing a near perfect stationary wave as two propagating waves. So the dominant mode is a zonal wavenumber 3 stationary wave with about 20% of variance. The timescales of this mode are at very high frequency ($<$ 1 to 2 years). Most of the variability occurs in the Southern Ocean between 40 and 70°S. The anomalies are oriented a NW-SW direction

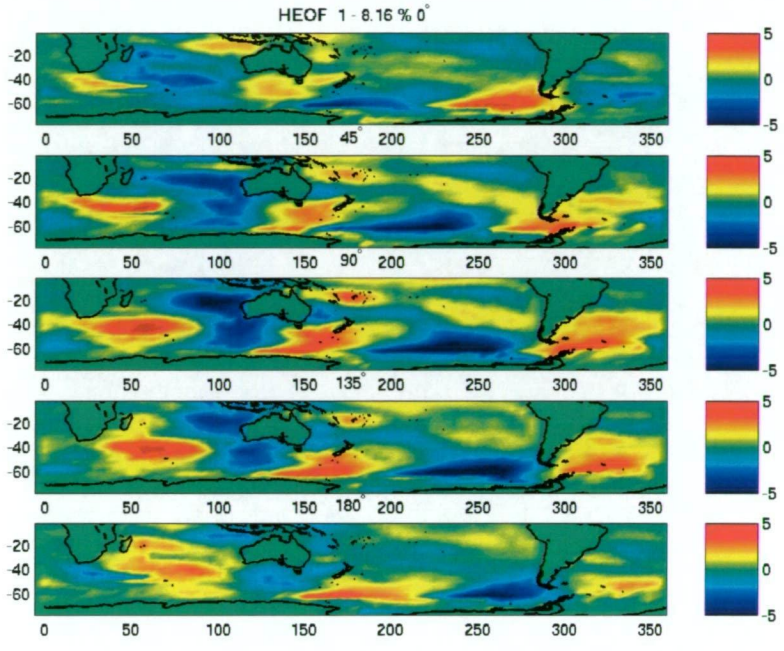

Figure 5.7: Spatial evolution of Mode 1 HEOF of heat flux calculated using 300 annually averaged years of the c17 control model. The first panel shows the spatial state at the beginning (0°) of the cycle; the second panel shows the new spatial state after evolution through one eighth (45°) of a cycle; third, fourth and fifth panels show the spatial states at one quarter (90°), three eighths (135°) and one half (180°) of evolution of a cycle respectively. Horizontal axis is Longitude (°E) and vertical axis is Latitude (°S).

and are of magnitudes of around 0.05. In section 3.1 we identified high RMS variability throughout the Southern Ocean, with particularly high levels in the Pacific. The same result occurs here. The HEOF analysis has furthered our understanding of Meridional Wind Stress as being dominated by the zonal wavenumber 3 stationary wave pattern.

Mode 3 of meridional wind stress (not shown) contains about 6% of variance and consists of a zonal wavenumber 4 pattern of anomalies which tend to show most energy in the Pacific and Atlantic Ocean. HEOF Modes of zonal wind stress are dominated by strong N-S gradients and are not shown.

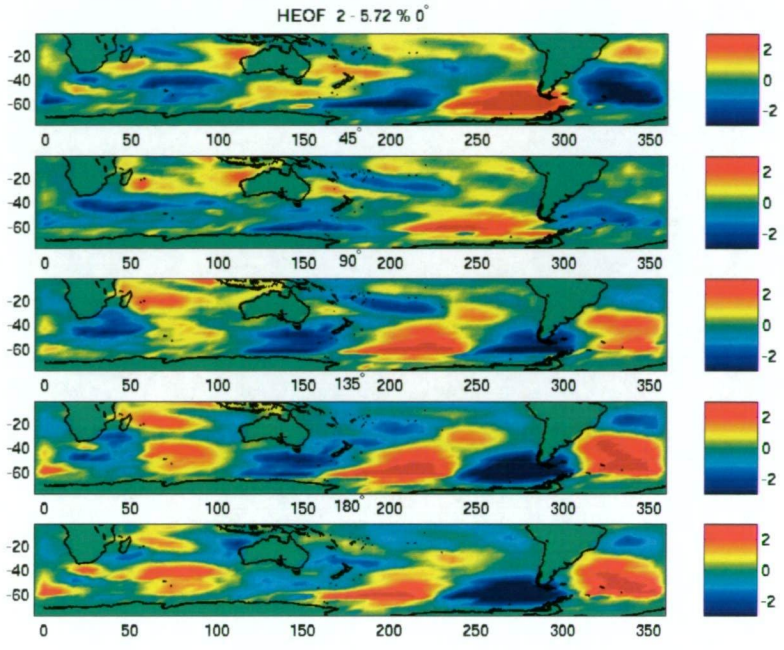

Figure 5.8: Spatial evolution of Mode 2 HEOF of heat flux calculated using 300 annually averaged years of the c17 control model. The first panel shows the spatial state at the beginning (0°) of the cycle; the second panel shows the new spatial state after evolution through one eighth (45°) of a cycle; third, fourth and fifth panels show the spatial states at one quarter (90°), three eighths (135°) and one half (180°) of evolution of a cycle respectively.

HEOFs of salinity flux

Mode 1 of salinity flux are shown in Figure 5.11. In the first 3 modes, much of the energy in salinity flux occurs north of 40°S and at high latitude (60°) near and over sea ice formation regions. Predominately, in all three modes, there is a NW-SE orientation of anomalies occurring across the Indian and Pacific Oceans. In the first mode, there is approximately 1.5 cycles of anomalies (ie. a positive anomaly between Africa and Australia and a positive and negative anomaly occurring between Australia and America) occurring between the West Indian Ocean and the East Pacific Ocean. In modes 2

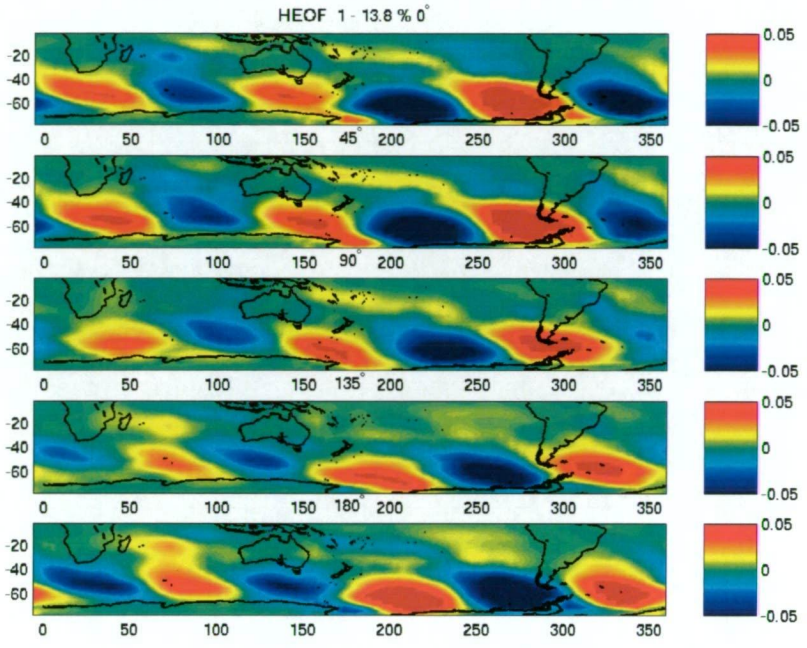

Figure 5.9: Spatial evolution of Mode 1 HEOF of meridional wind calculated using 300 annually averaged years of the c17 control model. The first panel shows the spatial state at the beginning (0°) of the cycle; the second panel shows the new spatial state after evolution through one eighth (45°) of a cycle; third, fourth and fifth panels show the spatial states at one quarter (90°), three eighths (135°) and one half (180°) of evolution of a cycle respectively.

and 3 (not shown), spatial complexity increases and the number of cycles occuring between these two oceans becomes 2.5 and 3.5 cycles respectively. Also, anomalies retreat further north as mode number and spatial complexity increases.

Summary of atmospheric variables

Over the southern ocean, primary modes of meridional wind and surface heat flux are dominantly zonal wavenumber 3. Unlike oceanic modes, these atmospheric modes tend to be stationary with propagation limited to only

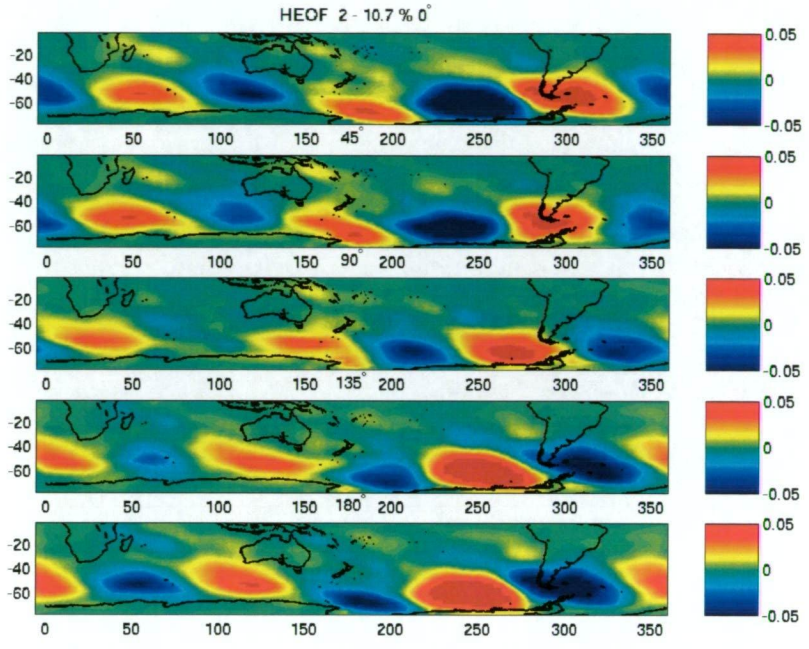

Figure 5.10: Spatial evolution of Mode 2 HEOF of meridional wind calculated using 300 annually averaged years of the c17 control model. The first panel shows the spatial state at the beginning (0°) of the cycle; the second panel shows the new spatial state after evolution through one eighth (45°) of a cycle; third, fourth and fifth panels show the spatial states at one quarter (90°), three eighths (135°) and one half (180°) of evolution of a cycle respectively.

some regions. High variance occurs around the globe within latitudes 30 to 60°S with the highest energy being seen in the Pacific Sector. Time scales are dominated by higher frequencies (biennial to interannual).

Meridional Wind

Ekman pumping caused by winds leads to a vertical fluctuation of density surfaces, whilst properties on the density surface remain relatively constant. This is reflected by a dominate, interannual, zonal wavenumber three spatial distribution of pressure anomalies on density surfaces. Since the properties

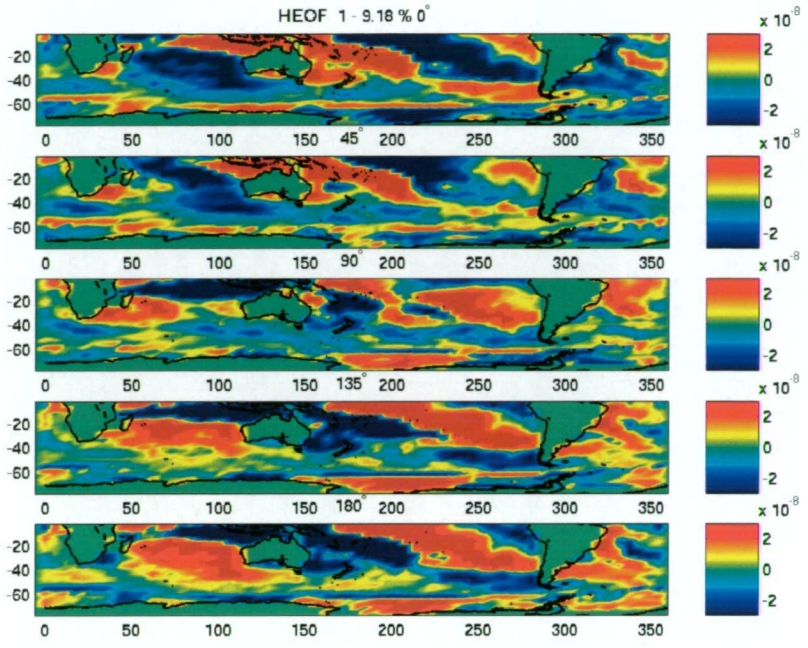

Figure 5.11: Spatial evolution of Mode 1 HEOF of the salinity flux calculated using 300 annually averaged years of the c17 control model. The first panel shows the spatial state at the beginning (0°) of the cycle; the second panel shows the new spatial state after evolution through one eighth (45°) of a cycle; third, fourth and fifth panels show the spatial states at one quarter (90°), three eighths (135°) and one half (180°) of evolution of a cycle respectively.

of salinity and temperature on a density surface remain unaffected, these fluctuations are less important for water mass property variations.

Heat Flux

Source waters for SAMW and AAIW are subject to strong interannual, zonal wavenumber three heat flux variability. Interannual zonal wavenumber three variability is seen on neutral density surfaces 26.5 - 27.5 as well as constant pressure surfaces 12.5 and 410 m. However the primary variability transferred to the ocean interior is decadal zonal wavenumber two. The ocean

has longer response times compared to the atmosphere so decadal timescales dominate its spectra. My thesis is interested as to how a dominant zonal wavenumber three pattern transforms to a zonal wavenumber two pattern. Some hypothesis I use for testing are as follows: 1. Transfer of anomalies from the atmosphere to the ocean is limited to regions where convection and subduction takes place. Since these regions are not evenly spatially distributed, the zonal wavenumber of the spatial distribution of convection regions will filter an atmospheric signal. 2. Wintertime cooling has a more significant affect on annual ocean anomalies compared to equivalent summertime warming. In this case we expect the variability of the wintertime heat flux to have a different character to that of the annual signal. 3. Non-uniform zonal distribution of heat flux energy could also lead to a convoluted spatial structure of resultant oceanic anomalies, particularly when coupled with specific regions of convection.

5.2 A simple model of the oceans modulation of atmospheric forcing.

In the previous section we saw that the ocean exhibited a dominant decadal zonal wavenumber 2 pattern and the atmosphere a dominant interannual zonal wavenumber 3 pattern. We hypothesis that much of the ocean signal is due to the ocean filtering of the atmosphere signal. In particular we suggest a mechanism for the filtering is the existence of two strong convection

regions globally. A simple test to disprove this hypothesis is to use a simple convection model inducing this scenario. In particular, solving a simple model which uses advection, convection, diffusion and atmospheric forcing terms using various scenarios we are able to obtain zonal wavenumber two patterns from a predominately zonal wavenumber three atmosphere forcing. The most significant scenario is as follows: Interannual, zonal wavenumber three forcing is applied to the ocean (Figure 5.12). Deep convection occurs only in two regions which overlap peaks (which are in phase) of the forcing term (Figure 5.13). The resultant oceanic anomaly shows a spatial structure zonal wavenumber two (Figure 5.14). This scenario is similar to the coupled model ocean, where density surfaces showed RMS energy peaks in primarily two regions: For example, examining meridional slices and mean mixed layer depths, deep convection is seen occurring in primarily two regions: SW of Australia (centred at 50°S,100°E) and in the Pacific sector (centred at 60°,250°E). Correspondingly, in primary HEOF modes of heat flux there is a tendency for heat flux anomalies over these regions to be in phase. Hence this result indicates that strength and location of convection regions may be a key factor in modulation of the zonal wavenumber three atmospheric signals. In particular the hypothesis that the zonal wavenumber 2 oscillation seen in the ocean may be a result of zonal filtering of an atmospheric zonal wavenumber 3 pattern appears qualitatively consistent with ocean and atmosphere patterns.

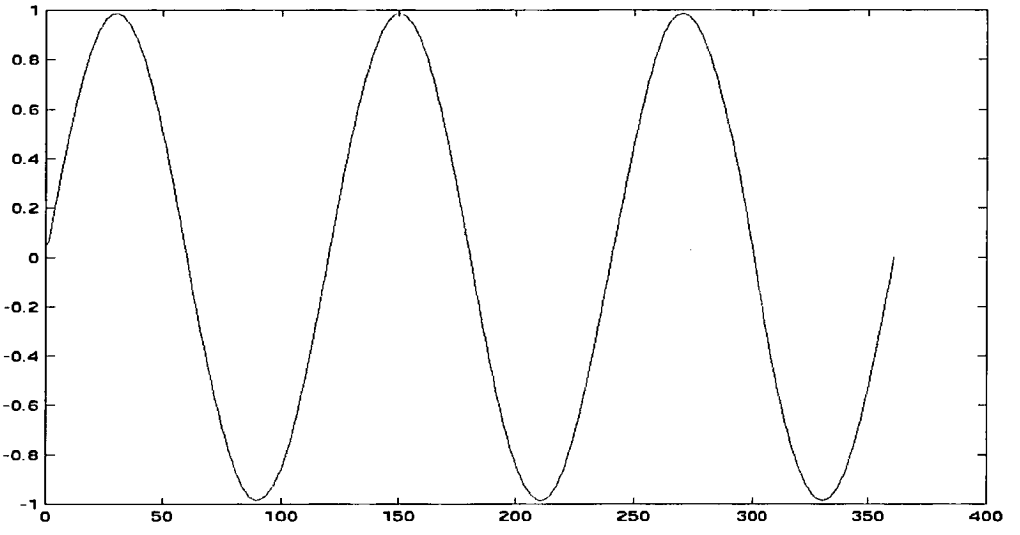

Figure 5.12: Atmosphere forcing applied to model

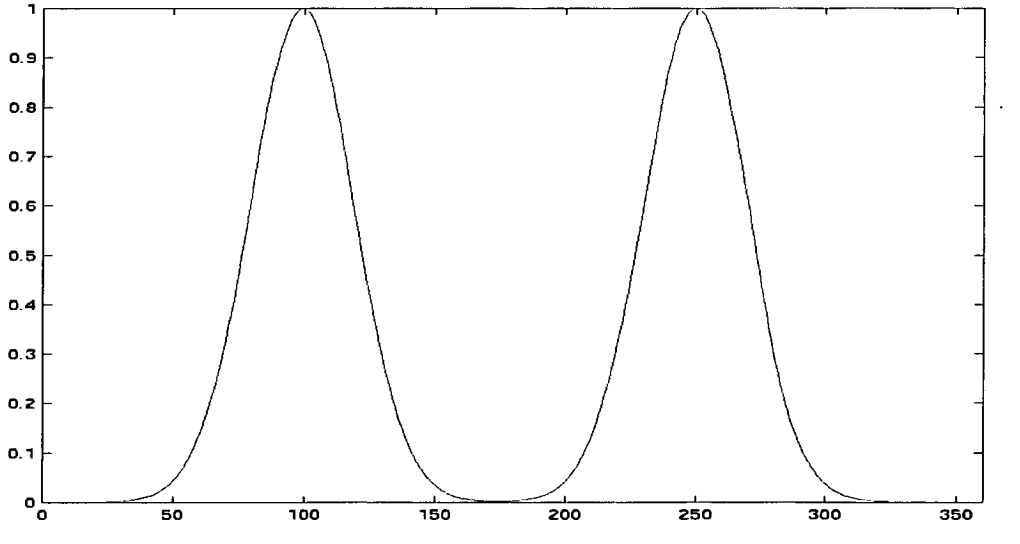

Figure 5.13: Convection regime applied to model

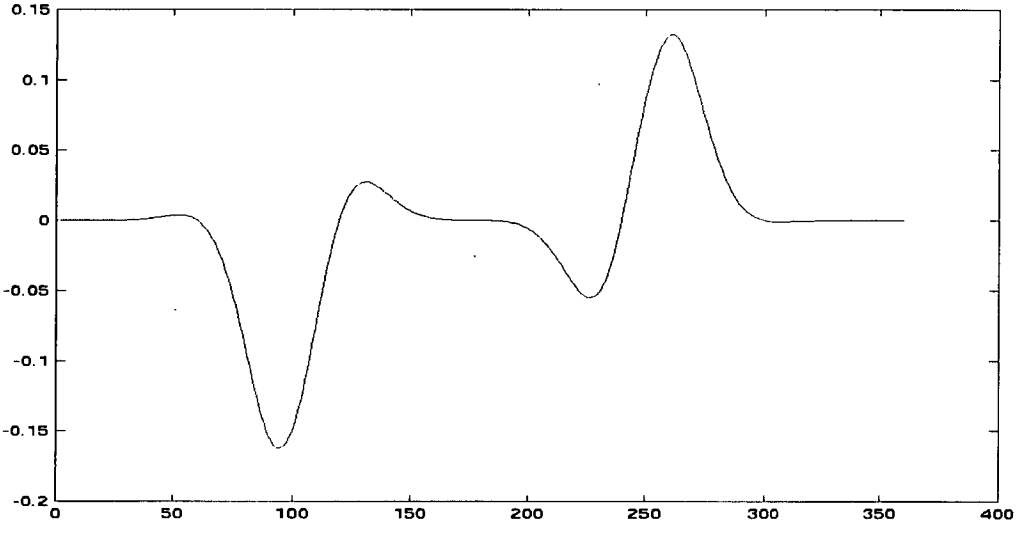

Figure 5.14: Resulting temperature anomaly within model

Chapter 6

Detection of Climate Change

6.1 Comparison between transient and control model runs

In this section I use fingerprinting techniques to compare control and transient model runs. The comparisons reveal whether signals of change in the ocean are attributable to natural variations or long term climate change. I focus on changes over meridional sections in the southern ocean inclusive of density surfaces 26 to 28 kgm^{-3}.

Typically, studies of climate change using ocean data involve examining changes in sea water properties from two time series. The time domain of the data may consist of transects performed on two occasions or the transect at the final or initial time may consist of a set of various data obtained at times surrounding the final or initial times. This data is then mapped onto the transect line using objective mapping. The result produced is a map of

change at a grid point, or along a trensect or depth profile.

Chapter 1 discussed a number of studies which examine changes over time. The observations typically consisted of data from two epochs, with an average of 30 years separation. This study follows suite. To examine the significance of the 30 year period, section 6.2 varies the time separation parameter between 10, 30 and 50 years. Each epoch of observed data consists of around 10 years of observations. Again, to mimic observed studies I generally epochs of length 11 years. The mean of all data from each epoch is used. For example, to compare the change in potential temperature between 1950 and 1980, I deduct the average temperature of 1945 to 1955 (epoch 1) from the average temperature between 1975 and 1985 (epoch 2). The actual fingerprint method used here is calculation of an uncentered statistic (as used by Santer et al. (1995), Banks and Wood (2002)). For a map of change of temperature over a given period (say 30 years), we represent the change as P(x), where x = 1, n gridpoints. This map of change may be obtained from observations or from a simulation of climate change using a transient model run.

To compare the pattern of change $P(x,k)$ (x and k represent the spatial and time domains respectively) with the simulated control run and transient runs we calculated uncentered statistics u(t) and v(t):

$$u(t) = \frac{\sum_{x=0}^{n} P(x)C(x,k)}{\sum_{x=0}^{n} P(x)P(x)} \text{ and } v(t) = \frac{\sum_{x=0}^{n} P(x)T(x,k)}{\sum_{x=0}^{n} P(x)P(x)}$$

where C(x,k) is the temperature change seen between year t and t+30 in the control run (T(x,k) is obtained from the transient run) and t is any given year. ie. $C(x, 1950) = \theta(x, 1980) - \theta(x, 1950)$ (θ is potential temperature).

In the following experiments we will set specific parameters as constant. The first of these parameters is the use in the calculation of P(x). Generally, P(x) is defined as follows: $P(x,k) = \frac{1}{2p+1}[\sum_{i=-p}^{p} \theta(x, k+i+l) - \theta(x, k+i)]$

where $2p+1$ is the number of years to average over, and l is the number of years between data sets and x is the spatial variable. For example, this study uses values of $2p+1 = 11$ years and $l = 30$ years in order to best replicate the observational data used for comparison.

I perform the experiments using properties on a set of neutral density surfaces 26 to 28 kgm^{-3} (increments of 0.2 kgm^{-3}). Results discussed are from experiments conducted along the 110°E and 150°E meridional sections. For each meridional section I use a map of change as the comparison data set. This is calculated using transient model output as one of the following: the difference between the years 1980 and 1950 as well as the difference between the years 2030 and 2000, where properties at 1980 and 1950 are calculated as the average of properties from 1975 to 1985 and 1945 to 1955 respectively.

6.2 Changes in potential temperature and pressure on neutral density surfaces at 110°E.

Figure 6.1 (a) shows the map of change between 1950 and 1980 of potential temperature on neutral density surfaces 26 to 27 kgm^{-3} along 110°E. The general trend is cooling on isopycnals in the mode and shallow waters (north of 45°S and up to 500 m) and a slight warming in the AAIW (near the

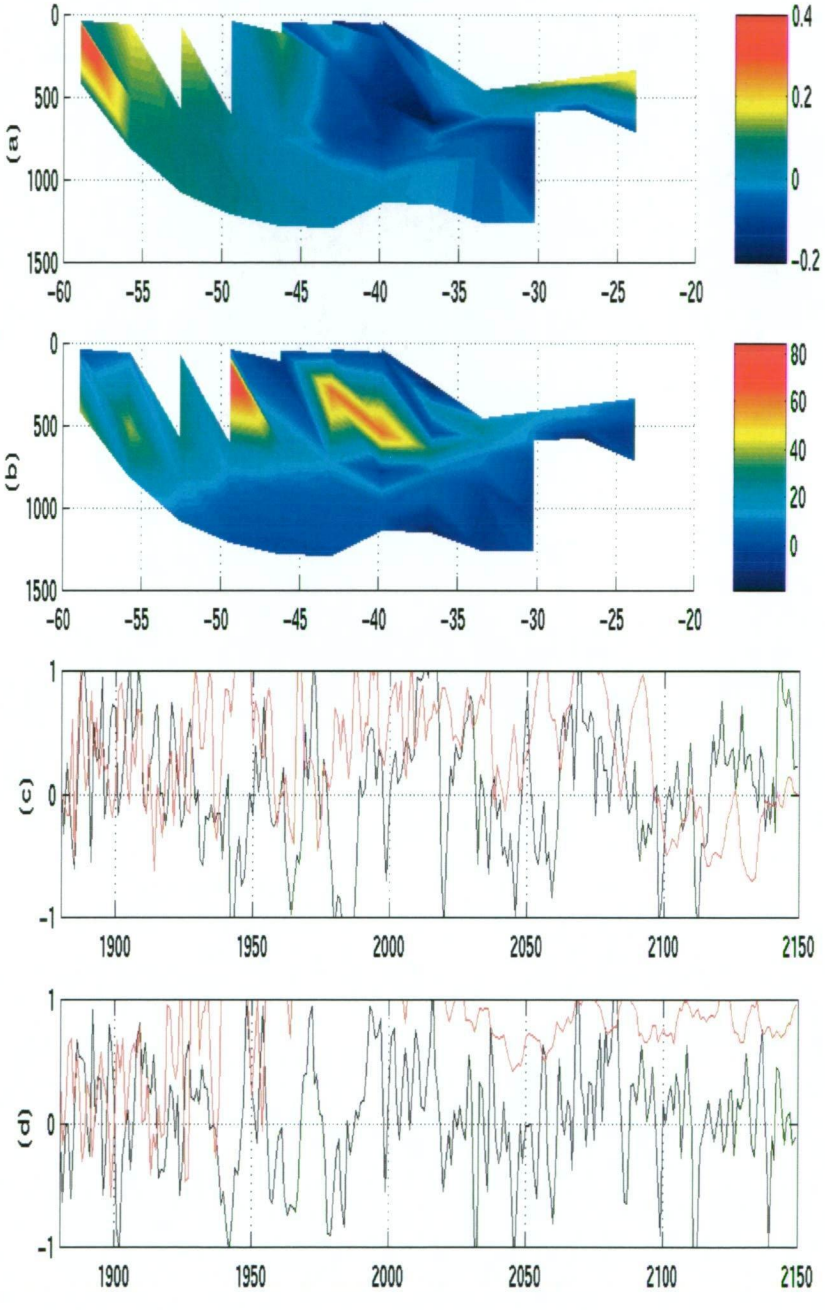

Figure 6.1: (a) $P_\theta(x, 1950)$, $P_\rho(x, 1950)$; (c) u(t) (black) and v(t) (red) for Potential Temperature (θ) and (d) u(t) (black) and v(t) (red) for pressure (ρ); for p = 5 and l = 30 along 110°E. Significance (p¡0.5) is greater than 0.5.

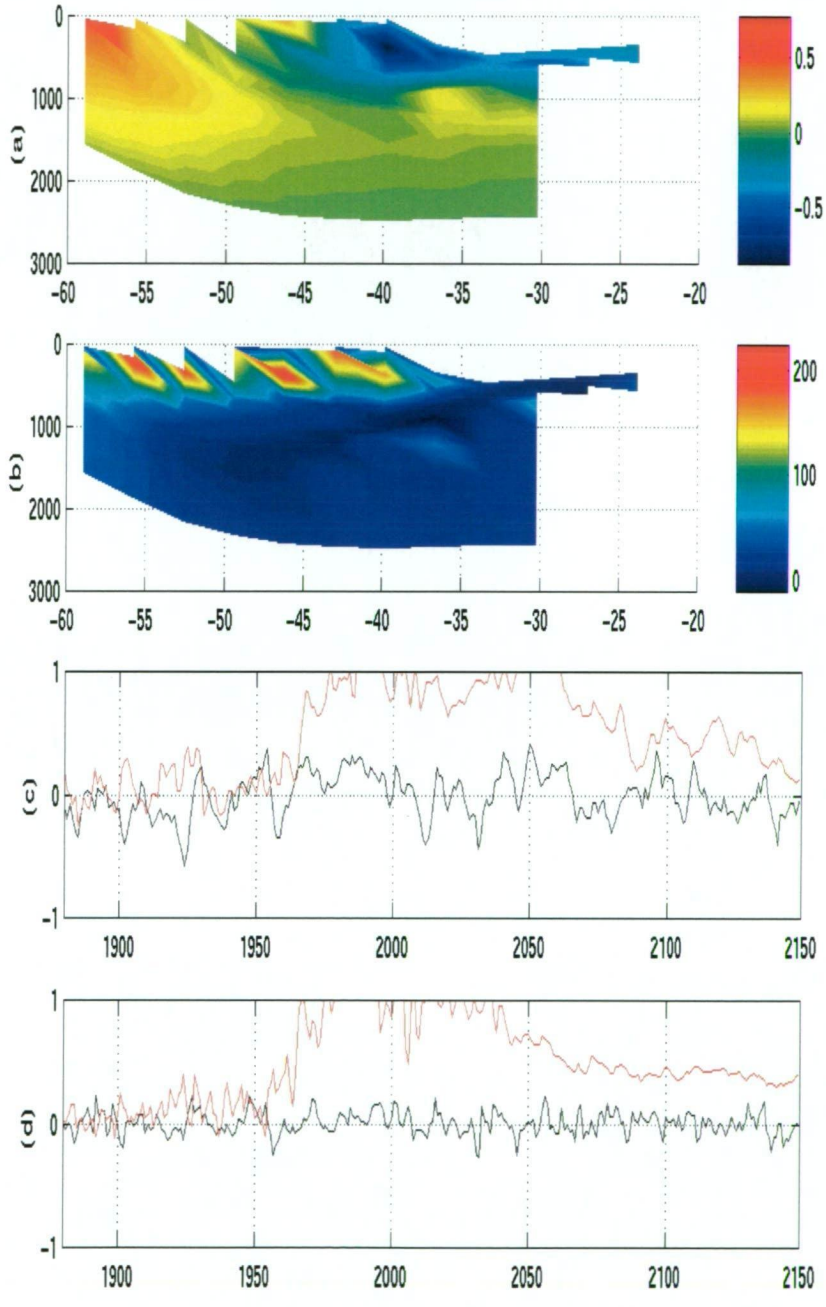

Figure 6.2: (a) $P_\theta(x, 2000)$, $P_\rho(x, 2000)$; (c) u(t) (black) and v(t) (red) for Potential Temperature (θ) and (d) u(t) (black) and v(t) (red) for pressure (ρ); for p = 5 and l = 30 along 110°E. Significance (p¡0.5) is greater than 0.5.

salinity minimum at 1000 m). The magnitude of these changes are around a 0.2°C cooling in the mode water and 0.2 to 0.4°C warming in the intermediate water. Note that cooling (warming) on neutral surfaces occurs in conjunction with a decrease (increase) in salinity. A map of change (for the same 30 year period) of pressure on neutral density surfaces is shown in Figure 6.1 (b). Between 1950 and 1980, the changes show a deepening of density surfaces in the regions where SAMW and AAIW occur. Most of the water column experiences at least a slight deepening, with the exception of a region at 45°S to depths of 500m as well as deeper than 1000 m. The magnitude of the pressure changes range from 10 m shallower to around 80 m deepening. Note that in both figures discussed, there are some wave like patterns seen at the surface and at the edges of the data set. These effects are produced by the interpolation routine used in the graphics display and may be ignored.

Figure 6.1(c) (black contour and red contours) show the the uncentered statistics calculated using the above potential temperature changes and 300 years of control and transient model data (respectively). The control statistic shows an oscillating behavior with periodically strong positive and negative correlation (statistic ≥ 0.5 equivalent to 95%CI). The transient statistic shows oscillating behavour also. The transient and control statistics differ in that the transient uncentered statistic is mostly positively correlated with the map of change, with the exception of post 2100, where the statistic is negative. These results indicate that temperature changes seen at 110°E in Figure 6.1(a) are reflective of changes that can be seen throughout the control run data set (in both positive and negative forms) and the transient run

data set (mostly in a positive form).

Figure 6.2 shows similar results but using comparative years 2000 to 2030 and expanded set of neutral surfaces 26 to 28 kgm^{-3}. The maps showing the change in potential temperature and pressure (Figures 6.2 (a) and (b)) have similarities and differences to those of 1950 to 1980 (Figure 6.1 (a) and (b)). The similarities include: Potential temperature decreases in the vicinity of SAMW and increases over AAIW. Pressure of neutral density surfaces tends to be higher in the top 500 m. The differences are that the magnitudes of change are much greater: potential temperature changes are plus/minus 0.5°C and pressure increases are up to 200 dbar. Calculating control and transient run uncentered statistics we see very different results (Figure 6.2 (c) black and red contours respectively). The control run statistic is not significantly correlated with this strong temperature change pattern. The transient run statistic show significant positive correlation after 1970 through to 2080. After 2080 there are periods of positive and significant correlation until 2125 where the correlation becomes insignificant. This indicate that the evolving picture of change (which included larger magnitudes of warming on ispycnals on the salinity minimum) correlates with a large portion of the transient timeseries and not with the control run timeseries.

The pressure statistics show a similar but also unique result (Figure 6.2 (d)). The control run statistic is not significant over the timeseries (black contour). The transient run (red contour) shows positive and significant correlation between 1970 and 2060. After 2060, correlation is positively correlated but

not significant.

6.3 Comparison with observations

Chapter 1 outlined various studies which compared historical observations with more recent observations. Here we will compare the observed changes with some simulated changes (from the transient model run) to first determine whether correlation occurs between modelled and observed changes. If correlation occurs, the second step is to calculate an uncentered statistic using control and transient model output. This allows us to determine whether the changes may be attributed to natural variability, anthropogenic climate forcing, both or neither. Since the study has thus far consisted of meridional transects, the observations with which I make comparison are those described by Aoki et al. (2005) along 150°E. In the model dataset I conduct a comparative study along 146°E (the closest model gridpoint to 150°E). Along 150°E, on 27 kgm^{-3}, the observed changes consisted of: freshening and cooling in SAMW north of the SAF; and increased salinity and temperature south of the Polar Front.

Using model data, $P_\theta(x, 1950)$, $P_\rho(x, 1950)$, where θ is potential temperature and ρ is pressure) and subsequent uncentered statistics u(t) and v(t) using 2p+1=11 and l=30 along 146°S are shown in Figure 6.3. Figure 6.3 (a) shows us that the map of potential temperature change between the average of 1945 to 1955 and the average of 1975 to 1995 is as follows: Between 45 and 50°S there is mainly cooling on isopycnals, associated with SAMW. Between

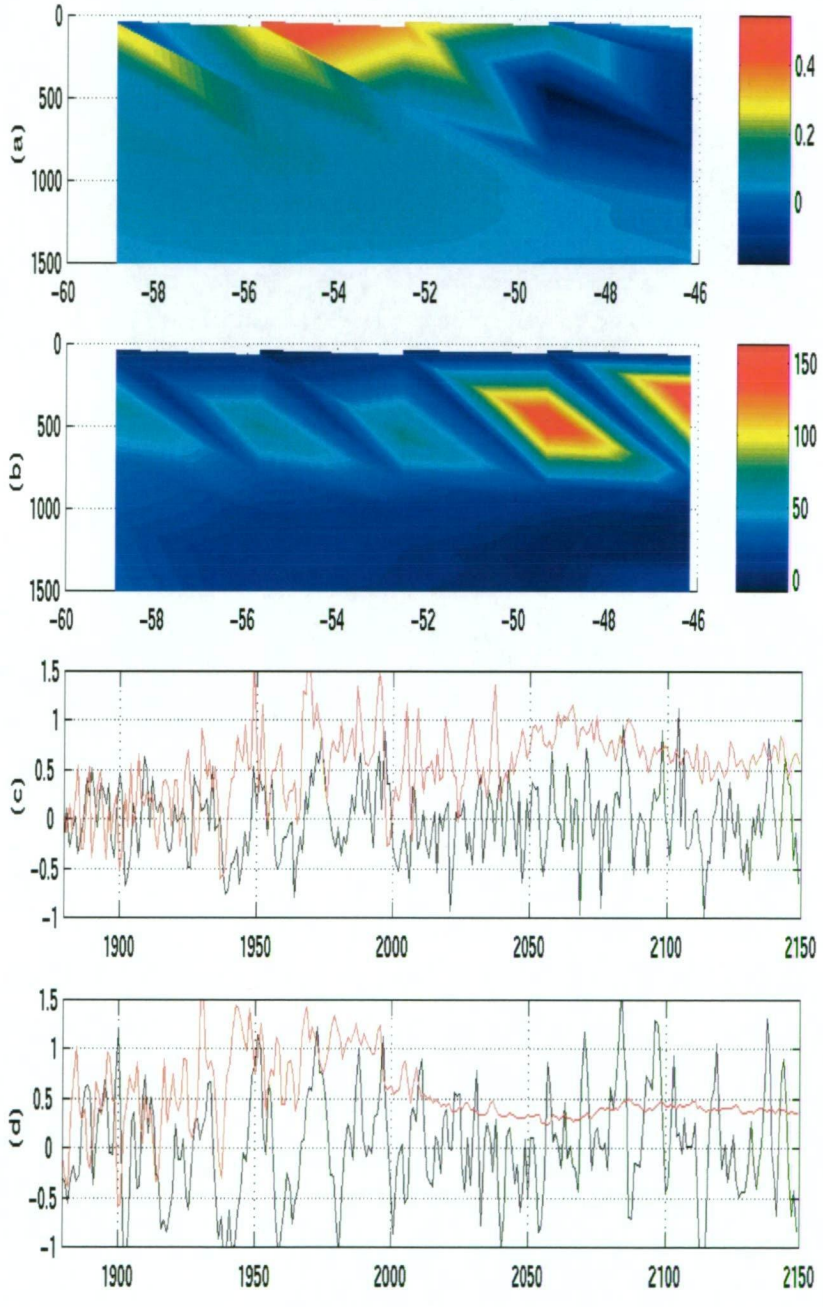

Figure 6.3: (a) $P_\theta(x, 1950)$, $P_\rho(x, 1950)$; (c) u(t) (black) and v(t) (red) for Potential Temperature (θ) and (d) u(t) (black) and v(t) (red) for pressure (ρ); for p = 5 and l = 30 along 146°E. Significance (p¡0.5) is greater than 0.5.

50 to 56°S there is strong warming (> 0.4°C) to about 500 m and slight warming throughout the remainder of the water column and further south. These include AAIW. Hence the SAMW shows cooling and freshening and the AAIW is saltier and warmer. This result qualitatively agrees with the observations. The figures show some interpolation errors (near the surface) which should be ignored. The pattern of pressure change (Figure 6.3 (b)) shows a subsurface deepening of neutral surfaces (peaks at about 500 m). The wave effect is interpolation plotting error and can be ignored. We don't have observations to compare this result with.

Since the change of potential temperature qualitatively agrees with observed changes, we can proceed with step 2. Examining the uncentered statistics (Figure 6.3 (c)) for the control and transient runs, we see that the pattern of temperature change is at times significantly correlated with both control and transient time series. In particular, the control run shows episodes of significant positive or negative correlation at least twice every 50 years. Hence the changes may be due to natural climate variations. The transient run, also shows oscillating correlation between 1880 and 1950 afterwhich it shows episodes of strong positive correlation only. After 2040, there is persistant and significant positive correlation until around 2125. Hence, the transient model is undergoing a persistant state of change over periods of 30 years and is well represented by the map of temperature change in Figure 6.3 (a). Therefore the temperature changes may also be attributable to anthropogenic climate changes.

This indicates that the individual snapshot of change provided by the observations (and the transient model years 1950 to 1980) may be due to natural variations or a climate change. That is, either cause cannot be ruled out. It also indicates that if future sampling shows changes of opposite sign, the changes may be attributable, in part to natural climate variations. On the other hand, as comprehensive observations become available, if the changes continue to be consistent with Aoki et al. (2005) then these results would indicate that the changes are statistically unlikely due to natural variability.

Aoki et al. (2005) does not describe the corresponding change in pressure on neutral density surfaces. Here we discuss these as seen in the model output. The map of change of pressure on the neutral density surfaces (Figure 6.3 (b)) over 30 years in the transient run shows a deepening of surfaces centered at around 500 m and peaking between 45 and 50°S. This indicates that in particular, neutral density surfaces inclusive of SAMW have, on average, deepened. Comparing this scenario of change with the control run output, this scenario is reflected significantly in both its positive and negative forms with periods ranging between 5 to 25 years. Comparing the scenario of pressure change with the transient run, a different result emerges. The uncentered statistic oscillates with periods of significance until about 1950, where it remains significant and positively correlated until about 2010. After 2010, the statistic is positively correlated but without significance.

This indicates that transient changes in potential temperature and pressure are not simply correlated. A key difference is that changes in potential tem-

perature are correlated significantly until 2150 (end of dataset), whereas the pressure changes lose significance (although not positive correlation) at around 2010. This indicate that the projected changes in potential temperature persist with large magnitude for much longer than projected changes in pressure on neutral surfaces.

6.4 Discussion and Conclusion

This chapter has used uncentered statistics to draw the following conclusions. By making a case study of the 110°E meridion we saw that examining changes over a three decade period from 1950 and comparing with control and transient runs shows that changes could generally be attributable to either natural variations or the simulated man-made change. Using changes from the tri-decade from 2000, the results changed. The control run no longer showed any significant correlations with the examined changes and the probability that the changes are due to natural variations are statistically very low/unlikely. That is, the simulated changes from the 1950 tri-decade were weaker than those extracted from the 2000 tri-decade and the transient model run was the only model run to exhibit repeated tri-decadal change with magnitude and structure consistent with the latter tri-decade. How can these results be applied to climate change observing techniques. The results suggest that repeated observing over similar timescales is required to monitor how changes are evolving.

In Section 6.2 we used the uncentered statistic technique to qualitatively

assess observed changes. The results revealed that neither natural variability or man-made climate changes could be ruled out as potential causes.

This result is significant. It indicates that further observational sampling is required in order to statistically disprove either of the causes. In particular, the results recommend repeat sampling on time scales inclusive of dominant natural modes. Armed with such data we can determine whether changes are occurring which are unlikely to be natural by two means. If the magnitude of catalogued changes is significant compared to variability levels, this makes natural variability to appear less likely. Second, if changes, regardless of magnitude, consistently are unable to reflect both positive and negative reflection of a natural cycle (ie. the spatial polarization is fixed), then the demonstration of natural causes is diminished.

Chapter 7

Conclusions

This thesis has three aims. First, to characterise the general patterns of variability in the Southern Ocean component of a coupled model. Second, to determine sources or factors which generate and influence these variability patterns. Lastly, to determine the impact of a climate change signal in terms of water mass properties.

For the first aim, I used Hovmoeller diagrams of potential temperature anomalies along a streamline in the Southern Ocean to investigate propagation. Circumnavigating temperature anomalies clearly occur in the modelled southern ocean in shallow to intermediate depths (1000 m). At 410 m, along a streamline where the speed of the Antarctic Circumpolar Current is a maximum, the speed of the strongest anomalies is approximately 4 cm/s. The strongest anomaly time-scales are 4-5 years (interannual anomalies) and take approximately 20 years to travel around the globe. The anomaly strength is not uniform along this streamline. The strongest anomalies occur in the

longitude band 100 to 200°E. Here the streamline moves relatively far south towards Antarctica. Although ACW-like variability with timescales of 4 to 5 years is the dominant signal, decadal variation with timescales of approximately up to 40 years also occur. Below 1000 m, there is a minor presence of interannual variability and the decadal variability is the dominant signal and persists to at least 2000 m. The phase speed of these propagating signals decreases with depth. Scatterplots show a clear relationship between ACC current speed and phase speed throughout the water column. For each depth, the wave speed is calculated directly from the Hovmoeller plots for the more dominant propagating anomalies (ACW or decadal variability). This relationship is strongest at intermediate depths (500 to 1500 m) where anomalies are most strongly advected and least subject to other influences such as convection, mixing and mid-ocean ridges.

Using HEOF analysis I directly determine statistical modes of variability and their corresponding temperol and spatial variability. This revealed two dominant modes of variability in the Southern Ocean. First, a mode characterised by interannual anomaly in temperature and salinity on shallow to intermediate depth and density surfaces. The spatial structure of this mode is dominated by zonal wavenumber 3. Also, there is significant correlation between temperature and pressure anomalies on density surfaces. The pressure pattern is 180° out of phase with the temperature changes on density surfaces. This is similar to a mechanism proposed by (White et al., 1998) for the ACW.

The second mode is a decadal variation which dominates on all intermediate to deep depths and density surfaces. The decadal signal is primarily seen with spatial structure zonal wavenumber 2. Overall, the decadal signal is the dominant feature of the Southern Ocean, with more total energy in this mode throughout most of the water column. The interannual variability has been described in studies using observations or models of the Southern Ocean. The spatial zonal wavenumber 3 feature of the interannual variability occurs has been described in studies using models. Interannual variability is also seen in studies of observations, however in observations the spatial distribution tends to be zonal wavenumber 2. For example, observations analysed by White and Peterson (1996) showed interannual anomalies with zonal wavenumber 2. Previous model studies which have obtained a zonal wavenumber 3 pattern, suggest that the difference is due to the slower ACC currents seen in the coupled model, compared with the observations. The coupled model used in this experiment also has slower current speeds than observed.

For the second aim, I first examined variability in several atmospheric properties including wind stress, heat and salinity fluxes. The heat flux and meridional wind component showed dominant modes of interannual variability with zonal wavenumber 3. These two properties have been shown to play a significant role in determining SSTs in the Southern Ocean. The results indicates that heat flux and meridional wind are important for creating zonal wavenumber 3 interannual variability in resultant SSTs. The second mode, consists of a decadal signal with dominant zonal wavenumber 2. The zonal

wavenumber 2 component is more intriguing. Slower timescales in the ocean occur due to natural filtering of anomalies such that interannual signals are absorbed and only the longer term decadal signals remain. The change in dominance from a signal with spatial structure zonal wavenumber 3 to zonal wavenumber 2 is more complex. Exploring the possible reasons for a zonal wavenumber 2 structure required investigation of convection regions in the Southern Ocean. An estimate of mixed layer depth revealed two dominant regions of wintertime convection. The first begins in the southeast Indian Sector of the Southern Ocean and continues to below Australia. The second region is the Pacific Ocean to the east of Drake Passage. These two regions are important for generation of SAMW and AAIW respectively. In essence, these two regions of convection act like highways in a myriad of surburban streets whereby anomalies at the surface can quickly access the deeper depths (compared with anomalies at the surface in adjacent regions of low convection). A simple model is used to test the assumption (Chapter 4). Forcing this model with interannual, zonal wavenumber 3 heat flux anomalies and applying a convection system of two convective regions, we obtain a resultant subsurface anomaly with zonal wavenumber 2. This experiment showed the hypothesis: that the distribution of convection regions influences the zonal wavenumber structure of anomaly to be reasonable.

For the third aim, I compared warming and deepening signals seen in the transient model run with a control run. There is a consistent pattern of cooling on isopycnals in shallow/Mode waters and warming on isopycnals in AAIW in the transient run. This coincides with a general deepening of

density surfaces. The fingerprint experiment reveals statistical significance in these results indicating that the simulation of CO_2 changes, indeed produces changes, to Southern Hemisphere water masses with the described spatial pattern. Qualitative comparison with studies of observed changes show a similar pattern of change.

Bibliography

R. Allan and C. Reason. Modelling Indian Ocean Responses to Low Frequency Fluctuations in Observed Wind Patters. *Mathematical Computing and Modelling*, 21(9):143–149, 1995.

Shigeru Aoki, Nathaniel Bindoff, and John Church. Interdecadal Water-mass Changes in the Southern Ocean between 30° E and 160°E. *Geophysical Research Letters*, 32:7607.1–7607.5, 2005.

Peter G. Baines and Wenju Cai. Analysis of an Interactive Instability Mechanism for the Antarctic Circumpolar Wave. *Journal of Climate*, 13(11): 1831–1844, June 2000.

H. Banks and N. Bindoff. Comparison of Observed Temperature and Salinity Changes in the Indo-Pacific with Results fromt he Coupled Climate Model HadCM3: Processes and Mechanisms. *Journal of Climate*, 16:156–166, January 2003.

H. Banks and R. Wood. Where to Look for Anthropogenic Climate Change in the Ocean. *Journal of Climate*, 15:879–891, April 2002.

T. Barnett. Comparison of near-surface air temperature variability in 11

coupled global climate models. *Journal of Climate*, 12:511–518, February 1999.

J. Barsugli and D. Battisti. The Basic Effects of Atmosphere-Ocean Thermal Coupling on Midlatitude Variability. *Journal of the Atmospheric Sciences*, 55(4):477–493, February 1998.

Daohua Bi. *Transient and long-term behaviour of the world ocean under global warming.* PhD thesis, University of Tasmania, 2002.

G Bigg. The role of oceans in climate. 23:1127–1159, 2003.

N. Bindoff and J. Church. Warming of the water column in the southwest Pacific Ocean. *Nature*, 357:59–62, May 1992.

N. Bindoff and T. McDougall. Diagnosing Climate Change and Ocean Ventilation Using Hydrographic Data. *Journal of Physical Oceanography*, 24 (6):1138–1152, June 1994.

N. Bindoff and T. McDougall. Decadal changes along an Indian Ocean section at 32°s and their interpretation. *Journal of Physical Oceanography*, 30(6): 1207–1222, 0 2000.

Hans Bonekamp, Andreas Sterl, and Gerbrand J. Komen. Interannual variability in the Southern Ocean from an ocean model forced by European Centre for Medium-Range Weather Forecasts reanalysis fluxes. *Journal of Geophysical Research*, 104:13317–13331, June 1999.

W Broecker. Thermohaline Circulation, the Achilles Heel of Our Climate

System: Will Man-Made CO2 Upset the Current Balance? *Science*, 278: 1582–1588, November 1997.

H. Bryden, E. McDonagh, and B. King. Changes in Ocean Water Mass Properties: Oscillations or Trends? *Science*, 300:2086–2088, June 2003.

Wenju Cai, Peter G. Baines, and Hal B. Gordon. Southern Mid- to High-Latitude Variability, a Zonal Wavenumber-3 Pattern, and the Antarctic Circumpolar Wave in the CSIRO Coupled Model. *Journal of Climate*, 12 (10):3087–3104, October 1999.

Wenju Cai and Hal B. Gordon. Southern high-latitude ocean climate drift in a coupled model. *Journal of Climate*, 12:132–146, December 1999.

M. Christoph, T.P. Barnett, and E. Roekner. The Antarctic Circumpolar Wave in a Coupled Ocean-Atmosphere GCM. *Journal of Climate*, 11(7): 1659–1672, July 1998.

M. England, J. Godfrey, A. Hirst, and M. Tomczak. The mechanism for Antarctic Intermediate Water renewal in a world ocean model. *Journal of Physical Oceanography*, 23:1553–1560, 1993.

H Friedli, H. Lotscher, H. Oeschger, U. Siegenthaler, and B. Stauffer. Ice core record of 13c/12c ratio of atmospheric co_2 in the past two centuries. *Nature*, 324:237–238, 1986.

P Gent and J. McWilliams. Isopycnal mixing in ocean circulation models. *Journal of Physical Oceanography*, 20:150–155, 1990.

Per Gloersen. Modulation of hemispheric sea ice covers by ENSO events. *Nature*, 373:503–508, 1995.

K. Hanawa and L. Talley. Mode waters. In G. Siedler, J. Church, and J. Gould, editors, *Ocean Circulation and Climate: Observing and Modelling the Global ocean*, pages 373–386. Academic Press, Harcourt Place, 32 Jamestown Road, London NW1 7BY, UK, 2001.

J Hansen, M. Sato, A. Lacis, R. Ruedy, I. Gegen, and E. Matthewsr. Climate forcings in the industrial era. *Proceedings of the National Academy of Sciences*, 95:12753–12758, 1998.

S. Hellerman and M. Rosenstein. Normal monthly wind stress over the World Ocean with error estimates. *Journal of Physical Oceanography*, 13:1093–1104, 1983.

P. Jones and T. Osborn. Estimating sampling errors in large-scale temperature averages. *Journal of Climate*, 10(10):2548–2568, 1997.

P. Jones, T. Wigley, and P. Wright. Global temperature variations between 1861 and 1984. *Nature*, 322:430–434, July 1986.

C Keeling and T. Whorf. Atmospheric carbon dioxide records from sites in the sio air sampling network. In *Trends: A Compendium of Data on Global Change*. Carbon Dioxide Information Center, Oak Ridge National Laboratory, 1998.

S Levitus. *Climatological Atlas of the World Ocean*. NOAA, 1982.

M. McCartney. Subantactic mode water. In M. Angel, editor, *A voyage of Discovery, George Deacon 70th Anniversary Volumn*, pages 103–119. Pergamon PRess, Oxford, 1977.

M. McCartney. The subtropical circulation of mode waters. *Journal of Marine Research*, 40:427–464, 1982.

D. McDermott. The regulation of northern overturning by southern hemisphere winds. *Journal of Physical Oceanography*, 26:1234–1255, 1996.

G. Meehl, G. Boer, C. Covey, M. Latif, and R. Stouffer. Intercomparison makes for a better climate model. *Eos, Transactions, American Geophysical Union*, 78:445–451, 1997.

T. Motoi, A. Kitoh, and H. Koide. Antarctic Circumpolar Wave in a coupled ocean-atmosphere model. *Annals of Glaciology*, 27:483–487, January 1998.

E. Murphy, A. Clarke, C. Symon, and J. Priddle. Temporal variation in Antarctic sea-ice: Analysis of a long term fast-ice record from the South Orkney Islands. *Deep-Sea Research*, 42(1):1045–1062, 1995.

N Nicholls, G. Gruza, J. Jouzel, T. Karl, L. Ogallo, and D. Parker. Observed climate variability and change. In J. Houghton, L. Filho, B. Callander, N. Harris, A. Kattenberg, and K. Maskell, editors, *Climate Change 1995. The Scientific Basis. The Contribution of Working Group 1 to the Third Assessment Report of the Intergovernmental Panel on Climate Change.*, pages 133–192. Cambridge University Press, Cambridge, UK, 1996.

S. Rintoul. South Atlantic interbasin exchange. *Journal of Geophysical Research*, 96:2675–2692, 1991.

S. Rintoul and M. England. Ekman transport dominates local air-sea fluxes in driving variability of Subantarctic Mode Water. *Journal of Physical Oceanography*, 32:1308–1321, 2002.

S. Rintoul, C. Hughes, and D. Olbers. The Antarctic Circumpolar Current System. In G. Siedler, J. Church, and J. Gould, editors, *Ocean Circulation and Climate: Observing and Modelling the Global ocean*, pages 271–302. Academic Press, Harcourt Place, 32 Jamestown Road, London NW1 7BY, UK, 2001.

B. Santer, U. Mikolajewicz, W. Bruggermann, U.. Cubasch, K. Hasselmann, H. Hock, E. Maier-Reimer, and T. Wigley. Ocean variability and its influence on the detectability of greenhouse warming signals. *Journal of Geophysical Research*, 100:10693–10725, 1995.

B. Santer, K. Taylor, T. Wigley, T. Johns, P. Jones, K. Karoly, J. Mitchell, A. Oort, J. Penner, V. Ramaswamy, M. Schwarzkopt, R. Stouffer, and S. Tett. A search for human influences on the thermal structure of the atmosphere. *Nature*, 382:39–46, July 1996.

B Sloyan and S. Rintoul. Circulation, renewal , and modification of antarctic mode and intermediate water. *Journal of Physical Oceanography*, 31(4): 1005–1030, April 2002.

L. Talley. Some aspects of ocean heat transport by the shallow, intermediate and deep overturning circulations. *Geophysical Monograph*, 112:1–22, 1999.

J. Toggweiler and B. Samuels. *Is the magnitude of the deep outflow actually governed by Southern Hemisphere Winds?* Springer-Verlag, 1993.

J. Toggweiler and B. Samuels. Effect of the sea ice on the salinity of antarctic bottom waters. *Journal of Physical Oceanography*, 25(9):1980–1997, 1995.

M. Tomczak and J. Godfrey. *REgional Oceanography: An introduction.* Pergamon Press, 1994.

Warren B. White. Influence of the Antarctic Circumpolar Wave on Australian Precipitation from 1958 to 1997. *Journal of Climate*, 13(7):2125–2141, July 2000.

Warren B. White, Shyh-Chin Chen, and Ray. G. Peterson. The Antarctic Circumpolar Wave: A Beta Effect in Ocean-Atmosphere Coupling over the Southern Ocean. *Journal of Physical Oceanography*, 28(12):2345–2361, December 1998.

Warren B. White and Neil J. Cherry. Influence of the Antarctic Circumpolar Wave upon New Zealand Temperature and Precipitation during Autumn-Winter. *Journal of Climate*, 12(4):960–976, April 1999.

Warren B. White and Ray G. Peterson. An Antarctic circumpolar wave in surface pressure, wind, temperature and sea-ice extent. *Nature*, 380: 699–702, April 1996.